Dissertations, Theses, and Masters Projects   Theses, Dissertations, & Master Projects

2004

Characterization of transient behaviors in a colliding pulse mode-locked (CPM) laser

Wei Yang
College of William & Mary - Arts & Sciences

CHARACTERIZATION OF TRANSIENT BEHAVIORS IN A COLLIDING PULSE MODE-LOCKED (CPM) LASER

A Dissertation

Presented to

The Faculty of the Department of Physics

The College of William & Mary in Virginia

In Partial Fulfillment

Of the Requirements for the Degree of

Doctor of Philosophy

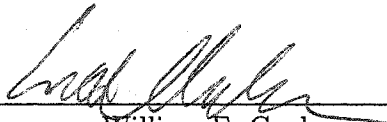by

Wei Yang

2004

APPROVAL SHEET

This dissertation is submitted in partial fulfillment of

the requirements for the degree of

Doctor of Philosophy

_____

Wei Yang

Approved, July 2004
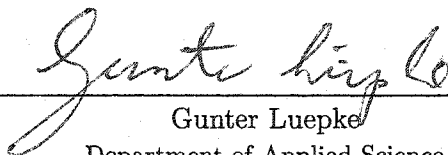
_____

William E. Cooke

Thesis Advisor

_____

Eugene R. Tracy

_____

John B. Delos

_____

Anne Reilly

_____

Gunter Luepke

Department of Applied Science

ii

To my parents...

Table of Contents

v

ACKNOWLEDGMENTS

My first acknowledgement goes to Dr. William E. Cooke. I am very lucky to have him as my advisor. I deeply appreciate the valuable training and teaching he provides me with. Without his insightful and patient guidance, this work would not have been possible.

I would also like to acknowledge Dr. Eugene R. Tracy and Dr. John B. Delos. I truthfully thank Dr. Tracy for his guidance to the project as well as his encouragement to me. Dr. Delos has always been readily to discuss and answer any questions I bring to him.

I also want to thank the members of our weekly working group for their input and collaboration in research: Dennis Weaver, George Andrews, Chris Kulp, Andrew Davis, Haijian Chen, Stephen Richardson, and Peter Harris, and Rui Yang for his help. My acknowledgement also goes to Dr. Jan Chaloupka, Dr. Dennis Manos, and Dr. Thomas F. Gallagher (University of Virginia) for kindly letting me use their lab instruments in this project.

I would like to thank the many friends I made during my graduate study for the help and happy experience they have given me.

My gratitude and love to my family is forever.

List of Tables

List of Figures

x

xiii

ABSTRACT

A colliding pulse mode-locked (CPM) laser achieves sub-picosecond operation by synchronizing two counter-propagating pulse trains to form a standing wave in a thin absorber jet. When properly aligned, these lasers maintain mode-locking for more than 100 seconds (10^{10} pulses), but eventually cease mode-locking for short periods of time. This thesis examines the characteristics of these transient events, when CPM mode-locking ceases (dropout) and when it resumes (dropin). The dropout is an apparently rapid event, typically lasting no longer than 5 microseconds or less than 500 pulses. The dropin takes significantly longer time, often has structure, and has a clear power dependency. This thesis uses a variety of statistical methods to search for changes in the nonlinear dynamics prior to the apparent power output change of a dropout, but does not find consistent precursors. Moreover, this thesis uses a fluence mapping method to study ultrashort pulse generation process in a novel bistable medium model. The bistable medium model naturally incorporates various high order perturbations and provides a framework for dynamics study and pulse shape control in ultrafast lasers.

CHARACTERIZATION OF TRANSIENT BEHAVIORS IN A

COLLIDING PULSE MODE-LOCKED (CPM) LASER

Chapter 1

Introduction

The CPM laser is a typical example of ultrafast systems that use passive mode-locking technique. The passive mode-locking action is caused by the interaction of the saturable gain and the slow saturable absorber in the CPM laser. During its passive mode-locking process, the CPM laser self-starts from oscillation noise caused by unlocked modes and stabilizes with ultrashort pulses forming in the cavity.

Since the passive mode-locking process relies on saturation absorption, the CPM laser is subject to transient power fluctuations such as dropout and dropin. This thesis studied the transient behaviors, especially dropout and dropin behavior, in the CPM ring laser, with an ultimate goal of early detection and control of these behaviors.

Previously, long-term stability control of the CPM laser has been studied to reduce noise and timing jitter effect, yet the transient behaviors, such as dropout and dropin, in this laser has never been studied [1]. We recorded the dropout and dropin events and calibrated their forms. As a first step of the attempt to control the dropout processes in this laser, we studied the dropout events to search for any possible precursor to them. We analyzed time series of pulse power collected before dropouts using various statistical methods, but no consistent precursor is observed yet.

2

The CPM laser provides a unique tool to test the nonlinear models developed to describe the pulse generation process in ultrafast lasers. In a CPM laser, the gain and the absorber are physically separate, allowing either to be varied independently.

The theoretical study of the CPM laser's dynamics by Andrews and Tracy reveals defects in previous ultrafast laser theories such as the neglect of gain memory effect. Their study of CPM lasers predicted the difference between dropout and dropin processes, which was confirmed by our experiment.

We proposed a fluence mapping method to study ultrafast lasers in order to develop a simple and clear model that allows for the study of the dynamics of ultrafast lasers. Using this method, we developed a novel bistable medium model to describe the ultrashort pulse generation process. This model provides a direct and intuitive relation between pulse generation and the physical parameters of the laser. It is also able to include higher order dispersion terms in modeling on a sound basis. The commonly encountered problem of dealing with various pulse shapes is readily solved in this method. In this model, closed form solutions exist for soliton shape pulses.

1.1 Why Ultrashort Pulses

Very short optical pulse generation has been an interesting subject to researchers for the fine temporal resolution they can provide [2]. The studies of fast dynamics of nature such as electronic relaxation in atoms and vibrations in molecules constantly demand shorter optical pulses to achieve higher temporal resolution.

While seeking shorter pulse and higher resolution, people used many techniques such

as mechanical shutters and fast electronic devices (picosecond). Ultrafast lasers pushed the limit to an unprecedented level of femtosecond time scales. Recent development of ultrashort pulse generation technology has allowed us to examine fundamental processes in material within a few femtoseconds.

The advance in ultrashort pulse generation techniques also paved the way for new fields in science and technology. The unique optical properties of ultrashort pulses, such as ultrashort duration, ultra-wide spectrum, and ultra-intense fields, make it an essential tool in fundamental studies in physics, chemistry, and biology, as well as in the laser fusion program, Terahertz devices, micro-machining, optoelectronics and communication systems.

1.2 A Brief Review of Ultrafast Lasers

The rapid advancement of ultrashort pulse generation technique started at the birth of laser in 1960. Soon after that, people invented many techniques such as flashlamp pumping, Q-switching (10 nanosecond) and mode-locking to generate optical pulses. The most important ultrashort pulse generation technique, mode-locking, was first demonstrated by Hargove *et al.* by actively modulating the loss of a helium-neon laser in 1964 [3]. Since then, various kinds of mode-locked lasers that generated from picosecond to femtosecond pulses have been discovered.

The development of the CW mode-locked dye laser (1972) was another important break-through [4]. In CW mode-locked dye lasers, pulse shaping effect in each round trip is small, therefore it takes many round-trips to evolve to a steady-state. The CPM laser developed on the basis of these early systems produces high quality pulses and reasonable stability.

The study of the CW mode-locking of dye lasers also provided essential knowledge of ultrafast lasers, such as dispersion and self-phase modulation (SPM). Along with the evolution of ultrafast lasers, pulse amplifying, shaping, and spectrum broadening techniques also advanced. These techniques make it possible to compress pulses to even shorter durations outside the laser cavity. The cumulative development led to a steady decreasing of pulse duration to a few femtoseconds (6fs, 1987). But, despite their good performance, dye lasers are usually inconvenient to use and hard to maintain due to laser dye's aging, toxicity, and circulating requirement.

The realization of Kerr Lens mode-locked (KLM) Ti:sapphire laser greatly improved this situation (1990) [5]. In late 1990's, KLM has been realized in many solid-state laser systems that are more convenient and compact than the dye laser systems. Although solid-state ultrafast laser systems cannot produce pulses much shorter than dye laser systems, their beam quality, stability, and power level have made it possible for them to replace the role of dye lasers in ultrafast techniques. Today has seen the state-of-the-art ultrafast dye and solid-state laser systems producing pulses with just 2-3 cycles of oscillation in the visible range, which is close to the ultimate limit of a pulse with only one cycle of oscillation. Though various solid-state, dye, color-center, fiber, and semiconductor lasers have been available to generate femtosecond pulses since mid 1990's, the CPM dye laser has been one of the most successful ultrashort pulse generating systems.

Using femtosecond pulses, a number of rapid physical and chemical processes can be studied, such as the dynamics in condensed matter [6]. But the limit of temporal resolution still exists in the studies of very fast processes like inner-shell electron relaxation, which may happen below femtosecond time scale. This limit opens a new field, attosecond tech-

nology, with great challenges. The next generation of ultrafast pulses must have shorter wavelengths. New techniques to produce sub-femtosecond pulses, such as high harmonic generation, are still being studied. Other directions of today's ultrashort pulse generation science and technology include ultrahigh-peak-power pulse generation, ultrafast laser tunability, laser dynamics study, and parametric control of pulse.

1.3 A Brief Review of Ultrafast Laser Theory

The development of ultrafast laser theory was closely related to the advance of ultrafast lasers. The early theories of ultrafast lasers based on the rate equations of the laser medium, which effectively explained the laser's mode-locking and pulse shaping processes.

As researchers achieving shorter and shorter pulses, the group velocity dispersion (GVD) and self-phase modulation (SPM) in the ultrafast systems became the limit of ultrashort pulse generation. Various theories proposed at this stage deepened people's understanding of ultrafast systems. But once people realized the importance of GVD and SPM, more universal theories such as the Landau-Ginzburg equation and nonlinear Schrodinger equation were used to model ultrafast systems with success.

In extreme short pulse generation, the theoretical concerns center around the higher order dispersion and compensation of the Kerr effect. The instability in ultrafast lasers such as power and duration fluctuation and timing jitter also bring up interesting problems for control.

Chapter 2

Basic Knowledge of Pulse Optics

Ultrashort pulses are readily described by time and space dependent classical electric field. This chapter discusses the description, propagation, and measurement of ultrashort pulses using the field representation in Section 2.1 and 2.2.

Moreover, to lay a background for the theoretical and experimental work we shall discuss in later chapters, this chapter also carries out a short introduction to the two key techniques using in ultrafast lasers: mode-locking and dispersion control, in Section 2.3.

2.1 Optical Properties

In the description of an ultrashort pulse, a number of parameters are used. For a single pulse, its envelope, duration, spectrum width, carrier frequency, spatial shape, and chirp are its essential properties. A full description will also need to include envelope-carrier phase and polarization of the pulse. Section 2.1.1 will discuss the definitions of some of these parameters and their relationships using a Gaussian pulse. The propagation of the pulse in optical medium demonstrates the interaction between them, which is essential basis for various ultrafast techniques. Section 2.1.2 describes the linear processes that occur while

7

a Gaussian pulse traverses an optical medium. Section 2.1.3 briefly reviews the optical properties of ultrashort laser beam.

2.1.1 Representation of Ultrashort Pulses

The electric field of an optical pulse can be described either temporally or spectrally. The two representations are equivalent and related through the Fourier transform.

Leaving out the transverse distribution and the polarization of the field, a Gaussian shape pulse can be written as the product of a monochromatic plane wave and a Gaussian envelope [7],

$$\mathbf{E}(\mathbf{r}, t) = E_0\, e^{-\Gamma t^2} e^{i(\omega_0 t - \mathbf{k}\cdot\mathbf{r})}, \qquad |\mathbf{k}| = \frac{2\pi}{\lambda} = \frac{\omega}{c}, \tag{2.1}$$

where $\mathbf{E}$ is the electric field perpendicular to the propagating direction, $\mathbf{r}$, of the pulse, E_0, Γ, ω_0, and $\mathbf{k}$ are the amplitude, the shape factor of the Gaussian envelope, carrier frequency at wavelength of λ, and wave vector, respectively. Eq. 2.1 can be reduced to a one-dimensional equation by assuming that the pulse's propagation is along the x axis,

$$\tilde{E}(x, t) = E_0\, e^{-\Gamma t^2} e^{i(\omega t - kx)}, \qquad \left(k = \frac{2\pi}{\lambda} = \frac{\omega}{c}\right). \tag{2.2}$$

At $x = 0$, the spectral content of the pulse can be derived from the Fourier transform as,

$$E(\omega) = \left(\frac{\pi}{\Gamma}\right)^{1/2} E_0\, exp\left[-\frac{(\omega - \omega_0)^2}{4\Gamma}\right]. \tag{2.3}$$

For a pulse with its shape well defined, its duration, i.e. the full width at half maximum (FWHM) of its intensity, is easy to determine and measure. For the Gaussian pulse above, its duration is $t_p = 1.177\Gamma^{-1/2}$.

The FWHM of pulse's power spectrum, ν_p, is another useful parameter, which is in inverse proportion to the pulse duration through universal time-energy uncertainty, $t_p\omega_p \geq 1/2$. Depending on the dispersion of a pulse, when the spectral bandwidth is given, its duration is limited to be above a certain value,

$$t_p\nu_p = K \geq \frac{1}{4\pi}, \tag{2.4}$$

with the values of K for different pulse profiles shown in table 2.1. Eq. 2.4 also shows that the shorter a pulse is, the broader its spectrum is and the broader an ultrafast system's bandwidth needs to be. When the equality in Eq. 2.4 is reached, the pulse is called a Fourier-transform-limited (FTL) pulse [7].

Field	Intensity	t_p(FWHM)	Spectrum	ν_p(FWHM)	K
Gauss	$e^{-2\Gamma t^2}$	$1.177\Gamma^{-1/2}$	$e^{-(\omega-\omega_0)^2/2\Gamma}$	$0.375\Gamma^{1/2}$	0.441
sech	$sech^2(t/t_s)$	$1.763t_s$	$sech^2(\pi(\omega-\omega_0)t_s/2)$	$0.178/t_s$	0.315
Lorentz	$[1+(t/t_L)^2]^2$	$1.287t_L$	$e^{-2|\omega-\omega_0|t_L}$	$0.110/t_L$	0.142

Table 2.1: Profiles of conventionally used pulses and their spectrum, and the inequality relations between pulse duration and spectral width.

Deducing from Table 2.1, a 100 fs Gaussian pulse requires its frequency bandwidth to be 4.41×10^{12} Hz at minimum. If the spectrum is centered at $\nu_0 = 4.84 \times 10^{14}$ Hz (i.e. $\lambda_0 = 620nm$), this frequency bandwidth gives a wavelength range covering 6.2 nm [7]:

$$|\delta\lambda/\lambda_0| = \delta\nu/\nu_0. \tag{2.5}$$

Similarly, for a CPM laser with a bandwidth of 20 nm centered at 620 nm, the frequency bandwidth is 1.6×10^{13} Hz. In this system, the shortest Gaussian pulse that can be produced has duration of 27 fs.

In most practical cases, the envelope of a pulse is complicated. A pulse with arbitrary

envelope can be generally described as:

$$\tilde{E}(x,t) = \tilde{\psi}(t)e^{i\omega_0 t} = \rho(t)e^{i\phi(t)}e^{i\omega_0 t}, \tag{2.6}$$

where $\tilde{\psi}(t)$ is called the complex field envelope, and $\phi(t)$ is the function of time dependent

phase delay. The expansion of phase function in power of t gives:

$$\phi(t) = \phi_0 + \frac{d\phi}{dt}t + \frac{1}{2!}\frac{d^2\phi}{dt^2}t^2 + \frac{1}{3!}\frac{d^3\phi}{dt^3}t^3 + \dots . \tag{2.7}$$

The first order derivative of $\phi(t)$ has the unit of frequency, which can be absorbed into the

frequency term in Eq. 2.6, i.e.

$$\omega_l = \omega_0 + \frac{d}{dt}\phi(t). \tag{2.8}$$

The new frequency term, ω_l, is called carrier frequency of the pulse. The carrier frequency is

often used in the description of complicated pulse envelope instead of central frequency, ω_0,

which could be confusing in the cases of asymmetric or multi-hump shaped pulses. There

are other ways to decompose the phase function to get the carrier frequency [8], but we will

use the above definition throughout this thesis. Usually, $d^2\phi/dt^2 \neq 0$, in which case the

carrier frequency changes along the pulse and the pulse is said to be frequency modulated

or chirped. For a special case when $d^2\phi/dt^2 = 0$, the pulse is said to be chirp-free. When

$d^2\phi/dt^2 > 0$, the pulse is called up-chirped pulse. In an up-chirped pulse, the field oscillation

is faster in the trailing edge than that in the leading edge of the pulse. Frequency chirping

causes a pulse to be broader than its FTL pulse [9]. For example, when a linear chirp is

added to the Gaussian pulse, the field becomes

$$E(t) = E_0 e^{-(1+ia)\Gamma t^2} e^{i\omega_l t}. \tag{2.9}$$

The intensity profile of Eq. 2.9 is the same as that in Table 2.1, i.e. t_p does not change. But the spectral profile changes to

$$E(\omega) \propto exp\left(-\frac{(\omega - \omega_l)^2}{2\Gamma(1 + a^2)}\right), \tag{2.10}$$

with $\nu_p' = \sqrt{1 + a^2}\nu_p$. It shows that the pulse with same duration now requires a broader spectral width. In practice, pulses generated directly from ultrafast systems are usually chirped.

2.1.2   Propagation of Ultrashort Pulses

The propagation of pulses in a medium can be described by the wave equation derived from the Maxwell equations:

$$\left(\nabla^2 - \frac{1}{c^2}\frac{\partial^2}{\partial t^2}\right) \mathbf{E}(\mathbf{r}, t) = \mu_0 \frac{\partial^2}{\partial t^2}\mathbf{P}(\mathbf{r}, t), \tag{2.11}$$

where μ_0 is the magnetic permeability of free space, and $\mathbf{P}$ is the polarization of the medium induced by the field. $\mathbf{P}$ is the macroscopic description of the medium which sums over the response of all the particles involved in the interaction, which can be written as

$$\mathbf{P}(\mathbf{r}, t) = \mathbf{P}^L(\mathbf{r}, t) + \mathbf{P}^{NL}(\mathbf{r}, t). \tag{2.12}$$

The two parts of $\mathbf{P}$ correspond to the linear and nonlinear response of the medium. The $\mathbf{P}^L$ term accounts for the effects of index of refraction and absorption (or gain). The $\mathbf{P}^{NL}$

term accounts for the effects of nonlinear absorption (or gain) and the effects involving frequency conversion. When the spectral components of the pulses are near the resonance of the medium, the medium cannot be treated classically. Instead, the quantum description, using Maxwell-Bloch equations, must be used. For inhomogeneously broadened material, $\mathbf{P}$ is the integral over the spatial coordinates of the beam, which could be different from spot to spot depending on local uniformity. But for homogeneously broadened material, all the particles are equivalent when pulses are relatively long, i.e. when that the pulse duration is longer than the dephasing time of the medium. We will consider homogeneously broadened medium only.

In the simplest situation, $\mathbf{P}^{NL} = 0$, which means that the response of the medium does not change with incident pulses' intensity. This situation is justified when a relatively weak pulse passes through a medium with its frequency components far away from the media's resonances. Eq. 2.11 can be rewritten and simplified to a scalar equation along x axis:

$$\left(\frac{\partial^2}{\partial x^2} - \frac{1}{c^2} \frac{\partial^2}{\partial t^2} \right) \tilde{E}(x,t) = \mu_0 \frac{\partial^2}{\partial t^2} P^L(x,t), \tag{2.13}$$

with

$$P^L(x,t) = \epsilon_0 \int_{-\infty}^{t} dt' \chi(t') E(x, t-t'), \tag{2.14}$$

where ϵ_0 is the electric susceptibility in vacuum and χ is the dielectric susceptibility of the medium. Eq. 2.14 describes the medium's response as a convolution integral, which reflects the frequency filtering effect of the medium. The filtering effect caused by the finite response time (or bandwidth limit) of the medium gives rise to dispersion. In frequency

domain, Eq. 2.14 and Eq. 2.13 become

$$\tilde{P}^L(x,\omega) = \epsilon_0 \chi(\omega) \tilde{E}(x,\omega), \tag{2.15}$$

and

$$\left[\frac{\partial^2}{\partial x^2} + \frac{\omega^2}{c^2} \epsilon(\omega) \right] \tilde{E}(x,\omega) = 0, \tag{2.16}$$

where $\epsilon(\omega) = 1 + \chi(\omega)$ is the dielectric constant. The solution of Eq. 2.16 is the product of

the transfer function of a linear system and the input wave,

$$\tilde{E}(x,\omega) = \tilde{E}(0,\omega)e^{-ik(\omega)x}, \tag{2.17}$$

where

$$k^2(\omega) = \frac{\omega^2}{c^2}\epsilon(\omega) = \frac{\omega^2}{c^2}n^2(\omega). \tag{2.18}$$

Note that the $k(\omega)$ used here is a real frequency-dependent wave vector when there is no

gain or absorption.

For a Gaussian pulse, after traveling through an optical media, its envelope changes.

The field of a Gaussian pulse is given in Eq. 2.2. When $x = 0$, the Fourier transform of a

Gaussian pulse is given by Eq. 2.3. By substituting the field in Eq. 2.17 with the Gaussian

pulse, we obtain the spectrum of the Gaussian pulse after traveling a distance of x,

$$\tilde{E}(x,\omega) = \left(\frac{\pi}{\Gamma}\right)^{1/2} E_0 exp\left[-\frac{(\omega - \omega_l)^2}{4\Gamma} \right] exp(-ik(\omega)x). \tag{2.19}$$

$k(\omega)$ can be expanded around the carrier frequency as

$$k(\omega) = k_l + k'(\omega - \omega_l) + \frac{1}{2}k''(\omega - \omega_l)^2 + ..., \tag{2.20}$$

where k_0 is the index of refraction of the medium at frequency ω_l (or λ_l),

$$k' = \left[\frac{dk(\omega)}{d\omega}\right]_{\omega_l} = \left[\frac{1}{c}n(\lambda) - \frac{\lambda}{c}\frac{dn(\lambda)}{d\lambda}\right]_{\lambda_l}, \qquad (2.21)$$

and

$$k'' = \left[\frac{d^2k(\omega)}{d\omega^2}\right]_{\omega_l} = \left[\frac{\lambda^3}{2\pi c^2}\frac{d^2n(\lambda)}{d\lambda^2}\right]_{\lambda_l}. \qquad (2.22)$$

Applying Eq. 2.20 to the second order to Eq. 2.19, the pulse spectrum becomes

$$\tilde{E}(\omega, x) = \left(\frac{\pi}{\Gamma}\right)^{1/2} E_0 exp\left[-ik_l x - ik'x(\omega - \omega_l) - \left(\frac{1}{4\Gamma} + \frac{i}{2}k''x\right)(\omega - \omega_l)^2\right]. \qquad (2.23)$$

The time evolution of the electric field now can be derived from the inverse Fourier transform of Eq. 2.23 as

$$\tilde{E}(t, x) = \left[\frac{\Gamma(x)}{\Gamma}\right]^{1/2} E_0 \, exp\left[i\omega_l\left(t - \frac{x}{v_\phi(\omega_l)}\right) - \Gamma(x)\left(t - \frac{x}{v_g(\omega_l)}\right)^2\right], \qquad (2.24)$$

where

$$v_\phi(\omega_l) = \left(\frac{\omega}{k}\right)_{\omega_l}, v_g(\omega_l) = \left(\frac{d\omega}{dk}\right)_{\omega_l}, \qquad (2.25)$$

and

$$\frac{1}{\Gamma(x)} = \frac{1}{\Gamma} + 2ik''x \qquad (2.26)$$

are respectively the phase velocity, the group velocity, and the shape factor. k'' can be rewritten as

$$k'' = \frac{d}{d\omega}\left(\frac{1}{v_g(\omega)}\right)_{\omega_l} = \frac{1}{v_g{}^2}\left(\frac{dv_g}{d\omega}\right)_{\omega_l}, \qquad (2.27)$$

which is called the group velocity dispersion(GVD) parameter [8, 7]. Rewriting $\Gamma(x)$ as

$$\Gamma(x) = \frac{\Gamma}{1 + 4k''^2x^2\Gamma^2} + \frac{-2ik''x\Gamma^2}{1 + 4k''^2x^2\Gamma^2} = A_\Gamma(x)exp[i\phi_\Gamma(x)] \qquad (2.28)$$

and substituting Eq. 2.28 into Eq. 2.24 yield

$$\tilde{E}(t,x) = A_\Gamma(x)\, E_0\, exp\left[i\omega_l\left(t - \frac{x}{v_\phi(\omega_l)}\right)\right]\, exp\left[-\frac{\Gamma}{1 + 4k''^2 x^2\Gamma^2}\left(t - \frac{x}{v_g(\omega_l)}\right)^2\right]$$

$$\times exp\left[\frac{2ik''x\Gamma^2}{1 + 4k''^2 x^2\Gamma^2}\left(t - \frac{x}{v_g(\omega_l)}\right)^2 + i\phi_\Gamma(x)\right], \qquad (2.29)$$

where

$$\phi_\Gamma(x) = -arctan(2x\Gamma k'') . \qquad (2.30)$$

As shown in Eq. 2.29, the phase velocity is responsible for the phase delay of the carrier in the medium, the group velocity causes a time delay to the Gaussian envelope, and the pulse's Gaussian shape remains with changed amplitude and shape factor.

In the second term to the last in Eq. 2.29, the Gaussian shape factor becomes smaller due to the existence of k'', which indicates pulse broadening. The last term shows the phase changes as a function of time and distance. Since the phase change is a function of time, it causes a frequency chirp. Thus, this pulse is no longer Fourier-transform-limited.

Depending on the GVD parameter of the medium, the chirp in the last term of Eq. 2.29 can be either positive or negative. When the wavelength is far from any resonance line of a medium, k'' is positive, which is the common case for optical glass. When a FTL pulse travels in a medium with $k'' > 0$ which causes $d^2\phi/dt^2 > 0$, the pulse will be up-chirped. After traveling a distance in optical glass, the instantaneous frequency of the pulse shows more red components in the leading part and more blue in the trailing part.

2.1.3 Beam Optics

So far we have treated pulses as a propagating plane wave, which is a simplified model of the real situation. To generalize the analysis above, we must include the beam profile of an optical pulse,

$$\tilde{E}(x,y,z,t) = \tilde{u}(x,y,z)\tilde{E}(z,t)e^{-i(\omega_l t - k_l z)}, \tag{2.31}$$

where, $u(x,y,z)$ is a function describing the transverse profile of the pulse. A laser beam is called a paraxial wave when its transverse size is much larger than the wavelength λ. The propagation of a paraxial beam can be calculated using Fresnel approximation based on Huygens' principle. In practice, a Gaussian beam is commonly used to model a laser beam under the assumption of the slowly varying envelope approximation (SVEA), i.e. the change of profile over one wavelength distance is small. A Gaussian beam can be written as

$$\tilde{u}(x,y,z) = \frac{u_0}{\sqrt{1 + x^2/\rho_0^2}} e^{-i\Theta(x)} e^{-ik_l(y^2+z^2)/2R(x)} e^{-(y^2+z^2)/w^2(x)}, \tag{2.32}$$

where

$$R(x) = x + \rho_0^2/x, \tag{2.33}$$

$$w(x) = w_0\sqrt{1 + x^2/\rho_0^2}, \tag{2.34}$$

$$\Theta(x) = arctan(x/\rho_0), \tag{2.35}$$

and

$$\rho_0 = n\pi w_0^2/\lambda_l, \tag{2.36}$$

where u_0, w_0, and λ_l are the field strength at the waist of the Gaussian, beam waist (radius), and wave length of the carrier, respectively. The origin of Eq. 2.32 $x = 0$, is chosen at the

beam waist. ρ_0 is known as the Rayleigh range describing the longitudinal focusing of the beam. For a pulse with given carrier frequency, once knowing the position and width of waist, we can predict the propagation of its field using Eq. 2.32- 2.35. In ultrafast laser systems, tight focus of the laser beam on the gain medium is commonly used since it enhances the nonlinear effects. It is often useful to know the beam size, i.e. the waist of the Gaussian beam, in the gain medium. The incident angle of the beam entering the medium is usually at the Brewster angle in order to reduce the loss. The incident angle and the beam waist can be calculated directly by measuring the reflection off the medium's surface. Inserting Eq. 2.36 into Eq. 2.34 and solving for w_0, we have

$$2w_0^2 = w^2(x) - \sqrt{w^4(x) - 4\left(\frac{\lambda_0}{n\pi}\right)^2 x^2}, \tag{2.37}$$

where $w(x)$ is the radius of the beam at x.

2.2 Ultrashort Pulse Measurement

A single pulse can be fully characterized by the amplitude and phase of its frequency components and its temporal polarization. In experiments, the measurement of certain properties of the pulse is often needed rather than a full characterization. The power and spectral profiles of the optical pulse can be easily obtained with conventional instruments. But to obtain the time profile and phase information, new techniques are needed. The methods proposed in early years of ultrashort pulse generation mostly focused on the measurement of pulse duration, including two-photon fluorescence, streak camera, optical Kerr gating, and optical correlation [10]. Later development in measuring methods allowed retrieving

of the profiles, phase, and polarization information of the pulses. These methods include various frequency-resolved optical gating (FROG) methods [11, 12], spectral phase interferometry for direct electric-field reconstruction (SPIDER) [13], and dual-channel spectral interferometry [14].

Direct measurement using a photo-detector with electronic devices is limited by its slow picosecond time scale response, which is good for fluence measurement, but not adequate for the time profile or duration measuring of femtosecond pulses. For ultrafast systems that produce trains of pulses with a very high repetition rate, photo-detectors can be used to measure the pulse fluence and to study the stability of the pulses, where complicated optical techniques of pulse characterization are often too slow to use. Photodiodes and photo multiplier tubes (PMT) are two commonly used photo-detectors because of their short (<ns) response time.

The autocorrelation method was one of the first methods that were proposed and demonstrated, and is widely used in experiments due to its simplicity and versatility (1966) [10]. In this work, we used this technique to measure the duration of the pulses in a high-repetition-rate pulse train.

The optical correlation technique is based on the nonlinear process of second harmonic generation (SHG) in an optical crystal. In an autocorrelator the input pulse passes through a Michelson interferometer, then its two pieces recombine on a phase-matched nonlinear optical crystal to generate a second harmonic signal. By varying the delay time in one arm of the interferometer, the second-order correlation function of the input pulse's intensity can be obtained. The second-order autocorrelation function of a pulse's intensity, I, is given in

the form of

$$G^2(\tau) = \frac{< I(t)I(t+\tau) >}{< I^2(t) >},$$ (2.38)

where τ is the relative delay time, and the bracket implies the averaging of functions over the time. It is easy to see in Eq. 2.38, that the output is always symmetric. So, the knowledge of the precise profile of pulses cannot be acquired using an autocorrelator. Rather, the additional information of higher order correlation is needed. For given pulse shapes, the autocorrelator can be used to measure the pulse duration [10, 15]. For the Gaussian pulse in Eq. 2.2, the FWHM duration of its autocorrelation function is $\tau = (ln\ 2/\Gamma)^{1/2}$ or $t_p = \tau/1.41$.

The experimental setup of an autocorrelator can be very versatile. Various autocorrelation traces can be obtained depending on the ways to overlap beams in the crystal and the types of phase-matching employed. Interferometric autocorrelation traces can be obtained by collinearly overlapping beams in the crystal. Background-free traces can be obtained using either the method of beams crossing in the crystal or the method of collinearly overlapping of differently polarized beams. The autocorrelator we used as shown in Fig. 2.1 belongs to the latter category.
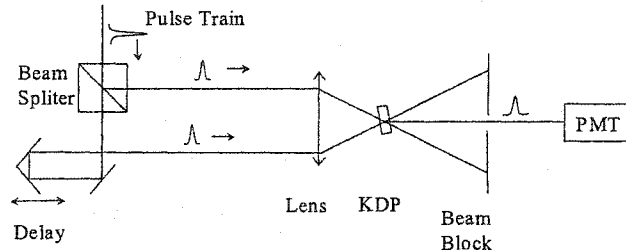
Figure 2.1: The background-free configuration of an autocorrelator.

2.3 Key Ultrafast Techniques

An ultrashort optical pulse has a very broad spectrum. To construct an optical pulse, the amplitudes and phases of various frequency components of the pulse must behave in an orderly way. The technique of achieving fixed phase and amplitude relationship between longitudinal modes in a laser is called mode-locking [16]. We will give a short introduction of mode-locking techniques in Section 2.3.1. The dispersion of an ultrafast system has significant influence on the duration of the pulses as well as the stability of the system. So, modern systems usually use dispersion control technique to adjust the intracavity dispersion. Section 2.3.2 briefly introduces the origin, description, and control of dispersion in ultrafast lasers.

2.3.1 Mode-locking

Most ultrafast systems use mode-locking techniques to produce ultrashort pulses. An ultrafast laser system must have a broad bandwidth to allow for many longitudinal modes in order to generate short pulses. When various modes are locked in phase and amplitude in an ultrafast laser, ultrashort pulses with stable shape are generated. Mode-locking in a laser can be realized by modulating the intensity, loss, or phase of the laser.

When a laser is mode-locked, its electric field $E(t)$ can be written as

$$\tilde{E}(t) = \sum_{n=-\infty}^{+\infty} E_n exp(i\omega_n t) , \qquad (2.39)$$

where the frequencies ω_n of the different modes are distributed around a carrier frequency ω_l, with

$$\omega_n = \omega_l + n\Delta\omega . \qquad (2.40)$$

$\Delta\omega$ is the frequency interval between two adjacent longitudinal modes, $\Delta\omega = 2\pi c/2L$, where

L is the cavity length of the system. Using Eq. 2.40, we can rewrite Eq. 2.39 as

$$\tilde{E}(t) = exp(i\omega_0 t) \sum_{n=-\infty}^{+\infty} E_n exp(in\Delta\omega t) \,.$$ (2.41)

If $E_{-n} = E_n^*$, Eq. 2.41 is a real-valued periodic function with a period of

$$T = 2\pi/\Delta\omega.$$ (2.42)

Eq. 2.39 - 2.41 describe the spectrum of a train of pulses instead of one pulse, therefore, the spectrum is discrete rather than continuous as that in Eq. 2.3. The period T arises from the beating between modes. The Fourier transform of the formula in Eq. 2.41 shows a train of pulse with carrier frequency ω_l and adjacent pulses separated by the time T.

The inverse of the period T is called the repetition rate. When only a single pulse exists in an ultrafast system, $T = 2L/c$. In an ultrashort pulse train, the time intervals between consecutive pulses may not be the same. The fluctuation of pulse arrival time is called timing jitter. In an actual system, the spacing between modes may vary, which results in timing jitter. These processes are usually caused by environmental temperature changes or acoustic oscillations, which are often slow. Timing jitter also originates from fast processes in which the phases or amplitudes of the pulses' frequency components vary, such as the dynamical evolving of pulses in the cavity and the high frequency modulation on the pump power in the CPM laser. In this kind of processes, the pulse's shape also changes. The change of phase and amplitude of the pulse's frequency components may be caused by either the evolution of pulses in the system or noise.

The process of mode-locking in an ultrafast system is easy to understand in the time domain description. The mode-locking process is usually achieved by inserting a nonlinear loss component into the cavity, which enhances the stronger pulses and inhibits the weaker ones. When the pulses travel around the cavity for many times, only a single strongest pulse survives in the cavity in most cases. During a mode-locking process, each mode is coupled to its adjacent modes by the modulation, which has a frequency the same as the beat frequency between adjacent modes. As the number of modes in a system grows, the pulses' duration shrinks. The process will continue until the pulses' duration is limited by the dispersion or by the finite bandwidth of the gain.

2.3.2 Dispersion Control

Dispersion refers to the phenomenon that the phase velocity of a wave varies with its frequency, i.e. $\frac{dv_p}{d\omega}$ in a medium. Dispersion is usually called normal if $\frac{dv_p}{d\omega} > 0$ (or $\frac{dn}{d\omega} < 0$), and anomalous if $\frac{dv_p}{d\omega} < 0$ (or $\frac{dn}{d\omega} > 0$). Due to ultrashort pulses' very broad spectrum, they are subject to significant influence of the dispersion in an optical system. The dispersion causes time delay and broadening of pulses traversing the medium. The importance of dispersion in ultrafast systems was recognized soon after the generation of sub-picosecond pulses. The uncompensated intracavity dispersion in picosecond laser systems caused a cumulative chirping effect on ultrashort pulses preventing these systems from generating FTL pulses. The chirping effect subsequently limited the generation of femtosecond pulses in those systems.

The intracavity GVD can be compensated using prism pairs, which leads to the generation of pulses shorter than 100 fs. In extremely short pulse generation, the control of

intracavity third- and fourth-order dispersion (TOD and FOD) becomes critical. It has been demonstrated that TOD can be eliminated and FOD be limited by using chirped mirrors. Dispersion also plays an important role in the compression of a laser pulse outside laser cavity. The control of dispersion in an optical compressor is easier than that in a laser cavity since no cumulative effect is involved [17].

In this section, we will briefly discuss the origin, description and compensation of dispersion in ultrafast systems. For simplicity, the spatial distribution of dispersion is left out. In some ring lasers such as our CPM laser, the field of a pulse after each round trip is its mirror image, which reduces the transverse spatial dispersion.

The dispersion in an ultrafast laser arises when pulses travel through or reflect from an optical medium. Because of ultrashort pulses' high intensity, the interaction between ultrashort pulses and the optical elements involves processes such as linear and nonlinear absorption and gain, self-phase modulation (SPM), harmonic generation, and Raman processes. The SPM is the major source of dispersion in ultrafast lasers. The dispersion caused by the reflection from dielectric mirrors is usually very small.

The geometric dispersion produced by prismatic or interferometric devices can be used to compensate for intracavity dispersion in ultrafast systems. The most commonly used dispersion-compensating devices are prism pairs, chirped mirrors, or grating pairs. In these devices, different frequency components of a pulse take different optical paths. The control of the second and third order of dispersion can only be realized by a combination of various dispersion control devices. The reduction of higher orders of dispersion is usually achieved by minimizing the materials in the cavity of an ultrafast system.

The dispersion of an optical pulse can be represented by the relative phase delays of its

frequency components. When waves traverse a sample of optical media, the phase velocity

follows the first formula in Eq. 2.25.

In a linear system, the output electric field can be related to the input by

$$\tilde{E}_o(\omega) = \tilde{S}(\omega)\tilde{E}_i(\omega), \tag{2.43}$$

where $\tilde{S}(\omega)$ describes the transfer function of the system, which is the Fourier transform

of the system's impulse response function. The argument of $\tilde{S}(\omega)$ is the phase transfer

function, $\phi(\omega)$, which shows the accumulated phase changes for different frequencies caused

by the optical system. As pointed out by Walmsley et $al.$, given a fixed spectrum width,

the shortest pulse must have a constant spectral phase function, i.e. $d\phi/d\omega = 0$ [9]. $\phi(\omega)$

is very useful in the design and analysis of ultrafast optical systems. Eq. 2.43 can then be

rewritten as

$$\tilde{E}_o(\omega) = e^{i\phi(\omega)}\tilde{E}_i(\omega). \tag{2.44}$$

When the pulse's spectrum is far away from the material resonance lines, e.g. in the

case of traversing a piece of glass, its phase transfer function is,

$$\phi(\omega) = \frac{\omega}{c}n(\omega)L, \tag{2.45}$$

where L is the thickness of the sample. Eq. 2.45 is a universal process happening in any

medium and is indifferent to the intensity of the pulse. When the beam is tightly focused, an

ultrashort pulse has very high intensity on the focal point. In this case, the high intensity of

a pulse will cause a nonlinear change of index of refraction in the optical medium, which is

known as the optical Kerr effect. The lowest order of this nonlinear effect can be described

as

$$n(\omega) = n_0 + n_2|\tilde{E}(t)|^2 = n_0 + \bar{n}_2 I(t), \tag{2.46}$$

where $\bar{n}_2 = 2n_2/(\epsilon c n_0)$. The intensity dependent property of the Kerr effect implies that the index of refraction varies in both time and space, which in turn causes the phenomena of self-phase modulation (SPM) and self-focusing (or -defocusing) of pulses respectively. SPM is an essential process in an ultrafast laser. When an ultrafast laser self-starts from noise, it takes many round trip times for longer pulses to evolve into shorter ones before the laser is stabilized. During this time, the SPM caused by the pulse intensity gives rise to the generation of new frequency components in the laser. So, it is sometimes preferable to focus the laser beam tightly to enhance the SPM effect. In the self-focusing process the laser beam converges. Very tight focusing may complicate the spatial distribution of the laser beam. When a strong laser pulse is focused tightly in a medium, the laser's beam quality deteriorates. The beam may break into many filaments or cause damage to the medium.

Our CPM laser uses two prism pairs as the dispersion compensation device. Appendix A shows the arrangement of the two prism pairs with a detailed dispersion analysis. In this device, the output beam collimates with the input beam. Different frequency components of the pulse will travel through different lengths of air and material in the prism sequence, i.e. different optical paths, so that a controllable dispersion is produced.

Chapter 3

The CPM Ring Dye Laser

The first dye laser was reported in 1966 by Sorokin and Lankard [18]. This report started the successful developments of many dye lasers including the CPM laser. In this chapter, we will review the evolution of the CPM laser in Section 3.1. Section 3.2 will give a detailed description of our CPM laser, which is a typical system among all CPM lasers. Finally, we will introduce the principles of CPM laser using rate equations in Section 3.3.

3.1 Evolution of the CPM Laser

The CPM laser relies on saturation effects of its dyes to produce ultrashort pulses. The saturation of the absorber is enhanced by the colliding pulse technique. During its development, the CPM laser's cavity evolved from linear to ring cavity to facilitate the colliding pulse action to produce ultrashort pulse and achieve stable running operation. Meanwhile, other techniques, such as dispersion control, were included into the CPM laser. In this section, we will review the CPM laser's development chronologically, starting with a short introduction of the properties of dye lasers.

3.1.1 General Properties of Dye Lasers

Laser dyes have the favorable property of very broad emission and absorption spectrum. Dye lasers cover a large range of frequencies. They are easy to pump, versatile, and often tunable. Though laser dyes can be used in solid or gas phase, they are most often used in liquid phase. When used in a solvent, the dye laser is under good control because the concentration of dye is easy to change, and the solvent can easily be circulated, chilled and self-repaired.

In a dye laser, the active dye media is commonly pumped to singlet-state, S_2, from which the particles quickly relax to singlet-state S_1. The laser action happens between S_1 and the ground state. Many different vibrational and rotational modes are coupled to the electron transitions when the dye molecule is big. In the solvent, thermal equilibrium is rapidly reached with collisions happening at about 10^{12} times per second. The collisions, together with the coupling between energy-levels, can homogeneously broaden the spectrum width of dye's energy states to several tens of nanometers. For example, the widely used Xanthene dye, Rhodamine 6G, has an emission spectrum range from 560 to 635 nm(0.53 to 0.47×10^{15} Hz).

The performance of a dye laser can be affected by many factors, such as the temperature, aging of the dye, different solvents, influence of triplet levels, generation of photo-isomers, and shapes of the dye container or jet. Therefore, it is usually difficult and complicated to analyze dye lasers.

The broad energy levels of laser dyes make them attractive candidates for the active media used in mode-locked lasers. With relatively large absorption cross-sections, some

organic dyes can be saturated with moderate photon fluence, therefore, absorbers consisting of dye solutions are also widely used. Laser dyes are also used in ultrashort pulse amplifiers.

3.1.2 The CPM Laser

Mode-locking in dye lasers using an intracavity saturable absorber dye cell was first demonstrated in a flashlamp-pumped dye laser (1968) [19]. Due to the limited time available for the shaping mechanism to take effect, the pulses generated in this system were longer than a few picoseconds. An important improvement was made when passive mode-locking of a CW dye laser was first achieved by Ippen *et al.* (1972) [4]. Their design includes most of the essential components of today's ultrafast dye laser.

In their experiment, Ippen *et al.* used a linear cavity consisting of a gain cell, an absorber cell, and five mirrors. The pump beam from an argon ion laser was coupled into the cavity by a prism. Rhodamine 6G in water and DODCI (3,3'-diethyloxadicarbocyanine iodide) in methanol were the gain and absorber medium, respectively. The intracavity laser beam was tightly focused on the gain and absorber to effectively deplete the gain and saturate the absorber. The system ran best near threshold. When the pump was a little higher than threshold, multiple pulses showed up in each round-trip time due to the mismatch between cavity round trip time and the gain's relaxation time. The pulse was chirped and its duration was measured to be about 1.5 ps with an spectrum width less than 1 Å. Later, by replacing dye cells by jets to reduce the number of optical surfaces in the cavity (1973) [20] and mixing the absorber and gain dyes together, a similar setup produced sub-picosecond pulses (1974) [21].

At this time, New [22, 23] and Haus [24] published their theoretical analysis of the

mode-locked CW laser. New realized the importance of putting the absorber close to the end mirror to form a standing wave from the leading and trailing parts of the pulse. The density needed to saturate the absorber by a standing wave was 3 times less than that of a traveling wave [23]. By applying New's concept of colliding to the mode-locked CW dye laser, Ruddock and Bradley generated pulses as short as 0.3 ps directly (1976) [25]. In their system, a pulse was focused on the absorber to effectively saturate the absorber. This system also had improved stability and allowed for a larger variable range of pump power. In an effort to reduce the spectrum filtering effect of the intracavity elements, a dye jet with mixed gain and absorber dyes was used in the same setup. Pulses as short as 120 fs were observed in this system (1978) [26].

Fork *et al.* introduced the colliding pulse mode-locking concept (1981) [27, 28]. They used two counter-propagating pulses to *collide* in the absorber to form a standing wave. Since the total energy density doubled compared with previous design, the loss was reduced when two synchronized pulses collided in the absorber. Applying the colliding pulse process to a ring cavity, they were able to obtain pulses as short as 90 fs with high quality (about 1% rms). In this system, two counter-propagating pulses emerging from noise passively, self-synchronized to minimize the loss caused by the absorber.

The CPM technique was also realized in linear cavities. In such cavities, there were two or more pulses existing in the cavity at any time. The absorber's position needed to be very accurately aligned to be a sub-multiple of the cavity length away from one end mirror. The accuracy required in the alignment was on the order of the pulse width. For instance, a 90 fs pulse has a pulse length of 27 μ m. Therefore, the CPM linear cavity system was hard to maintain. When more than two pulses existed in the cavity, the mismatch between

the relaxation time of gain and cavity length could also cause fluctuation of the pulses' amplitude. One special case for this scheme was the system demonstrated by Bradley [29], which used an absorber contacted to one end mirror and one pulse *colliding*.

The spectrum width limitation in the CPM laser was the next difficulty to overcome. By carefully selecting the mirrors used in the CPM laser, 55 fs-pulse trains were generated directly (1983) [30]. Then, the CPM mechanism was studied in detail, which revealed that pulses generated in the CPM laser were negative chirped rather than Fourier-transform-limited. In theory, the important role of SPM and GVD was elucidated. In experiments, intracavity dispersion control and external cavity pulse compression were explored.

Using intracavity prismatic dispersion to correct dispersion in ring dye laser was first demonstrated by Dietel *et al.* with outputs shorter than 60 fs (1983) [31]. Fork proposed the paired-prism design which was quickly adopted to improve the CPM laser. By 1985, intracavity compression with one or two pairs of prisms was demonstrated by a few groups [32, 33].

This knowledge culminated with the shortest pulse, 27 fs, ever generated directly from the CPM laser in 1985 [34]. The intracavity dispersion and GVD were carefully balanced with two pairs of prisms. By changing the position of the prism in the cavity, both negative and positive GVD could be provided by the two prism pairs. It was also observed that the shortest pulses could only be produced with fresh dyes.

In parallel with the evolution of the CPM laser, the techniques of amplifying and pulse compressing were developed as well. In the very early development of ultrafast technology, the ideas of using SPM to broaden pulses' spectrum [35] and using a grating pair to compress pulses [36] were proposed. By incorporating these ideas into a fiber and grating-pair setup,

Shank *et al.* compressed 90 fs pulses generated from the CPM laser to 30 fs in 1982 [37].
It was pointed out by Treacy that a grating pair is able to compensate the quadratic phase
distortion, but not cubic distortion [36]. Fork *et al.* demonstrated that a combination of
two pairs of grating and two pairs of prism can be adjusted to compensate both quadratic
and cubic dispersion (1987) [38]. Consequently, they amplified the pulses produced by the
SPM and GVD balanced CPM dye laser and ran them through the fiber compressor [37]
with the new combination instead of a grating pair. They generated pulses as short as 6
fs, or three cycles of the carrier oscillation at 620 nm, which was a record for more than
a decade. This record was broken only in very recent years with pulses as short as 4.5 fs,
or two optical cycles (1997) [17]. Further shortening of pulse in the CPM laser is limited
by minor effects such as spectrum broadening ability of the SPM, higher order dispersion,
four-wave mixing type coupling, and two-photon absorption in dye jets [39]. The chronology
of the shortest pulse produced by CPM lasers is shown in Fig. 3.1.
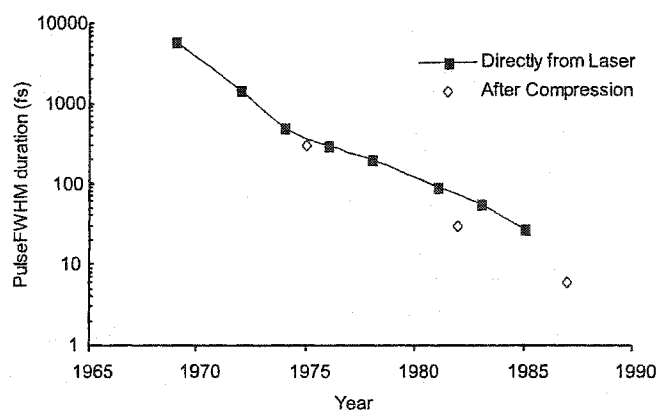
Figure 3.1: The time chronicle of shortest pulse produced by CPM lasers.

The mirrors used in ultrafast dye lasers used to be an important source of spectrum
filtering and dispersion. This situation has been improved during the development of the

CPM laser, and the spectrum filtering effect has now been almost removed by the invention of chirped mirrors [40]. Broadband multilayer dielectric mirrors are more often used in ultrafast dye lasers than the commonly used narrow-band single stack dielectric mirrors and metallic coated mirrors. For a broadband multilayer dielectric reflector, the interference of reflections from the layers causes frequency-dependent phase shift in reflected waves, which may in turn cause distortion and pulse broadening. This kind of dispersion can usually be corrected together with dispersion caused by other intracavity optics. The dispersion of the intracavity mirror surfaces have been studied in detail and proved to be minor and compensable in most cases [41, 8, 42]. The chirped mirror was introduced in the 1990s, which generates a dispersion function desired by reflecting different frequency components from different depths. Before the birth of the chirped mirrors, ultrafast dye lasers had been able to utilize the full spectrum of the gain. Therefore, the chirped mirror never played a role as important as that in solid-state ultrafast lasers.

In a typical CPM ring laser with two prism pairs, there are 18 to 19 optical surfaces inside the cavity. Therefore, the loss on optical surfaces due to the poor alignment of ring cavity is hardly avoidable. This problem has been partly solved by the introduction of the antiresonant ring. The antiresonant ring works the same way as the dye-contacted end mirror, but by splitting one pulse using a beam splitter and make the two pieces to collide in the absorber in a ring design. This ring can be used to terminate the linear CPM cavity, therefore, the antiresonant ring terminated CPM laser has the advantage of easy adjustment of cavity length as well as easy alignment of the cavity. But this kind of laser never achieved the same quality as the CPM ring laser due to the weakening of colliding effect.

The evolution of the cavity scheme of CPM lasers is shown in Fig. 3.2.
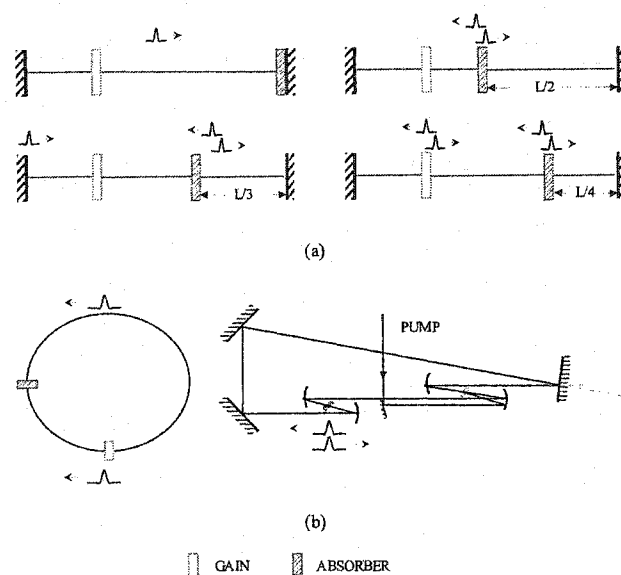
Figure 3.2: The evolution of the CPM laser cavity. (a) shows the early linear versions of colliding pulses mode-locking; (b) The current CPM laser has a ring cavity with its absorber and gain carefully positioned to best utilize the gain.

3.2 The Description of the CPM Laser

The CPM laser we studied uses a typical setup as shown in Fig. 3.3, which is just slightly different from the ring cavity used by Valdmanis and Fork as shown in Fig. 3.2(b) [43]. The system consists of an external pump laser, an absorber dye jet, a gain dye jet, 6 mirrors, and 4 prisms. The counter-propagating laser beams traversing the cavity are tightly focused on the absorber and the gain jets by two pairs of confocal concave mirrors. The pump beam is also focused on the gain by another confocal mirror. The optical properties of these components determine the characteristics of the pulses. In this section, we will discuss the basic design considerations followed by a detailed description of these components [44].
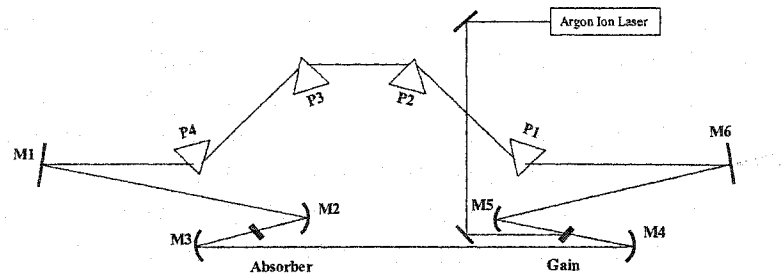
Figure 3.3: The scheme of the CPM laser we studied in this thesis.

3.2.1 Ring Cavity

In our CPM laser, all the cavity mirrors are normal incidence, single stack, dielectric high reflectors centered at 620 nm, allowing for a bandwidth well beyond the spectral range of its dyes. The cavity design of the CPM laser allows good transverse mode stability [43]. The cavity is setup in a compact way that the incident angle on each mirror is never significantly deviated from the normal to the mirror surface. This design best avoids the possible dispersion and bandwidth limiting effect of the mirrors.

The round-trip cavity length of our CPM laser is approximately 3 m. The separation between the gain and the absorber is approximately 70 cm, roughly a quarter of the cavity length. The separation between the gain and the absorber is designed to match their relaxation times. The separation does not need to be exact since the positioning difficulty is much alleviated in this system, but it is limited by the requirement to form a uniform beam waist in the cavity. In ring lasers with two tight focusing points, this problem of transverse mode stability was studied using ABCD matrices introduced by Kogelnik and Li (1966). The stability range for the ring laser with round-trip cavity length around 3 m turns out to be within a few centimeters, which makes the alignment much easier [34, 39].

The beam in the cavity has a diameter (2ω) of about 2 mm. The output coupler has an one percent transmission. The focal lengths of the confocal mirrors around the gain and absorber are 5 and 3.75 cm which make the active areas ($\pi\omega_0^2$) in them 300 and 172 μm^2, respectively.

The pump beam is focused by a separate mirror to allow for more flexibility in the alignment and the adjustment of spot size. This configuration also avoids the difficulty of choosing mirrors, which must be highly reflective in both the pump and the laser wavelength otherwise.

3.2.2 The Gain and the Absorber

The solution of Rhodamine 6G in Ethylene Glycol (EG) is used in the gain jet. Normally, we use the solution with a concentration of 1. 5g/l (or 3.1×10^{-3}mol/l). The gain medium is a very thin stream of dye solution produced by a high-pressure dye jet. The thickness of the stream depends on the size of the nozzle and the pumping pressure. The dye solution is pumped by a DC motor and is chilled while circulating. The pump connects to the jet via flexible tubes allowing for vibration-free operation. In our system, we measured the thickness of the gain jet to be 50 μm.

The solution of DODCI in EG is used in the saturable absorber. The concentration of the solution that we normally use is 0.037 g/l (or 7.5×10^{-5}mol/l). The absorber uses the same technique to produce its dye solution stream, which has a thickness of 35 μm.

The molecular structure and weight of these two kinds of dyes are shown in Fig. 3.4. Each dye jet is mounted on a 3-dimensional translation stage, which allows it to translate in vertical direction, along the beam, and normal to the beam. The absorber can be moved

out of and in the beam path while aligning the cavity.

$C_{28}H_{31}N_2O_3Cl$ MW: 479.02

Rhodamine 6G

$C_{23}H_{23}N_2O_2I$ MW:486.35

DODCI(3,3'-Diethyloxadicarbocyaninie Iodide)
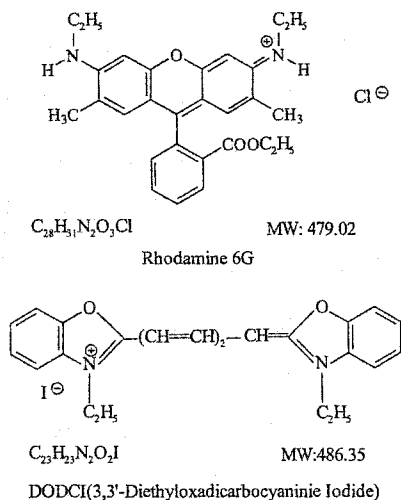
Figure 3.4: The molecule of the gain and the absorber dyes.

The nonuniformity in the active area in jet flow arises from vibrations of the mounts, un-removed pulsatile pumping, irregularity on nozzle, and surface waves. In our CPM laser, the nozzle is made of stainless steel.

The laser dyes are chilled to increase their usable life time. DODCI and Rhodamine 6G degrade on a similar time scale of 1-3 weeks in a daily-used CPM laser. So, frequently the pump systems need to be flushed and filled with freshly prepared dyes. We observed that the laser is significantly unstable with fresh dyes comparing to that with not-so-fresh dyes. The Rhodamine 6G degradation can be observed by the increasing olive color in the dye solution, while DODCI solution just becomes notably transparent when it ages. The aged Rhodamine 6G has a narrower fluorescence spectrum comparing with fresh dye and tends to absorb more in the red. The overall aging effects cause the laser to operate at shorter wavelength and to produce longer pulses.

3.2.3 Prism Sequence

The four fused silica prism sequence incorporated in the CPM laser serves as a GVD control component. All incident angles on the surfaces of prisms are near the Brewster angle of 43.3^o. The optical paths at the ends of the sequence are collimated to the path when the prisms are removed from the cavity.

The prisms are mounted on tilt and translation stages. The translation along the direction of the prism apex allows the prisms to fully intersect with the laser beam. In an ideal alignment, the prisms lie in the same horizontal surface as the optical beams in the cavity, and the beams pass through the apexes of the prisms. The prism sequence introduces negative GVD in a normal operation. The amount of negative GVD is proportional to the distance between prisms in each pair. A typical number of 27.2 cm for this distance is used in our CPM laser which provides adequate GVD adjustment. The GVD can be adjusted by varying the insertion depth of the prism into the beam.

3.2.4 The Pump Laser

The pump laser in our CPM system is an argon ion laser, which is commonly used for dye laser pumping. The argon ion laser is capable of producing high CW pump power (>4 W) in a good single-spatial mode. In the CPM laser system, it operates in its multiline visible mode with a power level >2.5 W, often at 3.5 W, depending on the CPM laser's condition. In this mode the argon ion laser lases in several lines in the green to blue range. A few of these lines fall into the absorption band of the Rhodamine 6G. But the major pumping energy comes from the strongest line at $514.5nm$. The power source of the argon ion laser is a 3-phase AC current, which makes it susceptible to modulation of the AC current, especially

when the laser is running in its maximum power. Also, the competition and coherence between different modes of the argon ion laser produces high frequency (RF) modulations on the CW output of the argon ion laser. The argon ion laser requires significant water cooling because of its low quantum efficiency.

3.2.5 Basic Operational Characteristics

The operating condition of the CPM laser is very sensitive to the alignment of the optics in the cavity, especially the confocal mirrors around the gain and the prisms. The CPM laser we operated on typically has a threshold at 0.8 W when the prisms and the absorber are pulled out. Due to the prisms' many surfaces, the prism sequence raises the laser threshold by 0.5 W even in good alignment. When both the prism sequence and the absorber present in the cavity, the threshold is typically around 2.7 W. Yet the optimal operation is obtained when the pump level is around 3.5 W. When the system is running under optimal conditions, the CPM laser produces pulses with adjustable durations from 60 to above 200 fs and with a typical average power of 5 - 6 mW in each beam. The repetition rate is around 94.5 MHz so that the energy in each pulse is around 0.053 nJ in the output and 5.3 nJ in the cavity. Assuming the intracavity pulses have the soliton shape, the peak power of the intracavity pulses are as high as 40 kW which yields peak power densities of single pulse of 1.3×10^{10} W/cm^2 in the gain and 2.25×10^{10} W/cm^2 in the absorber.

The wavelength at the peak of the pulse's spectrum is around 620 nm (4.84×10^{14} Hz) with fresh dye, and this wavelength shifts to the blue as the dye ages. The emission spectrum of the gain and the absorption spectrum of the absorber in the CPM laser is shown in Fig. 3.5. The gray area in Fig. 3.5 is the spectral range of the pulses produced

in our CPM laser. This peak wavelength in the pulse's spectrum changes from day to day since it depends on many dynamically changing parameters and processes such as the pump power, intracavity GVD, dye aging, and the Stokes shifts of the dye fluorescence spectrum.
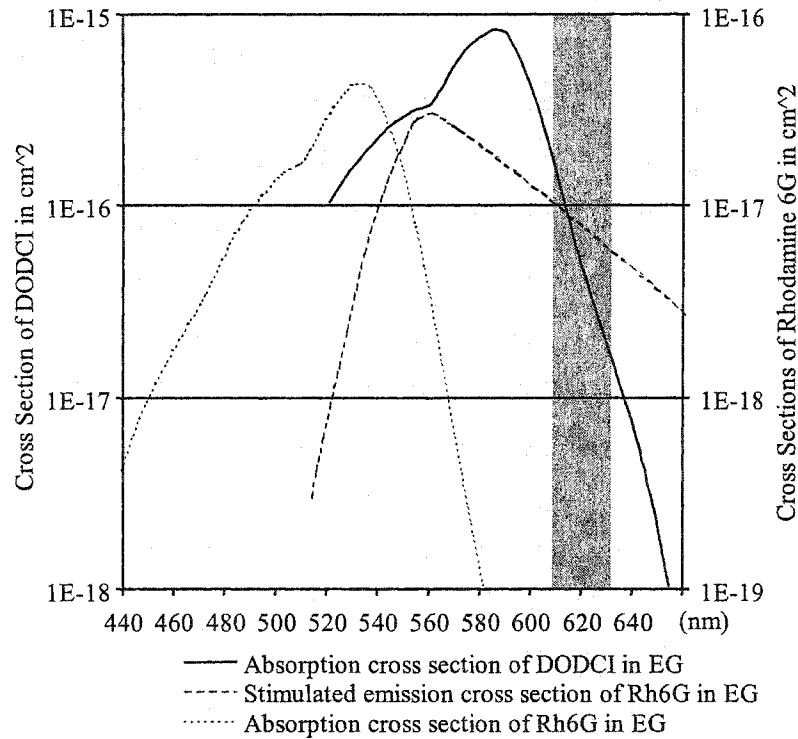
Figure 3.5: The absorption cross section of DODCI and absorption and emission cross sections of Rhodamine 6G and in EG solvent [45].

The CPM laser is rich in transient phenomena. These transient phenomena happen when the CPM laser transits between its possible operation states. Fig. 3.6 shows a simple model describing these transitions.

The stable mode-locking mode is the mode the CPM laser normally operates in. In this mode, the CPM laser produces an ultrashort pulse in each round trip in each output beam. The double pulse mode describes the appearing of additional satellite pulses in the CPM
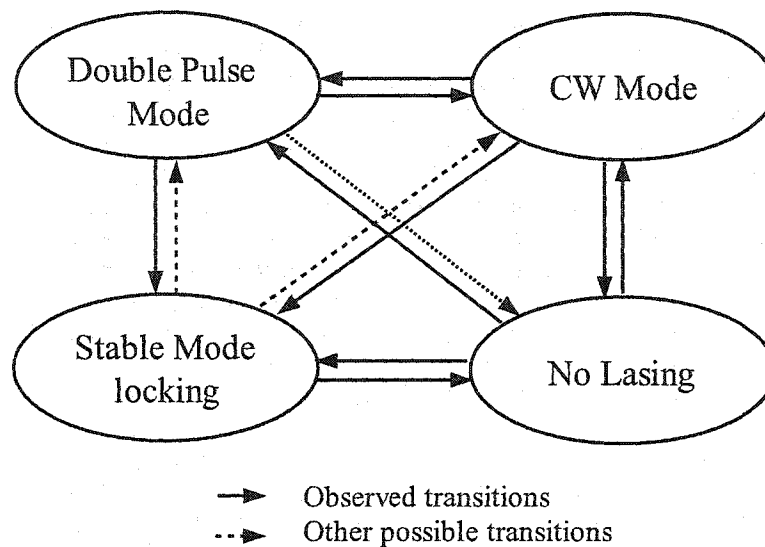
Figure 3.6: The possible states of the CPM laser observed on its output and the transient transitions between them.

laser caused by excessive gain. In this mode, the CPM laser usually produces two ultrashort pulses in each round trip in each beam. The satellite pulse appears about a quarter of the round trip time after the main pulse. Caused by excessive gain or dispersion, in the CW mode, the CPM laser produces very long pulses, a few nanoseconds. The pulses in the two counter-propagating beams have no obvious synchronization as that in the previous modes. The CPM laser may also stop lasing for a brief time before resuming lasing, which is described by the stop lasing mode in Fig. 3.6.

As an example of the transitions, the output power fluctuation of the CPM laser during a dropout and a dropin to the CW mode is shown in Fig.3.7.

In this thesis, we investigated the transitions happening between a stable mode-locking mode and the stop lasing mode, i.e. dropout and dropin processes.
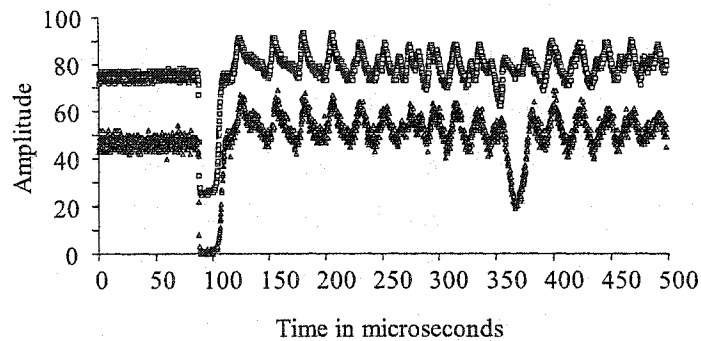
Figure 3.7: The data used here is generated by our data processing program with a 500 points fitting window. One data channel is offset for clarity. The figure shows a dropout of laser power from the mode-locking mode followed by a dropin to CW mode. The two laser beams are commonly very well correlated in mode-locking mode. In CW mode, the two beams show strong correlation and sometimes anti-correlation.

3.3 Principles of the CPM Laser

The topology of the CPM laser is shown in Fig. 3.8(a), which includes all the essential components: the gain, the absorber, linear loss, mirrors and the prism sequence. The distance between the absorber and the gain is about one quarter of the round-trip cavity length. The two pulses in the CPM laser are synchronized by their collision in the absorber, as shown in the snap shot in Fig. 3.8(b). The CPM laser enhances the laser beam's ability to saturate absorber by colliding two counter propagating pulses in it. The standing wave formed by the colliding pulses lowers the saturation fluence of the absorber to 1/3 of that in two traveling pulses case [39]. When the CPM laser is running in stable mode-locking condition, only these two synchronized pulses can deplete the absorber and retain part of their energy. Noise bursts will be suppressed.

The nonlinear effects of the saturable gain and the saturable absorber lead to the passive mode-locking of the CPM laser. The starting pulse of the CPM laser emerges from random

(a)

(b)

G: Gain A: Absorber P: Prisms
L: Lens O: Output Coupler
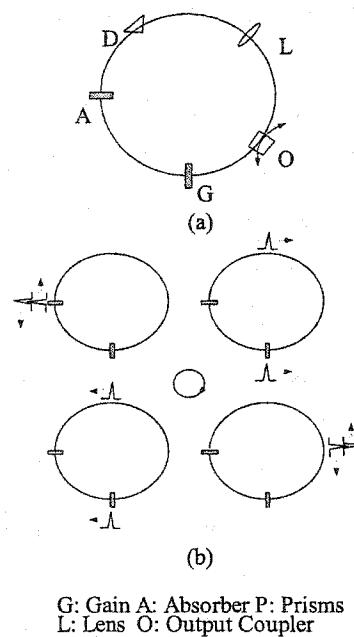
Figure 3.8: The topology and synchronization of two pulses in the CPM laser.

noise. When a noise pulse is able to bleach the absorber, it starts growing in the cavity. The pulse keeps growing until it saturates the gain. The gain and the absorber are slow in that their fluorescence energy (or longitudinal) relaxation times are much longer than the duration of ultrashort pulses produced in the system. Therefore, when the absorber is bleached by the leading edge, it stays transparent to the rest part of the pulse. This effect shortens the pulse duration by clipping the leading edge of the pulse. On the other hand, the gain only amplifies the leading edge of the pulse due to its depletion. The rest of the pulse sees only loss. So, while the pulse fluence grows, its duration contracts as well due to the shaping effects of the slow gain and absorber. The intracavity dispersion also plays an important role in the CPM laser.

The characteristics of the gain, absorber, and intracavity dispersion will be discussed in this section as well as the their ultrashort pulse generation mechanisms.

3.3.1 Modeling of the Absorber and the Gain

The saturable absorber plays an important role in the CPM laser. Its saturation effect discriminates against the noise pulses with lower energies. This effect can be described using rate equations. We first consider the absorbing transition in a 2-level system with CW input. The two energy states are homogeneously broadened in the absorber dye. Therefore, by considering the combined effects of absorption, stimulated emission, and spontaneous decay, the population on the upper state, N_2, can be written as

$$\frac{dN_2}{dt} = -W(N_2 - N_1) - \frac{N_2}{\tau_a}, \qquad (3.1)$$

where N_1 is the population in the lower level, and τ_a is the relaxation time of upper level. W is the stimulated emission or absorption rate, which is proportional to the photon flux, $F = I/h\nu$, where ν is the resonance frequency of the 2-level system. By introducing the absorption cross-section of the transition, W can be expressed as,

$$W = \frac{\sigma_a I}{h\nu}, \qquad (3.2)$$

By defining two new variables, $N_t = N_1 + N_2$ and $\Delta N = N_1 - N_2$, note that $\frac{dN_t}{dt} = 0$, we can rewrite Eq. 3.1 as

$$\frac{d\Delta N}{dt} = -\Delta N \left(\frac{1}{\tau_a} + 2W\right) + \frac{N_t}{\tau_a}. \qquad (3.3)$$

When the system reaches the steady state, the left hand side of Eq. 3.4 equals to zero, we obtain

$$\Delta N = \frac{N_t}{1 + 2W\tau_a}. \tag{3.4}$$

When the incident power has an intensity the same as the saturation intensity, $\Delta N = N_t/2$. When the incident power is well above saturation level, i.e. $2W\tau_a \gg 1$, $\Delta N \approx 0$. In a material, the power per unit volume, dP/dV, needed to maintain ΔN is,

$$\frac{dP}{dV} = h\nu W \Delta N = h\nu \frac{N_t W}{1 + 2W\tau_a}. \tag{3.5}$$

The population difference is related to the intensity of the incident laser beams as,

$$\frac{\Delta N}{N_t} = \frac{1}{1 + I/I_{a,s}}, \tag{3.6}$$

where

$$I_{a,s} = \frac{h\nu}{2\sigma_a \tau_a} \tag{3.7}$$

is known as the saturation intensity whose value relies on the material and the frequency of incident wave.

We next consider the case where the incident radiation is a train of ultrashort pulses. In the CPM laser, the DODCI absorber has a relaxation time about 1.2 ns [46] which is much longer than the typical duration of ultrashort pulses. In this case, the spontaneous decay of the upper level is trivial. Therefore, Eq. 3.3 can be reduced to

$$\frac{d\Delta N}{dt} = -2W\Delta N = -I(t)\Delta N \frac{2\sigma_a}{h\nu}. \tag{3.8}$$

Integrating Eq. 3.8 with the initial condition that $\Delta N(0) = N_t$ gives

$$\Delta N = exp\left[-\frac{2\sigma_a}{h\nu}\int_0^t I(t)dt\right]. \tag{3.9}$$

Similar to Eq. 3.7, by defining the energy fluence of the pulse(starting at t=0)

$$\Phi(t) = \int_0^t I(t)dt \tag{3.10}$$

we can define a saturation fluence, $\Phi_{a,s}$, as

$$\Phi_{a,s} = \frac{h\nu}{2\sigma_a}. \tag{3.11}$$

Then, the population difference varies with time as

$$\Delta N(t) = N_t exp[-\Phi(t)/\Phi_{a,s}]. \tag{3.12}$$

In this case, the fluence of the incident pulse determines the saturation behavior of the absorber. When the total fluence of the pulse is equals to Φ_s, the population difference drops to $\Delta N = N_t/e$ after the traversing of the pulse. The coefficient of loss caused by the absorber then can be written as

$$a(t) = a_0^s exp[-\Phi(t)/\Phi_{a,s}], \tag{3.13}$$

where a_0^s is the small signal loss of the absorber.

In the CPM laser, the gain is also saturable. The relaxation time of Rhodamine 6G in the gain is ~ 4 ns [46] which is also much longer than the a typical pulse's duration. It is easy to carry out similar calculation on the gain to find following results:

$$\Phi_{g,s} = \frac{h\nu}{\sigma_g} \tag{3.14}$$

and

$$g(t) = g_0^s exp[-\Phi(t)/\Phi_{g,s}]. \tag{3.15}$$

In a stable running mode, the pulses in the CPM laser saturates both the gain and the absorber. As a result, the shaping effect of the gain and the absorber mainly happens on the leading edge of the pulse.

In dye lasers, the two levels in above calculation need to be substituted by their corresponding line shape functions. A rigorous treatment of this problem can be found in Andrews and Tracy's work [47] where it is studied using the Maxwell-Bloch equations.

3.3.2 Rate Equation Model

The master equation of the CPM laser is first deduced by Haus using rate equations [24]. In a series of papers [24, 46, 48, 49], Haus discussed the formulation of the master equation and the parameter range of steady operating CPM lasers. The rate equation model is derived on following assumptions and approximations,

(1) The laser medium is homogeneously broadened.

(2) A pulse passing through any components in the cavity suffers only slight change on a single pass, i.e. the gain or loss in each round trip is much smaller than one.

(3) The gain and loss coefficients, as functions of fluence, may be expanded to second order.

(4) The dispersion of the laser system, as a function of frequency, may also be expanded to the second order.

The expansion of condition (3) and (4) is a reasonable on the assumption of condition (2). And the approximation in condition (4) is justified in our system as shown in Fig. 3.5

where the pulses' spectrum is much narrower than the available spectral range.

Under these conditions, the formula of pulse evolution in the cavity can be laid out by summing up the influence of each component in the cavity in a single round trip. The procedure to construct a master equation for an ultrafast laser is shown in Appendix B. Assuming the laser is running steadily, the following master equation can be derived

$$\left[g(t) - l - a(t) + \frac{1}{\omega_c^2} \frac{d^2}{dt^2} - \frac{1}{t_r} \frac{d}{dt} \right] \rho(t) = 0. \tag{3.16}$$

where g(t), a(t), l, t_r, and $\rho(t)$ represent the gain, the nonlinear loss of the absorber, the cavity linear loss, the round trip time, and the pulse's profile respectively. The overall gain, $g(t) - l - a(t)$, also changes with frequency. The term containing the second derivative with respect to time describes the spectral filtering effect caused by the shape of the gain spectrum. The last term describes the peak shifting effect caused by the asymmetric shaping effects of the gain and the absorber. This term causes a displacement of the pulse profile in time.

It should be noted that the gain and loss coefficients cannot be replaced directly by the formula in Eq. 3.13, 3.15 before an important conclusion is drawn. For the laser to be self-starting, the small signal gain, g_0^s, must meet following condition,

$$g_0^s > l + a_0^s, \tag{3.17}$$

where a_0^s is the small signal loss. But for the laser to stay in a steady mode-locking state, the gain factor, g_0, in each round trip before the pulse's arriving must be smaller than g_0^s, i.e. the population inversion of the gain must not fully recover. Furthermore, since any

noise preceding the pulse must see net loss to ensure pulse stability, it can also be derived that,

$$g_0^s > l + a_0^s > g_0. \tag{3.18}$$

Note that the loss may fully relax, i.e. $a_0^s = a_0$, since its fluorescence lifetime τ_a (~ 1.4 ns) is much smaller than t_r (~ 10.5 ns).

Now, we are ready to substitute Eq. 3.13 and Eq. 3.15 into Eq. 3.16,

$$\left[g_0 exp \left(\int_0^t dt |\rho|^2 / \Phi_{g,s} \right) - a_0 exp \left(\int_0^t dt |\rho|^2 / \Phi_{a,s} \right) - l + \frac{1}{\omega_c^2} \frac{d^2}{dt^2} - \frac{1}{t_r} \frac{d}{dt} \right] \rho(t) = 0, \tag{3.19}$$

Since each of these two coefficients includes the integral of the square of the pulse profile, the new master equation, Eq. 3.19 is a nonlinear integro-differential equation which has no analytic solution in general.

Here, we used the relation of $I = |\rho|^2$. By expanding the exponential terms in the gain and the loss coefficients and breaking them off with second-order terms, a simple analytic solution exists. Consider one of these expansions,

$$g_0 exp \left(\int_0^t dt |\rho|^2 / \Phi_{g,s} \right) \doteq g_0 \left[1 - \left(\int_0^t dt |\rho|^2 / \Phi_{g,s} \right) + \frac{1}{2} \left(\int_0^t dt |\rho|^2 / \Phi_{g,s} \right)^2 \right]. \tag{3.20}$$

The solution to Eq. 3.19 then has a soliton profile,

$$\rho(t) = A_0 sech(t/t_p), \tag{3.21}$$

with the following constraints,

$$\frac{1}{\omega_c^2 t_p^2} + g_0 \left[1 - \frac{A_0^2 \tau}{\Phi_{g,s}} + \left(\frac{A_0^2 \tau}{\Phi_{g,s}} \right)^2 \right] - l - a_0 \left[1 - \frac{A_0^2 \tau}{\Phi_{a,s}} + \left(\frac{A_0^2 \tau}{\Phi_{a,s}} \right)^2 \right] = 0, \tag{3.22}$$

$$\frac{\delta t}{t_p} = g_0 \left[\frac{A_0^2 \tau}{\Phi_{g,s}} - \left(\frac{A_0^2 \tau}{\Phi_{g,s}} \right)^2 \right] - a_0 \left[\frac{A_0^2 \tau}{\Phi_{a,s}} - \left(\frac{A_0^2 \tau}{\Phi_{a,s}} \right)^2 \right], \tag{3.23}$$

and

$$\frac{1}{t_p} = \frac{\omega_c^2 A_0^2}{4} \left(\frac{a_0}{\Phi_{a,s}} - \frac{g_0}{\Phi_{g,s}} \right). \tag{3.24}$$

These equations have important implications. Consider Eq. 3.24 where the inverse pulsewidth is related to the steady state gain and loss factors, since the pulsewidth has to be positive,

$$a_0/\Phi_{a,s} > g_0/\Phi_{g,s}. \tag{3.25}$$

The saturation fluence of the absorber must be less than that of the gain. This condition is first described by New [23] as

$$S = \Phi_{g,s}/\Phi_{a,s} > S_{min}. \tag{3.26}$$

S_{min} is a constant that varies in different ultrafast lasers, but it is always greater than unity. Substituting Eq. 3.26 into Eq. 3.22, one can get the same conclusion shown in Eq. 3.18.

Eq. 3.26 is instructive in the CPM laser's design. In order to make the saturation effect stronger in the absorber, the CPM laser employs a tighter focus on the absorber than that on the gain. The colliding pulse scheme also enhances local intensity and therefore the saturation in the absorber. In the CPM laser when two pulses collide, they form standing waves in the absorber and the total fluence is doubled. But the population required to be saturated in the absorber is small comparing to that in two traveling waves case since the molecules near the nodes of the standing wave need not be saturated. The noise bursts, therefore, suffer more loss. The overall colliding effect greatly improves the stability of CPM laser. One may intuitively conjecture that increasing the fluence of the two traveling waves

by tuning up pump power may have the same effect. But in that case, the gain relaxes faster which causes amplification of the spontaneous emission between pulses resulting in instability and satellite pulse generation (double pulsing) in the CPM laser.

New's stability requirement is essential to explain the pulse shortening effect, known as the gain-windowing effect, in the CPM laser, which is shown in Fig. 3.9. This gain-
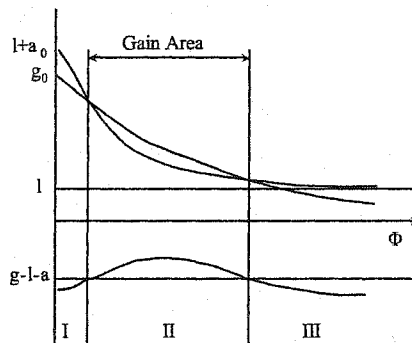
Figure 3.9: The interaction between the optical pulse and the dyes leads to window effect in the CPM laser (not in scale). The loss saturates faster than the gain while the pulse passing by, which opens a gain window (gain>1) for the main body of the pulse. The leading and trailing edges see only loss.

windowing effect shortens the pulses traveling in the cavity. But the shortening effect will not cause a pulse to shrink to a delta function with infinite small width due to intracavity dispersion and gain bandwidth limit.

In summary, the rate equation model successfully shows that the CPM laser is able to produce ultrashort pulses and remain stable against noise.

3.3.3 Dispersion Control

The rate equation model is successful in explaining pulse shortening effect of the CPM laser. But when the pulses produced are about 100 fs, the model is no longer valid without the incorporation of dispersion. The dispersive phase function in the CPM laser causes chirping

on the pulses and prohibits it from producing extremely short pulses with pulse width much less than 100 fs.

As we discussed in Section 2.1.2 and Section 2.3.2, only the second and high order dispersions play important roles in pulse generation. In the CPM laser, the dispersion mainly comes from the prism sequence, the gain, and the absorber. The prism sequence introduces variable, and normally negative, second order dispersion, i.e. negative GVD. The Kerr effect of the dye solvent and the interaction of the pulse with the gain and the absorber introduce dispersion by the SPM effect. The Kerr effect mainly happens in the EG streams at the two tight foci on the gain and the absorber since it strongly relies on the radiation intensity as shown in Eq. 2.46, which also indicates the Kerr effect is strongest in the middle part of the pulse. In the CPM laser, the Kerr effect is very small [39, page 47] [34]. But when the intracavity GVD is around zero, it is not negligible.

The CPM laser can normally operate with a small amount of negative GVD present in the cavity. But the CPM laser produces pulses with the shortest duration when its intracavity GVD is around zero [34], i.e. when the GVD caused by SPM and negative GVD introduced by the prisms are well balanced in the cavity. This condition suggests that the CPM laser can be treated as a soliton laser if the dispersion is averaged by its round trip time. In other words, the dispersion of the CPM laser can be treated as uniform from one round trip to the next. Recognizing this soliton-like shaping mechanism, Valdmanis *et al.* produced the shortest pulse ever in the CPM laser in 1985. The pulses produced have a transform-limited shape.

To incorporate dispersion, the pulse profile ρ must be replaced by $\psi(t) = \rho e^{(i\phi)}$, where ϕ is the chirp. The master equation must also be modified to include the dispersion terms.

Here, we consider a master equation only including the second order dispersion effects. The GVD in the cavity is expressed as $iD \equiv ik''\Delta\omega^2 L_d$ where L_d is the path length and k'' is the GVD parameter. In the CPM laser, D has the physical meaning of total intracavity GVD. In the time domain, the GVD term is transformed into $iD\frac{d^2}{dt^2}$ by the Fourier transformation. The Kerr effect can be expressed as $-i\delta|\rho^2|$, where δ is a constant. From each round trip to the next, there also exists envelope-to-carrier phase shift, i.e. $\Delta\phi = \phi_{n+1} - \phi_n < 2\pi$. This effect is significant for extremely short pulses containing only a few cycles of oscillation. We will temporarily neglect this effect in the master equation. These phase effects introduce only imaginary terms into the master equation. After including various dispersion terms the master equation takes the form of Landau-Ginzburg equation whose behavior is out of the scope of this thesis and shall not be discussed here.

Higher order dispersion (>2) can also be incorporated into the rate equation model. These higher order dispersion effects are only important when the intracavity GVD is near zero. This condition further complicates the situation in the CPM laser in two ways. First, when the GVD is near zero, the CPM laser produces very short pulses. Subsequently, the very broad spectrum of the pulses may extend to the positive GVD regime and cause the pulse to break apart. Second, the very broad spectrum covers a large part of the gain emission spectrum so that the gain-shape term must include higher order terms.

Experimentally, the effects caused by the TOD can only be eliminated by removing the TOD generating material in the cavity. In our CPM laser, we have not removed the TOD. Therefore in the vicinity of zero GVD, our CPM laser is not stable.

The TOD can be written in analogy to the second dispersion term as $ik'''\Delta\omega^3 L_d$ [50].

Including the GVD and TOD in group velocity expression, one has,

$$v_g = v_{g,0} + \frac{dv_g}{d\omega}\bigg|_{\omega=\omega_0} (\omega - \omega_0) + \frac{1}{2}\frac{d^2v_g}{d\omega^2}\bigg|_{\omega=\omega_0} (\omega - \omega_0)^2. \tag{3.27}$$

Considering GVD is much smaller (one order) than the TOD and omitting higher order terms, one obtains [51]

$$v_g = v_{g,0} - \frac{k_0^{''}}{k_0^{'2}}(\omega - \omega_0) - \frac{1}{2}\frac{k_0^{'''}}{k_0^{'2}}(\omega - \omega_0)^2. \tag{3.28}$$

Eq. 3.28 shows that there are two frequencies that have the same group velocity in the cavity. This fact causes the spectrum of the pulses produced to have multi-humps or break apart, which were experimentally observed [52, 51] and theoretically studied [50].

In current state-of-art ultrafast systems, GVD and the TOD free operation has been achieved. The FOD and Kerr effect limit the generation of extremely short pulses in these systems.

Chapter 4

Bistable Medium Model

The existing theoretical models successfully reveal many aspects of the ultrashort pulse generation mechanism in the CPM laser. But there still exist problems that have never been addressed, such as the various pulse shapes and transient behaviors in the CPM laser [53].

Almost all models for ultrafast lasers have soliton solutions, e.g. in the rate equation model. But the soliton is only one of the pulse shapes observed in the CPM laser. Gaussian-shaped pulses were also observed [53]. The rate equation model must include higher order nonlinear terms to account for Gaussian pulse. But this improvement is countered by a loss of generality.

The nonlinear dynamics of the CPM laser have hardly been addressed in the references due to its very fast nature and complexity. Recently, Andrews and Tracy investigated these phenomena and proposed a novel bistable-system mapping model. In an ultrafast laser, the mapping of the pulse transfer function bifurcates between the steady state to other possible states. This bistable property is essential in explaining the complicated dynamics of the CPM laser. Andrews and Tracy developed a highly degenerate bifurcation scenario. In their model, a composite map is developed to describe the transfer function of a pulse

traversing the CPM laser in each round trip. The composite transfer (mapping) function is based on Maxwell-Bloch equations. The model also accounts for the memory effect of the gain, which does not fully recover between its interactions with pulses. Their study suggests that the nonlinear dynamics of the CPM laser is possible only when the memory effect lasts a few round-trip times and predicts that the dropout and dropin behaviors of the CPM laser must be different.

In this chapter, we propose a bistable medium model for ultrafast lasers using a fluence mapping method. In this model, the CPM laser is treated as a bistable medium that can respond to input pulses. The output is fed back to the medium after each round trip time. In this way, the system can be described as a transfer function of the pulse fluence. The fluence mapping derived from this transfer function must have stable fixed points at origin and steady state to allow for pulse generation.

For soliton-shaped pulses, a simple close-form solution of the transfer function exists. By using numerical methods and employing different pulse shapes in our model, we are able to explore the characteristics of their corresponding transfer functions. This model can be easily modified to include higher dispersions and the Kerr effect. This model also has universal generality with the potential to model other ultrafast lasers and explore the pulse evolution dynamics.

In this chapter, we will start with a description of the stable-state master equation. In Section 4.2, the master equation is solved in two special cases for pulses with three different shapes. In Section 4.3, we obtain a solution for soliton pulses in a general case. In the last section, the results we obtained using numerical methods are discussed.

4.1 Stable State Master Equation

Under the SVEA, the description of an optical pulse can be separated into two parts, the slowly varying profile and the fast carrier oscillation (see Section 2.1.3). Leaving out the carrier frequency part, the pulse can be simply described as,

$$\psi(t) = \rho(t)e^{i\phi(t)}, \tag{4.1}$$

where $\rho(t)$ and $\phi(t)$ are real functions of t representing the profile and the phase of the pulse respectively.

The evolution of the pulse in each round trip time can then be described by,

$$\psi^{(n+1)}(t) = \left\{ 1 + F'\left[\Phi^{(n)}(t) \right] \right\} \psi^{(n)}(t) + \tilde{\epsilon}\ddot{\psi}^{(n)}(t) + O(\dddot{\psi}^{(n)}(t)). \tag{4.2}$$

here, the pulse's profiles before and after one round trip in the cavity are denoted by n and $n+1$. $1 + F'[\Phi(t)]$ is the transfer function, whose argument is the fluence of the pulse,

$$\Phi(t) = \int_{-\infty}^{t} dt' \left| \psi(t') \right|^2 = \int_{-\infty}^{t} dt' \left| \rho(t') \right|^2. \tag{4.3}$$

$F'[\Phi(t)]$ is a real function describing the gain windowing effect caused by the saturable gain and the slow saturable absorber. $\ddot{\psi}(t) = d^2\psi(t)/dt^2$ is the second order derivative of $\psi(t)$. $\tilde{\epsilon}$ is a small complex number with units of time squared. The real and imaginary parts of this term account for the spectral shape of the gain and the sum of GVD in a round-trip, respectively. $O(\dddot{\psi}(t))$ implies that the terms describing higher order derivatives of $\psi(t)$ are small and will be omitted in following calculation.

When the change happening in each round-trip is small, Eq. 4.2 is justified with F' and $\tilde{\epsilon}$ being small. The term containing first order derivative of $\psi(t)$ does not show up in Eq. 4.2 since its real part is lumped into F', and its imaginary part can be set to zero by choosing the correct reference of time and the carrier frequency. By explicitly evaluating the derivatives as

$$\dot{\psi} = \frac{d}{dt}\left(\rho e^{i\phi}\right) = \left(\dot{\rho} + i\dot{\phi}\rho\right)e^{i\phi} \tag{4.4}$$

and

$$\ddot{\psi} = \frac{d^2}{dt^2}\left(\rho e^{i\phi}\right) = \left[\left(\ddot{\rho} - \rho\dot{\phi}^2\right) + i\left(2\dot{\phi}\dot{\rho} + \ddot{\phi}\rho\right)\right]e^{i\phi}, \tag{4.5}$$

we can rewrite the mapping equation in terms of $\rho(t)$ and $\phi(t)$. Hereafter, the functions of $\psi(t)$, $\rho(t)$ and $\phi(t)$ will be written as ψ, ρ and ϕ for simplicity.

When the system is in steady state, the master equation governing the pulse behavior can be constructed. Assuming the pulse replicates itself after each round-trip,

$$\rho^{(n+1)} = \rho^{(n)}, \tag{4.6}$$

and

$$\phi^{(n+1)} = \phi^{(n)} + \Delta\phi. \tag{4.7}$$

Here, $\Delta\phi$ stands for a possible phase shift relative to the carrier oscillation of the pulse's envelope in each round-trip time. Eq. 4.2 can then be simplified to:

$$\rho e^{i\Delta\phi} = \left\{1 + F'\left[\Phi(t)\right]\right\}\rho + \tilde{\epsilon}\left[\left(\ddot{\rho} - \rho\dot{\phi}^2\right) + i\left(2\dot{\phi}\dot{\rho} + \ddot{\phi}\rho\right)\right]. \tag{4.8}$$

$\tilde{\epsilon}$ can be rewritten as

$$\tilde{\epsilon} = \epsilon cos(\phi_\epsilon) + i\epsilon sin(\phi_\epsilon), \tag{4.9}$$

where ϵ and ϕ_ϵ are real constants with ϵ always being positive. As shown in Appendix B, $Re(\tilde{\epsilon}) > 0$ describes a gain spectrum peaked at the carrier frequency, therefore, $\phi_\epsilon \in [-\pi/2, \pi/2)$. When ϕ_ϵ is chosen to be 0 or $-\pi/2$, ϵ has either real or imaginary value only. The two values of ϕ correspond to the cases of either only the dispersion ($\phi_\epsilon = -\pi/2$) or only the spectral limitation of the gain ($\phi_\epsilon = 0$). Consequently, $\phi_\epsilon < 0$ corresponds to the case of negative GVD.

Substituting Eq. 4.9 into Eq. 4.8, Eq. 4.8 can be separated into real and imaginary parts:

$$\rho sin(\phi_\epsilon - \Delta\phi) = \left\{1 + F'\left[\Phi(t)\right]\right\}\rho sin(\phi_\epsilon) - \epsilon\left(2\dot{\phi}\dot{\rho} + \ddot{\phi}\rho\right), \qquad (4.10)$$

and

$$\rho cos(\phi_\epsilon - \Delta\phi) = \left\{1 + F'\left[\Phi(t)\right]\right\}\rho cos(\phi_\epsilon) - \epsilon\left(\ddot{\rho} - \dot{\phi}^2\rho\right). \qquad (4.11)$$

These two coupled second order differential equations with an arbitrary transfer function are difficult to solve. In addition, the transfer function contains an integral of pulse power over time, so that the equations are actually third-order differential equations.

So far, the pulse profile function has been considered only in terms of time. As shown in Haus's work [24], the soliton pulse has a simple parabola shape after transforming the argument from time, t, to fluence, Φ. Therefore, the equations may be easier to solve by transforming the argument. Since no additional restriction is involved in the transformation, a pulse's description by fluence will be equivalent to the time description.

The fluence relies only on the shape of the pulse, ρ, but not the relative phase function ϕ. So it is intuitive to simplify the equations by eliminating ϕ. We also introduce a function, P, where,

$$P[\Phi(t)] \equiv \rho^2. \qquad (4.12)$$

Notice two useful expressions,

$$\dot{\Phi} = \rho^2 = P, \quad \frac{d}{dt}\left(\rho^2 \dot{\phi}\right) = \left(2\rho\dot{\rho}\dot{\phi} + \rho^2\ddot{\phi}\right).$$ (4.13)

By assuming that there exists $F(\Phi)$ that

$$F'(\Phi) = \frac{dF(\Phi)}{d\Phi}.$$ (4.14)

and substituting Eq. 4.13 and Eq. 4.14 into Eq. 4.10, Eq. 4.10 becomes

$$sin(\phi_\epsilon - \Delta\phi)\frac{d\Phi}{dt} = sin(\phi_\epsilon)\frac{dF}{d\Phi}\frac{d\Phi}{dt} + sin(\phi_\epsilon)\frac{d\Phi}{dt} - \epsilon\frac{d(\dot{\Phi}\dot{\phi})}{dt}.$$ (4.15)

At time $t = -\infty$, the following boundary conditions for Φ and $F(\Phi)$ exist:

$$(\Phi)_{-\infty} = (\dot{\Phi})_{-\infty} = 0, \quad (F(\Phi))_{-\infty} = const..$$ (4.16)

Eq. 4.15 can then be integrated in time which gives the formula of $\dot{\phi}$

$$\dot{\phi} = \frac{F sin(\phi_\epsilon) + \Phi sin(\phi_\epsilon) - \Phi sin(\phi_\epsilon - \Delta\phi)}{\epsilon P}.$$ (4.17)

Considering P, its derivatives with respect to time are,

$$\dot{P} = 2\rho\dot{\rho},$$ (4.18)

and

$$\ddot{P} = 2\dot{\rho}^2 + 2\rho\ddot{\rho}.$$ (4.19)

The $\ddot{p}$ can be solved from Eq. 4.11. By substituting Eq. 4.11 into Eq. 4.19 and eliminating $\dot{\phi}$ using Eq. 4.17, Eq. 4.19 becomes,

$$\epsilon^2 \ddot{P} P/2 - \epsilon^2 \dot{P}^2/4 - \epsilon P^2 cos(\phi_\epsilon - \Delta\phi) + \epsilon P^2 (F' + 1)cos(\phi_\epsilon)$$
$$= [F sin(\phi_\epsilon) + \Phi sin(\phi_\epsilon) - \Phi sin(\phi_\epsilon - \Delta\phi)]^2 . \qquad (4.20)$$

We are now ready to transform the t's into the implicit variable Φ in Eq. 4.20 by changing $\dot{P} = \frac{dP}{dt}$ to $P' = \frac{dP}{d\Phi}$ and $\ddot{P} = \frac{d^2 P}{dt^2}$ to $P'' = \frac{d^2 P}{d\Phi^2}$. Notice that

$$\dot{P} = \frac{dP}{d\Phi}\frac{d\Phi}{dt} = \frac{dP}{d\Phi}\dot{\Phi} = P'P, \qquad (4.21)$$

and

$$\ddot{P} = \frac{d(P'P)}{d\Phi}\dot{\Phi} = P^2 P'' + P P'^2 . \qquad (4.22)$$

Eq. 4.20 then turns into

$$\left[\epsilon^2 P'' P/2 + \epsilon^2 P'^2/4 - \epsilon cos(\phi_\epsilon - \Delta\phi) + \epsilon(F' + 1)cos(\phi_\epsilon)\right] P^2$$
$$= [F sin(\phi_\epsilon) + \Phi sin(\phi_\epsilon) - \Phi sin(\phi_\epsilon - \Delta\phi)]^2 . \qquad (4.23)$$

The master equation, Eq. 4.23, now is much simplified.

4.2 Solving the Master Equation

We take a different approach from others to solve Eq. 4.23. Instead of finding a transfer function first, we assume that the pulse shape is given. Then, by putting in various commonly used pulse shapes, the corresponding transfer functions required can be extracted.

The descriptions of three commonly used pulse profiles using time t or fluence Φ as argument is shown in Table 4.1 and Fig. 4.1. The maximum fluence of pulses, Φ_m, is

Pulse	Gaussian	Soliton	Lorenzian
$P(A,\tau,t)$	$A\exp\left(-t^2/\tau^2\right)$	$A\,sech^2\left(t/\tau\right)$	$\frac{A}{1+t^2/\tau^2}$
Φ_m	$A\tau\sqrt{\pi}$	$2A\tau$	$A\tau\pi$
$P(\Phi_m,\tau,t)$	$\frac{\Phi_m}{\sqrt{\pi}\tau}\exp\left(-t^2/\tau^2\right)$	$\frac{\Phi_m}{2\tau}sech^2\left(t/\tau\right)$	$\frac{\Phi_m}{\tau\pi}\frac{1}{1+t^2/\tau^2}$
$\Phi(\Phi_m,\tau,t)$	$\frac{\Phi_m}{2}\left[erf\left(t/\tau\right)+1\right]$	$\frac{\Phi_m}{1+exp(-2t/\tau)}$	$\frac{\Phi_m}{\pi}\left[atan\left(t/\tau\right)+\pi/2\right]$
$t(\Phi_m,\tau,\Phi)$	$aerf\left(2\Phi/\Phi_m-1\right)\tau$	$\frac{1}{2}ln\left(\frac{\Phi}{\Phi_m-\Phi}\right)\tau$	$-ctan\left(\pi\Phi/\Phi_m\right)\tau$
$P(\Phi_m,\tau,\Phi)$	$\frac{\Phi_m}{\sqrt{\pi}\tau}\exp\left[-aerf^2\left(\frac{2\Phi}{\Phi_m}-1\right)\right]$	$\frac{2\Phi_m}{\tau}\left[\frac{\Phi}{\Phi_m}-\left(\frac{\Phi}{\Phi_m}\right)^2\right]$	$\frac{\Phi_m}{\tau\pi}sin^2\left(\frac{\pi\Phi}{\Phi_m}\right)$

Table 4.1: Profiles of conventionally used pulses as functions of time and fluence, Φ.

introduced in Table 4.1 to substitute for the amplitude, A. Fig. 4.1 shows that the portion of fluence in the pedestals of the three kinds of pulses are different: the Gaussian pulse has the shortest wings, and the Lorentzian pulse has the largest wings among the three pulse shapes. For a pulse with any of the three shapes, most of the fluence is located in the main body of the pulse, which causes the rapid change of fluence in Fig. 4.1 (c) and (d) around its peak.

Though the fluence in a pulse's wings is small, it may cause serious difficulty in theoretical treatment. The substitution of t with fluence can reduce this kind of difficulty. The comparison of pulse profiles plotted in time and in fluence is shown in Fig. 4.2. The pulses plotted have the same fluence and duration, and they will be used in the calculation in following sections.

The error function $erf(x)$ in Table 4.1 is defined as

$$erf(t) = \frac{2}{\sqrt{\pi}}\int_{-\infty}^{t} exp(-x^2)dx, \tag{4.24}$$

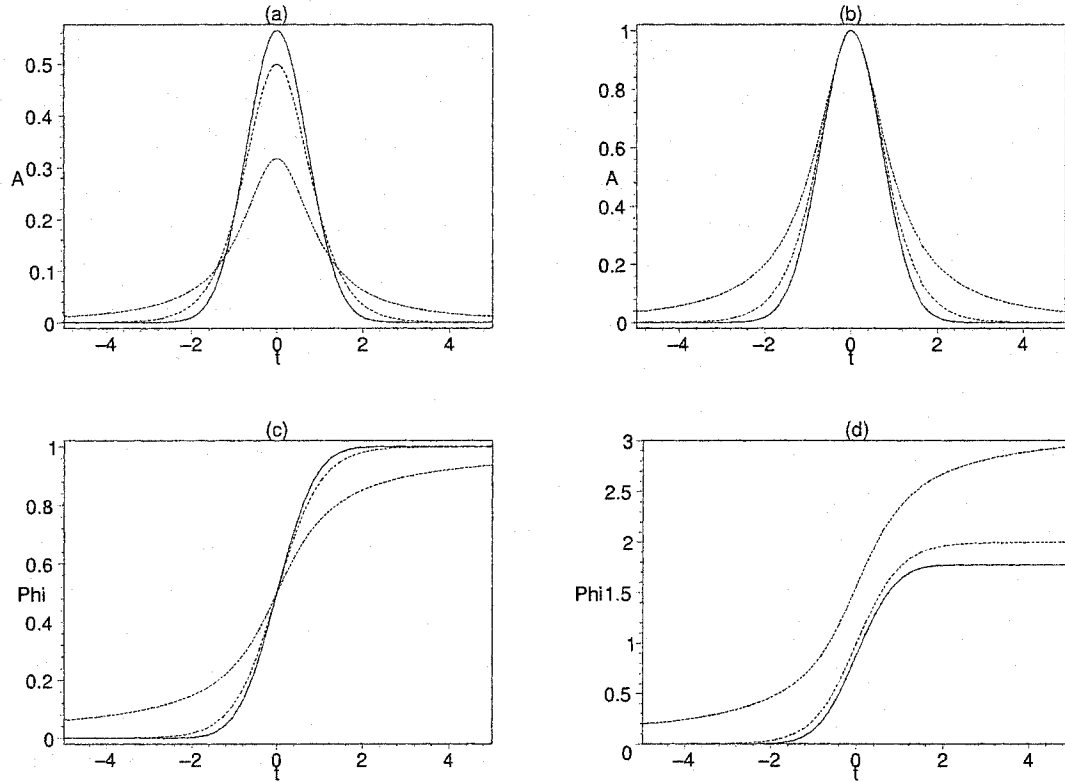with $aerf(y)$ being its inverse function.

Figure 4.1: The profiles and fluences are plotted as function of time for three kinds of commonly used pulses: Gaussian(solid line), Soliton(dotted line), and Lorentzian(dashed line). The pulses in (a) and (c) have unity fluence, in (b) and (d) have unity peak amplitude.

We set out to solve Eq. 4.23 and Eq. 4.20 in the two special cases that $\phi_\epsilon = -\pi/2$ or 0 first. Then, the general case that $\phi_\epsilon \in (-\pi/2, \pi/2)$ is considered.

Case I ($\phi_\epsilon = -\pi/2$):

In this case, only the second order dispersion of the pulse exists. Eq. 4.20 and 4.23 reduce to

$$\frac{\ddot{P}P/2 - \dot{P}^2/4}{P^2} + \frac{sin(\Delta\phi)}{\epsilon} = \frac{[F + \Phi - \Phi cos(\Delta\phi)]^2}{\epsilon^2 P^2} \qquad (4.25)$$

and

$$P''P/2 + P'^2/4 + \frac{sin(\Delta\phi)}{\epsilon} = \frac{[F + \Phi - \Phi cos(\Delta\phi)]^2}{\epsilon^2 P^2}. \qquad (4.26)$$
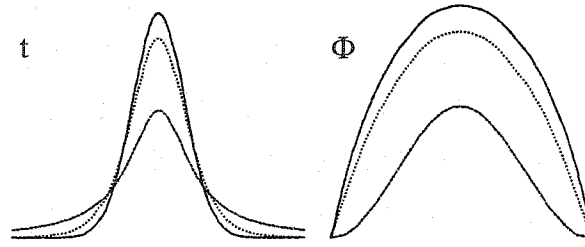
Figure 4.2: The profiles of the three commonly used pulses are plotted as functions of time and fluence. Gaussian(solid line), Soliton(dotted line), and Lorentzian(dashed line). The pulses plotted have the same fluence and duration.

The left hand side (LHS) of Eq. 4.25 is always greater or equal to 0. By substituting Eq. 4.18 and 4.19 into the LHS of Eq. 4.25, we have,

$$\frac{\ddot{\rho}}{\rho} \geq -\frac{sin(\Delta\phi)}{\epsilon}. \tag{4.27}$$

The minimum of the LHS of Eq. 4.27 is $-1/\tau^2$ at $t = 0$ (or $\Phi = \Phi_m/2$) for all three kinds of pulses. It will be proved later in this section that the inequality can be removed by the continuity requirement of F, i.e.

$$\epsilon/\tau^2 = sin(\Delta\phi). \tag{4.28}$$

The square roots of both sides of Eq. 4.26 give two opposite roots, of which both are possible branches of F. The two parts of the curve connect to each other at $\Phi = \Phi_m/2$ where both functions cross zero. The continuity requirement of F at this point limits $\Delta\phi$ to only one value as shown in Eq. 4.28. This relationship can also be deduced from Eq. 4.11 and 4.17. By substituting $\phi_\epsilon = -\pi/2$, Eq. 4.11 turns into

$$-\frac{sin(\Delta\phi)}{\epsilon} = \frac{\ddot{\rho}}{\rho} - \dot{\phi}^2, \tag{4.29}$$

which leads to Eq. 4.28 when $\Phi = \Phi_m/2$ and $\dot{\phi} = 0$. This equation also allows us to estimate the phase and chirp of the pulse. $\dot{\phi}$ is depicted in Fig. 4.3.
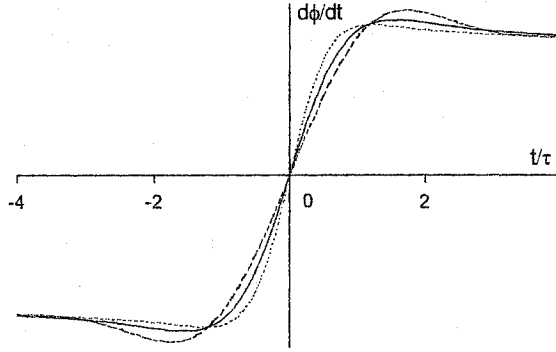

Figure 4.3: $\dot{\phi}$ shows symmetrical phase distribution of the three kinds of pulse about the peak when only second order dispersion presents in the model: Soliton (solid line), Gaussian (dashed line), and Lorentzian (dotted line).

In a stable solution, F' has to be negative on the leading and trailing edges and positive on the peak of a pulse to create a gain window. This constraint limits the solution to one function,

$$F = -\Phi + \Phi cos(\Delta\phi) + \begin{cases} -\epsilon P\sqrt{P''P/2 + P'^2/4 + sin(\Delta\phi)/\epsilon} & (\Phi \leq \Phi_m/2) \\ \epsilon P\sqrt{P''P/2 + P'^2/4 + sin(\Delta\phi)/\epsilon} & (\Phi > \Phi_m/2). \end{cases} \qquad (4.30)$$

The F functions and their derivatives with respect to Φ for the three types of pulses in Table 4.1 are plotted in Fig. 4.4. The plot of F shows the slow linear decreasing term in Eq. 4.30 which has a negative value at $\Phi = \Phi_m$. It implies that the loss coefficient shown on the low-fluence wings is greater than that of the gain around the peak. This nonlinear gain enables the pulse to retain its shape against dispersion. The total fluence of the pulse does not incline. Rather, the fluence gain caused by the transfer function, the integral of $\Phi F'$, is positive. The total fluence of the pulse is conserved. Fig. 4.4 (b) also shows F' to be

symmetric about the peak. F and F' for three kinds of pulse shape are similar, though the

F function exhibits one stable fixed point at zero and another fixed point around one. The

wings of the pulses cause the F functions to be significantly different between the beginning

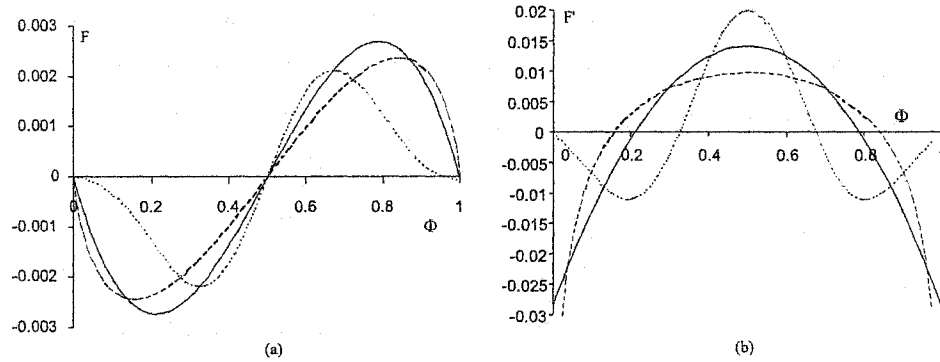and the end of the pulses. But in the main body part, they behave similarly.

Figure 4.4: The F and F' as functions of pulse fluence for three kinds of conventionally used pulses: Soliton (solid line), Gaussian (dashed line), and Lorentzian (dotted line). Each pulse has unity fluence, $\epsilon = 0.05$, and $\tau = 1$ in the calculation.

Case II ($\phi_\epsilon = 0$):

This case, ϵ corresponds to the case of gain spectral filtering only. ϵ is real, and $\epsilon > 0$.

When $\phi_\epsilon = 0$, the RHS of Eq. 4.23 has $\Phi_m sin(\Delta\phi) \rightarrow 0$ at the end of the pulse, therefore,

$\Delta\phi$ can only be zero. Eq. 4.23 then becomes

$$F' = -\epsilon(P''P/2 + P'^2/4). \tag{4.31}$$

Eq. 4.31 can be integrated analytically for a soliton pulse, and numerically for the other

two. The F's belonging to all three kinds of pulses can be obtained directly from Eq. 4.31.

It is also interesting to obtain the dispersion of the pulses using Eq. 4.8. The dispersion

is depicted in Fig. 4.5. The imaginary term on the RHS of Eq. 4.8 equals to zero, which

means $\rho^2\dot\phi = const.$, since

$$\frac{d\left(\rho^2\dot\phi\right)}{\rho dt} = 0,$$ (4.32)

and

$$\rho^2\dot\phi = const..$$ (4.33)

In contrast to the dispersion only case, the phase change around the peak is much smaller than that on the wings. In an ultrafast system, the ideal pulse produced is FTL. But in our model, a chirp-free system does not produce such pulses. In fact, the shortest pulse should have a square shape so that

$$\dot\phi = const..$$ (4.34)

Our model also shows that all three pulse shapes must have a chirp to be stable.
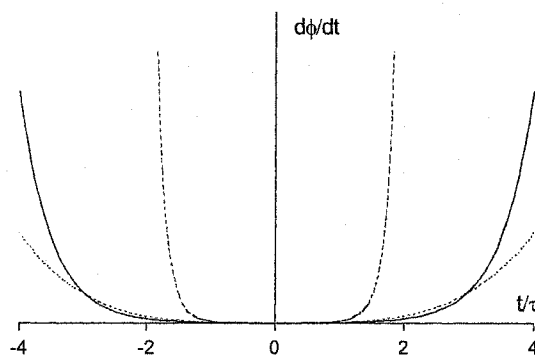
Figure 4.5: $\dot\phi$ shows asymmetric phase distribution of the three kinds of pulse about the peak when only gain spectral filtering exists in the model: Soliton (solid line), Gaussian (dashed line), and Lorentzian (dotted line).

The F and F' for the three kinds of pulse are plotted in Fig. 4.6. In this case, the gain filtering effect causes more loss than that in the dispersion only case. Though the F functions still have the bistable feature we expected, they are raised to compensate for the loss.

Figure 4.6: The F and F' as functions of fluence for the three kinds of pulse: Soliton (solid line), Gaussian (dashed line), and Lorentzian (dotted line). Each pulse has unity fluence, $\epsilon = 0.01$, and $\tau = 1$ in the calculation.

Case III ($\phi_\epsilon \in (-\pi/2, \pi/2)$):

In this case, the master equation remains a first order differential equation of F. Rewriting Eq. 4.23, we have

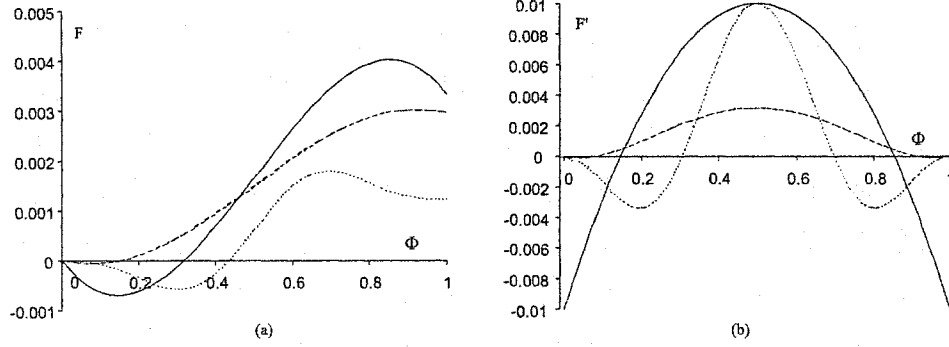$$F' = \frac{[F \sin(\phi_\epsilon) + \Phi \sin(\phi_\epsilon) - \Phi \sin(\phi_\epsilon - \Delta\phi)]^2}{\epsilon P^2 \cos(\phi_\epsilon)}$$
$$- \frac{\epsilon(P'' P/2 + P'^2/4) - \cos(\phi_\epsilon - \Delta\phi) + \cos(\phi_\epsilon)}{\cos(\phi_\epsilon)}, \tag{4.35}$$

with the boundary condition $F(0) = 0$ and $F'(0) < 0$. Noticing the $P(\Phi)$ functions for the three kinds of pulse all have similar shapes, so we can rescale them as

$$P(\Phi) = c \frac{\Phi_m}{\tau} p(x), \tag{4.36}$$

where $x \equiv \frac{\Phi}{\Phi_m}$, $x \in [0, 1]$; and c is a constant whose value can be found in Table 4.1. $p(x)$ is zero at $x = 0$ and 1 corresponding to the beginning and the end of a pulse.

By substituting Eq. 4.36 into Eq. 4.35, we have

$$F'(x) = \frac{[F(x) \sin(\phi_\epsilon)/\Phi_m + x \sin(\phi_\epsilon) - x \sin(\phi_\epsilon - \Delta\phi)]^2}{c^2 \alpha \cos(\phi_\epsilon) p^2(x)}$$
$$- \frac{c^2 \alpha \Phi_m^2 [p''(x)p(x)/2 + p'^2(x)/4] - \cos(\phi_\epsilon - \Delta\phi) + \cos(\phi_\epsilon)}{\cos(\phi_\epsilon)}, \tag{4.37}$$

with

$$\alpha = \epsilon/\tau^2. \tag{4.38}$$

We start solving this equation by conjecturing that the numerator of the first term in the RHS of Eq. 4.37 must have the factor $p(x)$ to make it converge on $x = 0$ and 1. Therefore $F(x)$ can be written as

$$F(x) = \frac{\Phi_m}{sin(\phi_\epsilon)} \left[-x sin(\phi_\epsilon) + x sin(\phi_\epsilon - \Delta\phi) + c\alpha p(x) r(x) \right], \qquad (4.39)$$

where r(x) is an arbitrary function of x. Now we need to solve the equation for $r(x)$ instead, which has the form

$$p(x)r'(x) + p'(x)r(x) = \frac{sin(\phi_\epsilon) - sin(\phi_\epsilon - \Delta\phi_\epsilon)}{c\alpha}$$
$$+ \frac{sin(\phi_\epsilon)\left\{ \Phi_m^2 \alpha r^2(x) - c^2 \Phi_m^2 \alpha \left[p''(x)p(x)/2 + p(x)'^2/4 \right] - cos(\phi_\epsilon - \Delta\phi) + cos(\phi_\epsilon) \right\}}{c\Phi_m \alpha cos(\phi_\epsilon)}. \qquad (4.40)$$

This equation has advantage over Eq. 4.37 by reducing the singularity by one order. A numerical calculation is then easier to carry out basing on Eq. 4.40. Eq. 4.35 and 4.39 provide two constraints for the calculation,

$$F'(x) + \frac{c^2\alpha\Phi_m^2 \left[p''(x)p(x)/2 + p'^2(x)/4 \right] - cos(\phi_\epsilon - \Delta\phi) + cos(\phi_\epsilon)}{sin(\phi_\epsilon)cos(\phi_\epsilon)} > 0, \qquad (4.41)$$

and,

$$F(x = 1) = \frac{\Phi_m}{sin(\phi_\epsilon)} \left[-sin(\phi_\epsilon) + sin(\phi_\epsilon - \Delta\phi) \right]. \qquad (4.42)$$

Now, $r(x)$ has 4 parameters, $\{\Delta\phi, \phi_\epsilon, \alpha, \Phi_m\}$. Eq. 4.42 can be solved numerically in general. But for a soliton pulse, it is possible to solve it analytically.

4.3   Soliton Pulse Solution

For a soliton pulse, a closed form solution exists for Eq. 4.42. We first assume $r(x)$ to have the form of $r(x) = a(x - x_0)$. The value of a and x_0 can be obtained from the boundary

conditions. Then, by substituting $r(x)$ into Eq. 4.40, the resulting function is quadratic polynomial of x which equals to zero everywhere. The solution can be found by solving the constraint equations,

$$F(x) = \frac{2a\alpha x(x - \frac{1}{2})(1 - x) + x sin(\phi_\epsilon - \Delta\phi) - x sin(\phi_\epsilon)}{sin(\phi_\epsilon)}, \qquad (4.43)$$

with

$$x_0 = 1/2, \qquad (4.44)$$

$$a = \frac{-3 + \sqrt{9 + 8tan^2(\phi_\epsilon)}}{tan(\phi_\epsilon)}, \qquad (4.45)$$

and

$$sin(\Delta\phi) = sin(\phi_\epsilon)\alpha - 2cos(\phi_\epsilon)a\alpha x_0 - sin(\phi_\epsilon)a^2\alpha x_0{}^2. \qquad (4.46)$$

Eq. 4.45 and 4.46 add two constraints to the choice of parameters for F. In the calculation, we also choose τ and Φ_m to be unity. Here, we chose ϕ_ϵ as the variable, i.e. $F(x, \phi_\epsilon)$, with $\phi_\epsilon \in (-\pi/2, 0)$ and $(0, \pi/2)$. This solution is consistent with our numerical calculation. It is easy to prove that in the two special cases, this solution reduces to the solutions discussed in the previous section. The parameters a and $\Delta\phi$ are plotted in Fig. 4.7. In an ultrafast laser, the sign of $\Delta\phi$ shows the delay or advance of the pulse relative to round trip time of the carrier frequency. The parameter $\Delta\phi$ describes the phase shift of a pulse's envelope to the carrier frequency. The $\Delta\phi$ depicted in Fig. 4.7(b) shows that this value is always small and may be positive or negative. The curve of $\Delta\phi$ shows that $F(x = 1)$ is always above 0.

The phase of the pulse can be found by substituting Eq. 4.43 into Eq. 4.17,

$$\frac{d\phi}{dt} = \frac{a}{2}coth^{-1}(t) \quad or \quad \frac{d\phi}{dx} = \frac{a}{2}\frac{x - \frac{1}{2}}{x(1 - x)}. \qquad (4.47)$$
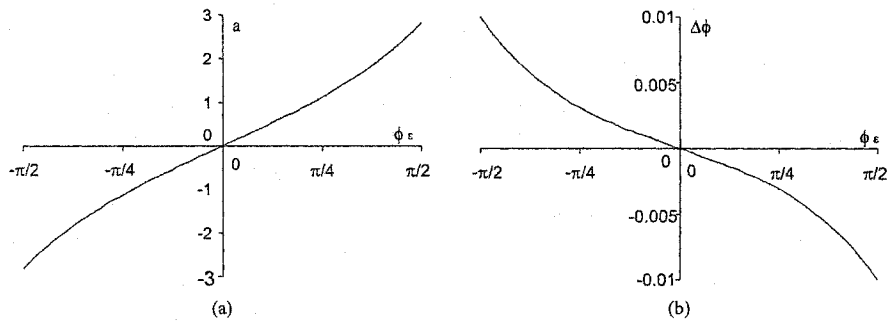
Figure 4.7: Both a and $\Delta\phi$ change monotonically with ϕ_ϵ in soliton pulse solution.
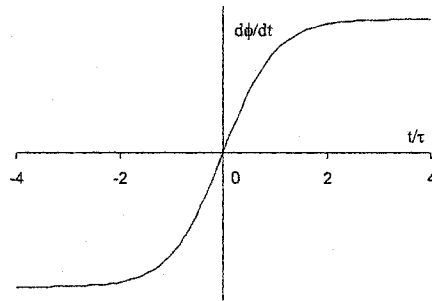
Figure 4.8: The first order derivative of the phase in the soliton solution is a function of a, here $a > 0$. As a changes from positive to negative with ϕ_ϵ, the phase changes its sign as well.

The phase described by Eq. 4.47 is plotted in Fig. 4.8 when $a > 0$.

We can now study F and F' by varying ϕ_ϵ, which is shown in Fig. 4.9. The plot shows the F and F' when ϕ_ϵ is positive. The F functions belong to two ϕ_ϵs with the same absolute value are identical. This is caused by the exchange of signs between ϕ_ϵ and $\Delta\phi$. The F function shows a similar behavior as that in the previous section, and changes gradually from that of the dispersion only case to gain filtering case as ϕ_ϵ decreases. So does F'. But F' is no longer symmetric around the pulse's peak. The maximum value of gain, denoting

g_m, shifts from $x = 1/2$ to slightly higher values, x_p,

$$x_p = \frac{1}{2} + \frac{sin(\phi_\epsilon - \Delta\phi) - sin(\phi_\epsilon)}{12a\alpha sin(\phi_\epsilon)}.$$ (4.48)

But since $\Delta\phi$ is always small, we can still approximate g_m by the value at $x = 1/2$. The maximum value of lost l_m occurs when $x = 0$. The approximation leads to a very useful result,

$$g_m - l_m = F'\left(\frac{1}{2}\right) - F'(0) = \frac{2}{cos(\phi_\epsilon)} \frac{\epsilon}{\tau^2}.$$ (4.49)

Eq. 4.49 relates the pulse duration to the nonlinear gain effect of system, which is a very simple way to estimate the pulse's duration. The linear relation between the τ^2 and ϵ is confirmed by the experimental data obtained from our CPM laser.
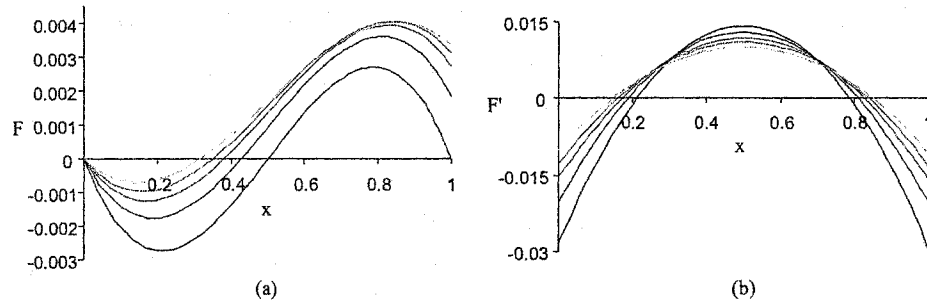
Figure 4.9: The $F(x)$ and $F'(x)$ in soliton-shaped pulse case are plotted by varying the ϕ_ϵ. The curves from the solid line to the dotted line are plotted as listed: $\phi_\epsilon = \frac{\pi}{2}^-, \frac{3}{4}\frac{\pi}{2}, \frac{1}{2}\frac{\pi}{2}, \frac{1}{4}\frac{\pi}{2}, 0^+$. Other parameters used in the calculation are: $\epsilon = 0.01$ and $\tau = 1$.

The $g_m - l_m$ is minimized when ϕ_ϵ is near zero, which is the dispersion-free case. In this case, the pulse's duration is the shortest, which is only limited by the bandwidth of the gain. On the other hand, when the dispersion effect dominates, the gain in a system needs larger nonlinearity to produce pulses with the same duration. But in all cases, a larger

value of $g_m - l_m$ not only enables the generation of shorter pulses but also suppresses noises to make the system more stable.

4.4 Numerical Investigations

To solve for the transfer function for Lorentzian and Gaussian pulses, we also investigated the bistable medium model with the numerical methods. The numerical calculation is based on Eq. 4.40. We took the following procedures in our numerical calculations: first, setting an initial point, $(0^+, F(0^+))$, by assuming $r(x)$ to be a linear function to avoid the singularity at $x = 0$; then using 4th-order Runge Kutta method to do a shooting process; finally, by searching in the parameter space, $\{\Delta\phi, \phi_\epsilon, \alpha, \Phi_m\}$, a single set of parameters and the correct curve of F(x) that satisfies the boundary condition Eq. 4.42 can be found.

The F and F' functions for a Lorentzian pulse show similar bistable behavior to that of the soliton. Due to the rigid singularity of the F function at $x = 0$ for a Gaussian pulse, we find it is hard to initialize the problem to obtain a reasonable numerical calculation. We proceed to analyze the relation between the $g_m - l_m$ and the pulse duration for these two pulse shapes. We again approximate the maximum of gain at $x = 1/2$. For Gaussian pulses, the loss at $x = 0$ is always infinity, therefore, we only keep the g_m term. The result for a Lorentzian pulse is

$$g_m - l_m = F'\left(\frac{1}{2}\right) - F'(0) = \frac{1}{cos(\phi_\epsilon)}\frac{\epsilon}{\tau^2},$$ (4.50)

and for a Gaussian pulse,

$$g_m = F'\left(\frac{1}{2}\right) = \frac{3}{2cos(\phi_\epsilon)}\frac{\epsilon}{\tau^2}.$$ (4.51)

These two equations show the generality of the relation between the nonlinearity of the gain and the pulse duration. It implies that same analysis can be applied to these two kinds of pulse as that in Section 4.3.
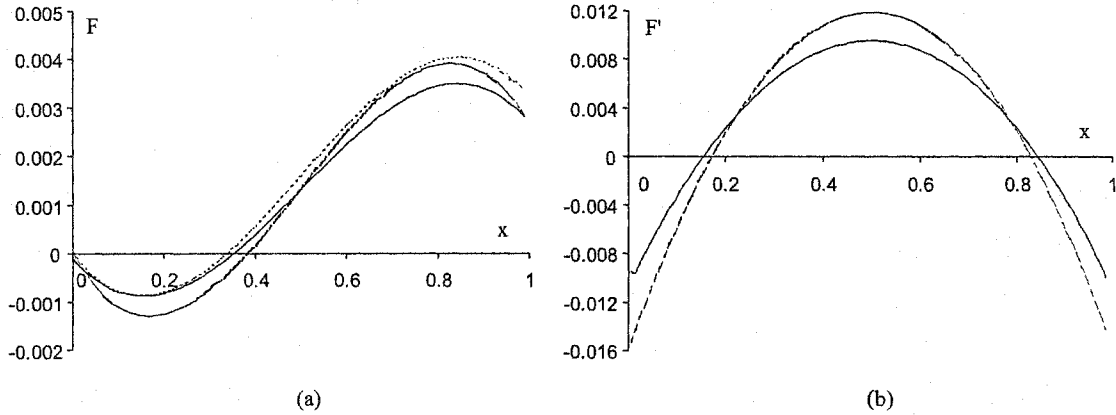

(a)   (b)

Figure 4.10: The $F(x)$ and $F'(x)$ in soliton-shaped pulse case with Kerr effect are plotted in solid line. It plots the curve of F without Kerr effect (dotted line), and also the F and F' without Kerr effect but fitting to the new boundary condition (dashed line). Other parameters used in the calculation are: $\epsilon = 0.01$ and $\tau = 1$.

We also investigated the Kerr effect using the numerical method. To include the Kerr effect, we need to add a new term to Eq. 4.8,

$$\rho e^{i\Delta\phi} = \left\{1 + F'\left[\Phi(t)\right]\right\}\rho + \tilde{\epsilon}\left[\left(\ddot{\rho} - \rho\dot{\phi}^2\right) + i\left(2\dot{\phi}\dot{\rho} + \ddot{\phi}\rho\right)\right] + i\epsilon\delta\rho^3. \qquad (4.52)$$

Here, the Kerr effect term has a factor $\epsilon = |\tilde{\epsilon}|$. The factor δ shows the relative significance of the Kerr effect to the dispersion. We also assume that δ is positive. By following the same process in Section 4.1, the following master equation, which we use in the numerical calculation, can be obtained

$$\begin{aligned}
\epsilon^2 \ddot{P}P/2 - \epsilon^2 \dot{P}^2/4 - \epsilon P^2 cos(\phi_\epsilon - \Delta\phi) + \epsilon P^2(F'+1)cos(\phi_\epsilon) + \epsilon^3\delta P^4 sin(\phi_\epsilon) \\
= \left[Fsin(\phi_\epsilon) + \Phi sin(\phi_\epsilon) - \Phi sin(\phi_\epsilon - \Delta\phi) + \epsilon\delta P\Phi cos(\phi_\epsilon)\right]^2,
\end{aligned} \qquad (4.53)$$

The numerical calculation shows that the new F and F' still have the bistable feature as those without Kerr effect. The parameters ϕ_ϵ and $\Delta\phi$ can be varied to compensate for the Kerr term. But ϕ_ϵ has to be negative. The system is no longer indifferent to the sign of GVD. The change of F is compared in Fig. 4.10 (a) by varying the two parameters. It shows the curves of F without Kerr effect (dotted line) or with (solid line), and also the curve of F without Kerr effect but fitting to the new boundary condition (dashed line). The latter two are valid solutions, and their F's are plotted in Fig. 4.10 (b).
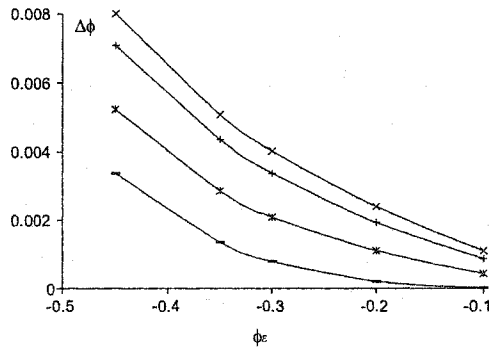
Figure 4.11: The same amount of Kerr effect can be accounted for by various combination of ϕ_ϵ and ϵ. The δ value for the symbols are 0 (crisscross), 0.2 (cross), 0.6 (asterisk), and 1 (hyphen), respectively. Other parameters used in the calculation are: $\epsilon = 0.01$ and $\tau = 1$. The ϕ_ϵ is plotted in unit of π.

It also turns out that the same amount of Kerr effect can be accounted for by various sets of ϕ_ϵ and ϵ. This is shown in Fig. 4.11. It indicates that when the system is dispersion dominated, the pulse tends to have longer delay at in its arriving time. When ϕ_ϵ is held fixed, the delay time increases with Kerr effect.

Chapter 5

The Experimental Apparatus

In this chapter, we will describe the experimental setup, our custom data acquisition circuit board, the USB technology we used in our data acquisition apparatus, and the processing of the time series data obtained in our experiment.

The experimental setup is shown in Section 5.1. The CPM laser's output has a repetition rate about 95 MHz. The dropout and dropin processes usually happen in a few microseconds, but some fast dropouts happen within 0.5 - 1 μ s, as plotted in Fig. 5.1. To obtain the data series on the laser's output, the experiment setup must have a very high sampling rate, which we chose to be 100 MHz. In our experiment, we also observed the second harmonic signals generated by the two output beams of the CPM laser. We found few commercial data collecting cards could match this demanding data acquisition requirement in 2000, when we started our experiment. So, we designed our own data acquisition system. Section 5.2 gives a detailed description of a custom data collecting card, the ADC5 board. A commercial universal series bus (USB) card is used to handle the communications between a PC and the ADC5 cardboard. Section 5.3 gives a short introduction to the USB technology we used in our data acquisition system. Using our data acquisition system, we are able to collect time series data around dropout and dropin processes and in various

75

operation modes of the CPM laser. The raw data obtained by the data acquisition system must be processed to restore the real power fluctuation. Section 5.4 shows the 16-point fitting procedure we used to process the raw data.
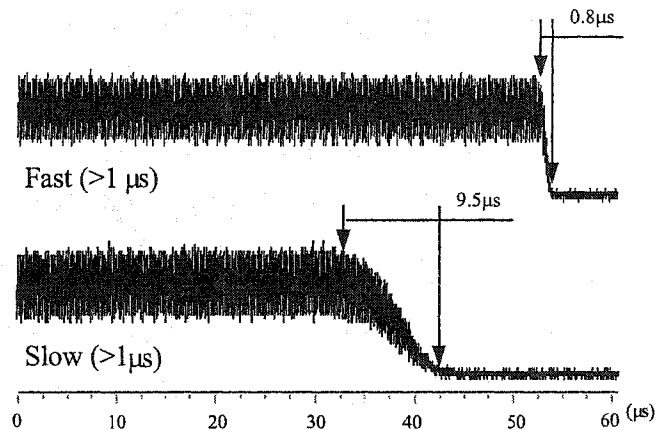

Figure 5.1: The curves plotted shows two typical dropout processes. The data is the raw data obtained directly for the ADC5 board.

5.1   Experimental Setup

The CPM laser's output consists of two pulse trains with the same repetition rate of 95 MHz. The fastest dynamics that can be observed is simply the fluctuation between two successive pulses separated by the round trip time of the laser, 10.5 ns. A complete measurement would therefore detect each pulse's power and duration for each of the two colliding beams.

The experimental setup we use to study the CPM laser consists of three parts: pulse fluence and duration detection, data acquisition, and the control program.

The diagram of the experimental setup is shown in Fig. 5.2.

In our experiment, pulse fluence detection is simply made by using fast avalanche photo-diodes. Since the two counter-propagating beams in the CPM laser may not be degenerate,
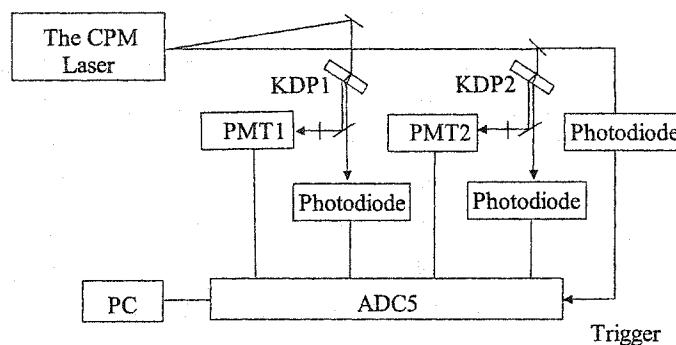
Figure 5.2: The experimental setup used to study the CPM laser.

we monitored both output beams. The pulse duration is also monitored using the second harmonic generation technique. A photo multiplier tubes (PMT) is used to detect the second harmonic signal generated in a KDP crystal by each beam. Another photo-diode serves as the detector for the trigger circuit on the ADC5 board.

The photo-diode we used for pulse power measurement is Hamamatsu's Si APD S2381, which has a cutoff frequency of 1000 MHz with 50 Ohm load resistance. Besides its fast response time, the S2381 also has a very high quantum efficiency (0.75) for photons in the range from 400 to 1000 nm, which is ideal to use in this experiment. The detector integrates the fluence of an input pulse (around 150 fs) and converts it to an electrical pulse with a duration about 2 ns. To avoid seeing no signal for most time in a cycle (10.5 ns), we stretch the pulses to be about 30 ns long using an LR circuit. The LR circuit is adjusted to match the impedance of downstream circuits.

The data acquisition board, ADC5, samples the photo-current signals generated by the photo-diodes and the PMTs and stores the data temporarily. A USB/SIMM device acts as an interface between the ADC5 board and a host PC. The PC controls the ADC5 board under operator control via a graphic user interface (GUI) created using C++ builder 4.0.

The USB/SIMM is also programmable. The C51 program on USB/SIMM is responsible to

pass on the instructions from the GUI program to the ADC5 board and transfer data from

ADC5 back to the PC.

The data acquisition system works like a simple oscilloscope. Its block diagram is shown

in Fig. 5.3.
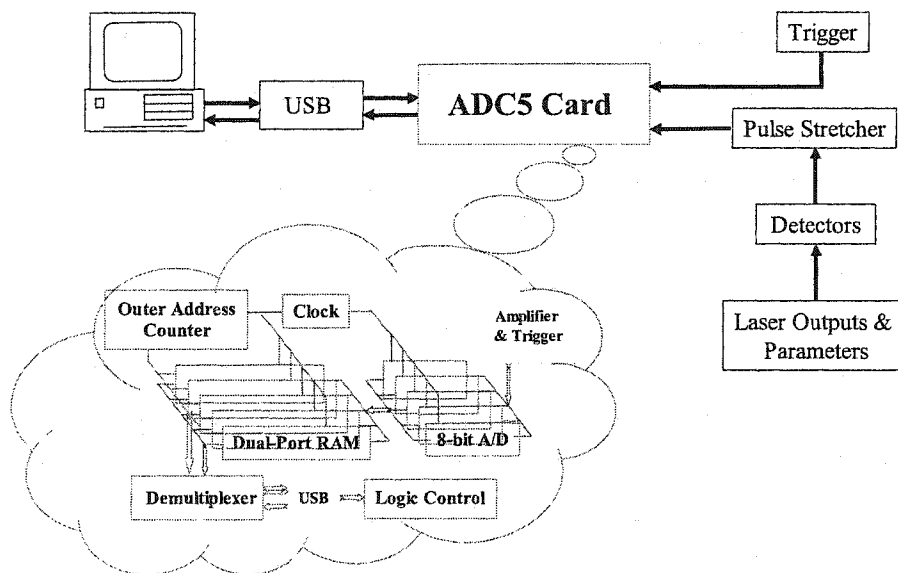
Figure 5.3: The functional diagram of the data acquisition system.

The GUI program initiates the commands to reset, start, trigger, and stop the ADC5

board in a data collecting action. The ADC5 board starts collecting and storing data upon

receiving a starting command. The ADC5 board will continue running until it is triggered

by the GUI program or by an external event. It then stops after an adjustable number

of samples after the trigger. The external trigger comes from a comparator on the ADC5,

which detects the change in the laser power. The PC then reads the data stored in the

ADC5 board.

With this system, we can record different kinds of dropouts and the laser's behavior before and after the dropouts such as the stop lasing and dropin processes.

5.2 The ADC5 Board

The ADC5 board is designed and implemented to synchronously record up to five channels of signals at a rate of 100 M Byte per second (Bps) in each channel. This circuit can be physically divided into two parts: the motherboard and five identical daughter boards. The circuit diagram is shown in Appendix C. Appendix C also lists the electrical signals commands the ADC5 board can execute.

5.2.1 The Daughter Board

Each daughter board performs the same basic functions of Analog-to-Digital converting (ADC) and data storing of one analog input signal.

A daughter board consists of a unity-gain amplifier, an ADC and a random accessible memory (RAM). The five daughter boards are removable from the motherboard, connecting by SIMM-Stick sockets. This modular structure makes it easy to debug and change one daughter board without affecting the others. All five daughter boards receive the same commands from the motherboard. The amplifier (CPA658) is a current feedback (CFB) amplifier, which has a bandwidth up to 900 MHz for unity amplification. On each daughter board, the amplifier uses unity gain configuration and offsets the signal to be around 2.5 V, which is the reference voltage of the ADC.

The ADC (AD9054) is an 8-bit A/D converter with a 350 MHz bandwidth. Its dynamical range is within 2-3 V. A crystal oscillator on the motherboard serves as the clock for the

ADC. Although the Nyquist limit requires the sampling frequency to be at least twice of the repetition rate, we chose the sampling rate on the ADC5 board to be 100 MHz, which is comparable to the repetition rate, since these elements were readily available. An alternative way to sample the data would be using a sampling frequency locked with the CPM laser's frequency with a proper delay. This method satisfied Nyquist limit by setting a fixed phase for each point measured, therefore it is a real shot-to-shot measurement. But, this method only works when the CPM laser is stable, not when it is in transitions.

The ADC converts the analog signal input into 8-bit digits. In our experiment, the ADC produces data at a rate of 100 MBps in each channel. And, the experiment requires at least 4 channels to monitor both outputs of the CPM laser and their second harmonic signals. In this situation, the data cannot be sent directly to the PC since the bandwidth required exceeds available PC input/output (I/O) devices.

The data is then transferred to the temporary RAM on board during the later half cycle of the ADC clock. We used the CY7C09089 dual-port circular memory with 100 MHz bandwidth and 64 K Byte capacity. The dual-port I/O design of the RAM makes it easy and fast to access the memory. The address of the RAM is obtained from an address counter on the motherboard.

5.2.2   The Motherboard

The motherboard provides a SIMM bus to communicate with the USB/SIMM board and controls the actions of the daughter boards. The motherboard use to ±5 V power supplies and connects them to the daughter boards.

The motherboard consists of a 16-bit address counter, an 8-bit delay counter, a SIMM

bus, a 100 MHz oscillator, a comparator, and accessory logic components. The ADC5 board

can perform five actions: reset, start, trigger, stop, and data transfer. These commands are

executed in the same order as listed in Appendix C to finish a data collecting cycle. The

motherboard controls the daughter boards using the same SIMM bus. We can illustrate the

function of the mother board by using a single daughter board, as shown in Fig. 5.4.
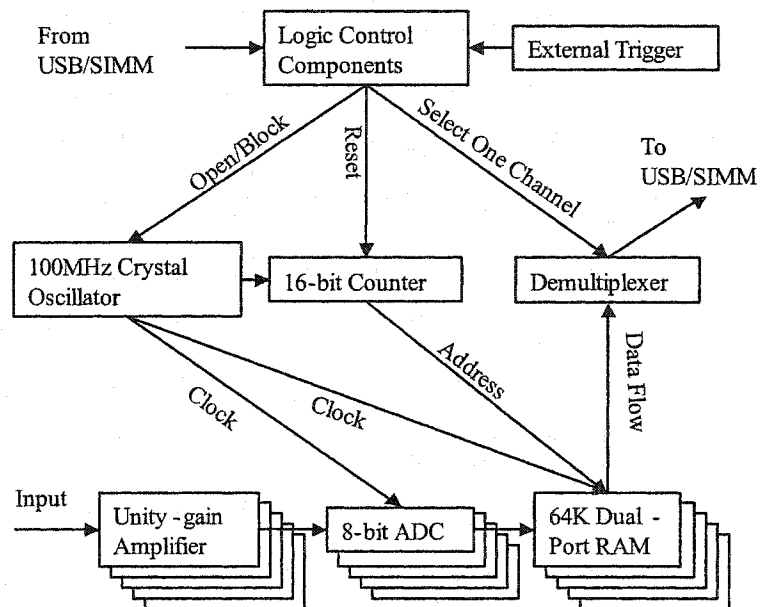

Figure 5.4: The structure of ADC5 board with a single input.

The reset command sent from the host computer stops the ADC5, clears the address

counter, and sets the delay counter to 0x40 to prepare for data collection. The start com-

mand starts the data collecting action by enabling the clock generated by the crystal oscil-

lator for the daughter boards. The ADC5 will continue running until it receives a trigger

signal, then it will stop after the delay counter reaches zero. During this time, the daughter

boards fill their memories with data using the addresses on the address counter. Since the

memory has a capacity of 64 KB, it can store a data series up to 0.65 ms long.

The external event trigger comes from a comparator on the motherboard. The compara-

tor compares the signal from a photo-diode that monitors the output of the CPM laser to a reference voltage. When the signal level drops below the reference voltage, the comparator sends a trigger signal to the logic on the motherboard. The delay time is determined by the variable RC time of the photo-diode circuit.

The stop command sends a software trigger signal to the motherboard. The software trigger works in the same way as the external trigger.

The transfer command starts data transfer from the ADC5 to the host computer. The transfer of data in the daughter boards to the USB/SIMM is controlled by a demultiplexer, which enables the selected daughter board and keeps the other boards' RAMs in the high impedance state. The 64 KB data in each RAM is transferred in order, starting from address 0. Each byte is transferred in parallel via the SIMM bus to the ports of USB/SIMM card, then to the host computer. In addition, the motherboard transfers three other items: the address of the counter upon stopping, a bit showing if the ADC5 stopped before the RAMs were filled at least once, and a bit showing hardware or software triggering. The GUI program uses these information to restore the correct timing of the data.

5.2.3   Issues in Design of ADC5

The photo-current generated in the photo-diode can produce a single pulse of 1 - 2 ns with its peak voltage about 500 mV. Since the time between pulses is 10.5 ns, we used a pulse stretching circuit to avoid sampling a signal that would be zero most of the time. The stretcher is a band pass filter that broadens a pulse to approximately the round trip time of the CPM laser.

The ADC5's amplifier is highly demanding in ADC5 since it must have a unity gain

for signals from DC to over 100 MHz. The amplifier we used has a broad bandwidth in a unity gain configuration. The CFB amplifiers are commonly used in high frequency circuits with better performance over the voltage feedback (VFB) ones. The CFB amplifier uses a different model in analysis. In a typical configuration, the input enters the amplifier via its inverting input, which has a small impedance compared to the VFB amplifiers. This situation complicates the impedance matching between the detector and the amplifier.

We solved this problem by varying the pulse stretching circuit to optimize the linearity of the amplified output. The resulting pulse stretcher circuit stretches the pulse from 1 - 2 ns to about 30 ns, but the impedance mismatch causes some high frequency ripples due to reflections. These ripples have a fixed pattern, which can be removed during analysis.

Another issue in the design of the ADC5 board is the power supplies. The ADC5 board needs ± 5 V power supply. The RF frequency ICs on the ADC5 board draw more than 1 A of DC current from the ± 5 V power supply. This heavy current load reduces the regulation of the power supply. In the digital part of ADC5, usually the current change is slow. But when the internal addresses of the memories reach the maximum, and all counter bits flip from 1 to 0 in less than 10.5 ns. This current change affects the power supply. In order to minimize this effect, the printed circuit board is designed to decrease the internal AC impedance of the power supply by increasing the capacity between the power line and the ground. In the data, small discrepancies around address flipping point exist. These discrepancies limit our data analysis methods to be valid only with short data pieces.

The photo-diodes and PMTs require high voltage power supplies, which must be routed to avoid RF noise and block reflections of the pulses.

5.3 The USB/SIMM Card

In our experiment, the choice of an I/O device is determined by its functional flexibility. The I/O device must be programmable to perform the basic functions needed by the ADC5 board. The speed of transferring data is a minor factor since real time transfer is hard to achieve. Yet, the I/O device should have a high data transfer speed since the data stored on the ADC5 board has an amount of 64KB in each channel. Therefore, we chose the programmable USB/SIMM card with a relatively broad bandwidth. This section will introduce the basics of the USB technology and the programming involved in the data acquisition system.

5.3.1 Basics of the USB Technology

USB technology started in 1995, and was designed to replace legacy ways of communication between personal computers (PC) and peripherals with a single and flexible interface. The specification of commonly used USB 1.1 was released in 1998. Since then, many computer peripherals were developed with USB connections and USB became fully supported in Windows 98. A USB device usually consists of a USB connector, a micro-controller, and other electronics. Comparing with legacy connection, the USB connection has many advantages, such as: single socket type, hot pluggable, high transferring speed, and device expandability up to 127 devices. USB also makes the development of peripherals easier since various USB micro-controllers and development boards are available.

USB peripherals are easy to use and develop. They are connected to PCs via USB cables. USB devices are hot pluggable, i.e. a USB device can be connected to computer

at any time. Once the USB device is plugged in, the PC automatically enumerates it and loads its driver. USB 1.1, which we used in our design, can transfer data at two modes: *full speed* at 12 M bit per second (bps) and *low speed* at 1.5 Mbps. Higher real time data transfer now can be achieved using latest USB 2.0 technology, 480 Mbps. USB devices can be powered by the PC, USB hubs or itself. This feature expands the number of devices connecting to a single USB port. By using hubs, 127 devices can share one USB port.

USB peripheral's outward simplicity is due to the internal complexity of the micro-controller. A USB cable consists of four wires: power, ground and two differential-signaling serial data lines. The micro-controller is responsible for decoding the serial signal, processing data using USB protocol, and communicating with other electronics with its I/O ports. The USB micro-controller provides eight pairs of I/O interfaces, known as endpoints, and four kinds of data transferring modes, which make its I/O highly flexible. The four transfer modes are: bulk transfer, control transfer, isochronous transfer, and interrupt transfer. We only use the bulk transfer and the control transfer in our experiment.

5.3.2 USB Programming

In our circuit, we used the Cypress AN2131 and the USB/SIMM development board as the I/O interface between the PC and our custom electronics. The Cypress Semiconductor EzUSB chip AN2131 is a widely used one among the USB micro-controllers, which uses Anchor Chips' technology. EzUSB AN2131 has a built-in enhanced 8051 processor and works in *full speed* mode. A very important feature of Anchor Chip's EzUSB controller is its re-numeration function, which allows dynamical downloading code to the USB controller. Based on the AN2131, J Gordon Electronic Design Inc. developed the USB/SIMM board.

The USB/SIMM board is a USB development firmware with expanded external RAM and EEPROM. The USB/SIMM board has two serial ports, an I^2C interface, and sixteen I/O lines. It can be connected to other electronics via a SIMM-stick socket.

Windows 98 is the operating system for our experiment. Windows 98 uses INF files to control activities associated with installing drivers. The INF file for a certain driver contains the device's description and the services available for it. The device description is stored in the identifier section of an INF file, and allows the operating system to recognize a device and to load its driver. For USB devices, this section looks like

USB /VID_ *vvvv*&PID_ *dddd*&REV_ *rrrr*,

where *vvvv* is the 4-digit hexadecimal vendor code assigned by USB committee to the vendor (VID), *dddd* is the 4-digit hexadecimal product code assigned to the device by the vendor (PID), *rrrr* is the revision code. All three of these values need to be assigned beforehand. Upon plugging in, the operating system will look up the values appearing in the device's descriptor or interface descriptor. If the driver exists, the operating system will load the registered driver and show in the system hardware profile that a new hardware device is available.

In our data acquisition system, we use a generic USB driver developed for the AN2131. By assigning a VID, a PID and a name for the ADC5 board in the INF file for the generic USB driver, the operating system can recognize the ADC5 board correctly and load the driver for it.

After loading the USB driver, the operating system provides I/O support so that applications can communicate with the USB device through the driver. The data flow in our data acquisition system is shown in Fig. 5.5.
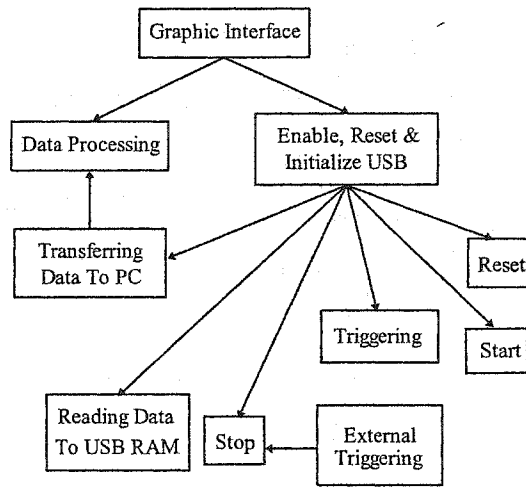
Figure 5.5: The diagram of virtual and physical data flows in the data acquisition system.

The GUI program and a set of framework programs running in the USB micro-controller are used to implement the data flows between the host computer and the USB/SIMM. The GUI program is written in and complied by the Borland C++ Builder 4.0.

The framework programs are written in C51 language and can be compiled using the Keil μ51 compiler. They configure and set the running mode of the USB device. They also contain the user-defined functions, known as vendor commands. These vendor commands are executable by calling their corresponding vendor request numbers.

Each time when we start the system, an executable HEX file compiled from the framework programs is downloaded to the USB internal RAM. The micro-controller then initiates the configurations of the USB/SIMM by setting the descriptor, VID, PID, and I/O interfaces. The operating system re-numerates the device to load the ADC5 driver, and refresh it in the hardware profile with its new identification. After initiation, the USB device will keep running a polling function that waits for calls from host computer and executes them.

After the initiating processes of the USB/SIMM, the GUI program is able to open the USB/SIMM device by calling system I/O functions, which issue a handle pointer for the USB/SIMM board. Then, the GUI is able to sent vendor requests to the USB/SIMM board, which in turn sends the commands to the ADC5 board to perform data collecting actions.

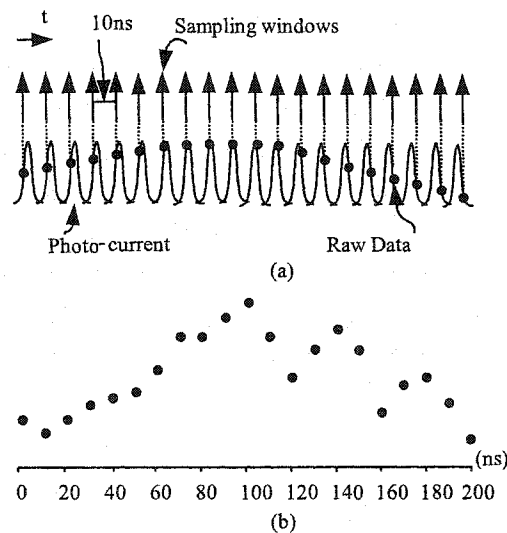The key functions in the GUI program and the framework programs are listed in Appendix D.

Figure 5.6: The ADC5 board works like a sampling scope, which causes modulation of the raw data. The dots in (a) demonstrate the origin of the modulation. The dots in (b) are the raw data we obtained with ADC5 board. Here one cycle of the modulation is plotted.

5.4 Data Fitting

The ADC5 board works like a sampling scope, since its sampling rate is just slightly higher than the CPM's repetition rate. The ADC samples the photo-current at different part of the pulses. Therefore, the raw data we collected has a modulation on it. Fig. 5.6 (a) shows

where the modulation comes from. The arrows illustrate the very short time the ADC needs to perform a sampling action. The sampling time for our ADC is very short, about 400 ps. Though the signals to be sampled have the same profile (identical pulses), the out-of-pace sampling process cause a modulation in the raw data (the dashed line). In this case, the pulse profile can be recovered by rescaling the time of the data.
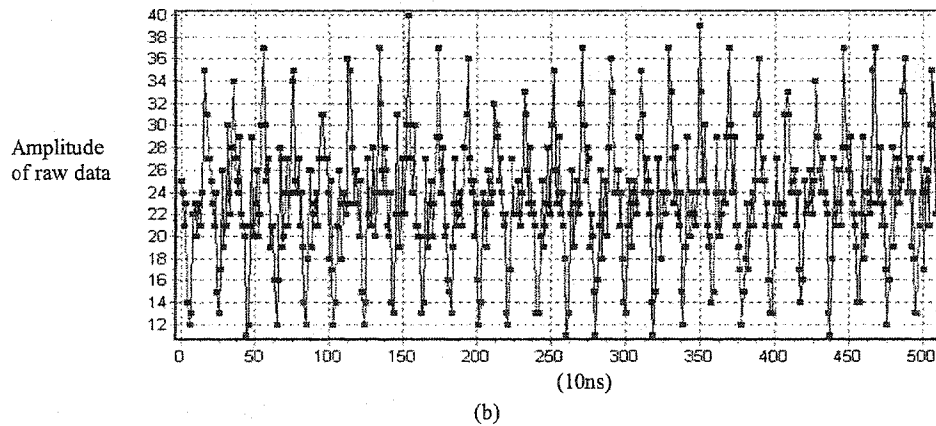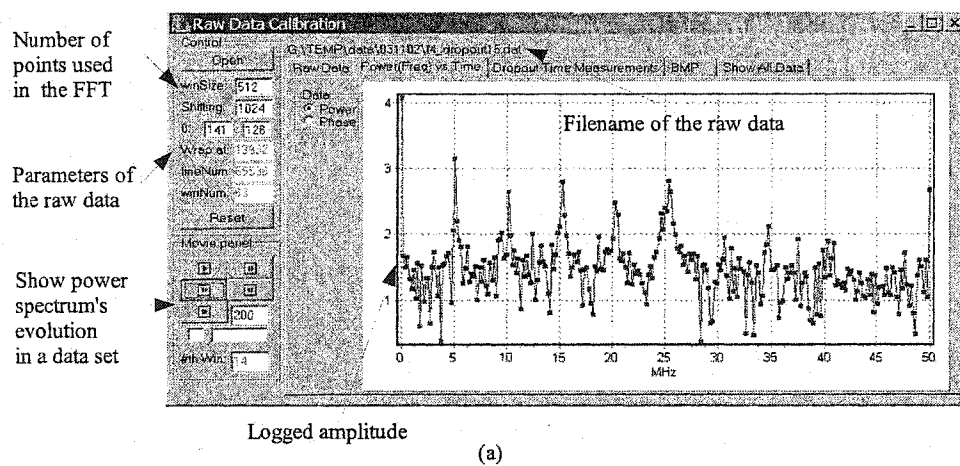

Figure 5.7: The power spectrum of the raw data in (a) shows a few strong frequency components. The lowest one around 5MHz is the modulation frequency, which is the beat frequency of the repetition rate and the sampling frequency. This picture is the screen shot generated by the 2D-correlation program we developed to analyze our data. The 2D-correlation program will be introduced in detail in Section 6.2.2 (b) shows the raw data from which the power spectrum is calculated.

Fig. 5.6 (b) shows a cycle of the raw data we obtained when the CPM laser is operating

in stable mode-locking mode. The ripples on top of the modulation are caused by the reflection as we discussed in Section 5.2.3. The profile of the modulation varies a little from cycle to cycle due to the fluence fluctuation of the CPM laser's output.
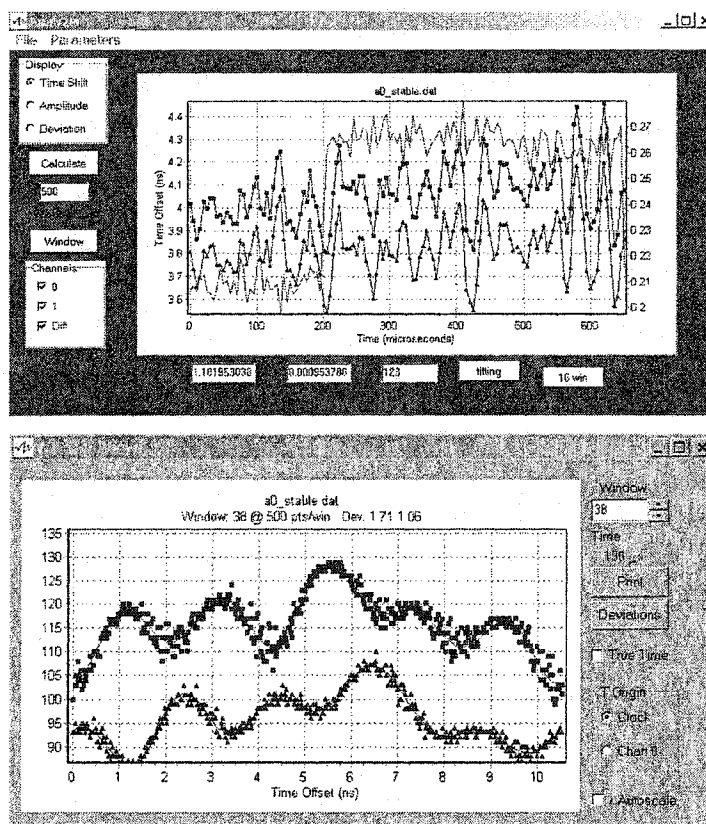

Figure 5.8: This figure depicts the screen shots of the C++ program, Analyzer. The pictures are generated in the first step of the fitting process in which 500 points are used to obtain the modulation frequency and the wave form of the modulation. The three curves plotted in (a) are the two channels of data and their difference (the light curve with its amplitude showing on the right). (a) shows that the modulation frequency is accurate. The small discrepancy on the difference curve is caused by the power surge on ADC5 board during the memory addresses flipping. (b) shows that the fitting is a satisfactory. The dots are the raw data wrapped at exact modulation period, and the wave form obtained is the solid line buried in the dots.

Noticing that even the fastest dropout lasts several tens of samples $(0.5\mu s)$, we used a 16-point fitting process to recover the amplitude of the signal. We developed a C++ program, Analyzer, to do the fitting.
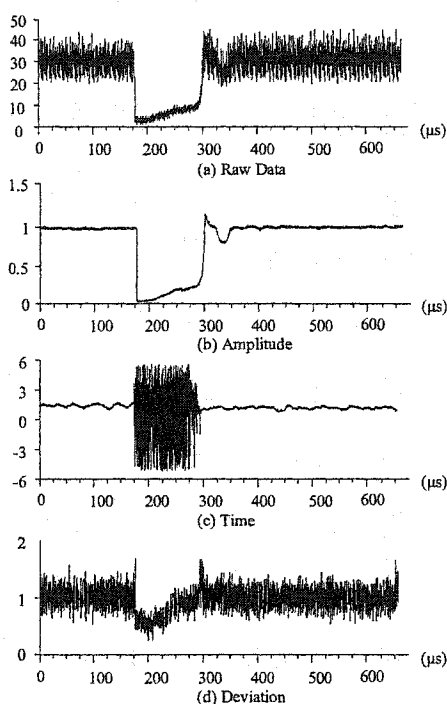
Figure 5.9: The fitting of a typical data set using 16-point fitting method generated (b) amplitude, (c) time, and (d) deviation (rms) data. The modulation in the raw data completely is removed in the fitted data. Each point of the new data is the average of 16 points, or 0.16 μs. The amplitude shows that the fluctuation of the CPM laser's power is very small while running in a stable mode-locking mode. It also reveals that the dropout is a smooth curve and the dropin has some structures, which were blurred by the modulation. The time data shows the phase delay of the 16-point windows relative to wrapping period. It also has a very small fluctuation except in the stop lasing part where the time offset is not well defined. The unit for the time data is in nanoseconds. The deviation of the fitting process is very small considering the size of modulation on the raw data. It is slightly higher during dropout and dropin where the function form changes wildly and is small during the stop lasing period. This small deviation supports the validity of the fitted data.

We found that the power spectrum of the raw data has several strong frequency components corresponding to the modulation frequency and its harmonics, as shown in Fig. 5.7. We can fit the wave form of the modulation using the sum of these frequency components. In the Analyzer program, we first find the amplitude and phase parameters of these frequency components using a 500-point data window. In this step, the modulation frequency is a critical parameter. If the modulation frequency is not exact, the time offset calculated
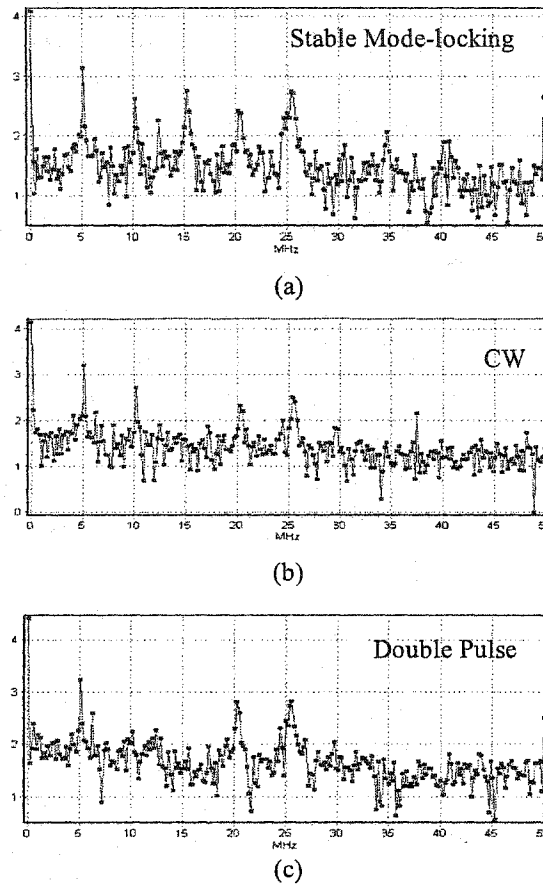
(a)

(b)

(c)

Figure 5.10: The wave forms for the data in stable mode-locking mode, CW mode, and double pulse mode are different. The differences is shown here by their power spectrum. Though the amplitudes of the harmonics in the CW mode and double pulse mode data are different from the stable mode-locking mode data, the 16-point fitting can effectively remove the modulation and reveal the power fluctuation in these data.

for each 500-point window will has a linear slope. Otherwise, the time offset shows a very

small fluctuation. So we can use the time picture to estimate the accuracy of the modulation

frequency. Fig. 5.8 shows the screen shots generated in this step by the Analyzer program.

Then, by keeping the parameters for the harmonics fixed, we use a 16-point window to fit

for the average amplitude and phase for modulation frequency component. The amplitude

we obtained in this way is the average amplitude of the 16 points or pulses. In the fitting

process, we used the amoeba simplex algorithm to make the searching of the 34 parameters in the fitting function converge quickly.

Using Analyzer, the calculation is simple and fast. The fitting we performed on a typical dropout and dropin data set is shown in Fig. 5.9. Since the two output beams of the CPM laser always have very strong correlation, only one channel is plotted.

We also apply this 16-point fitting method to the CW data and double pulse data. The wave forms need to be re-fitted for these data since the photo-current signals are significantly different from that produced in stable mode-locking mode. Fig. 5.10 shows the comparison of the raw data using their power spectrum.
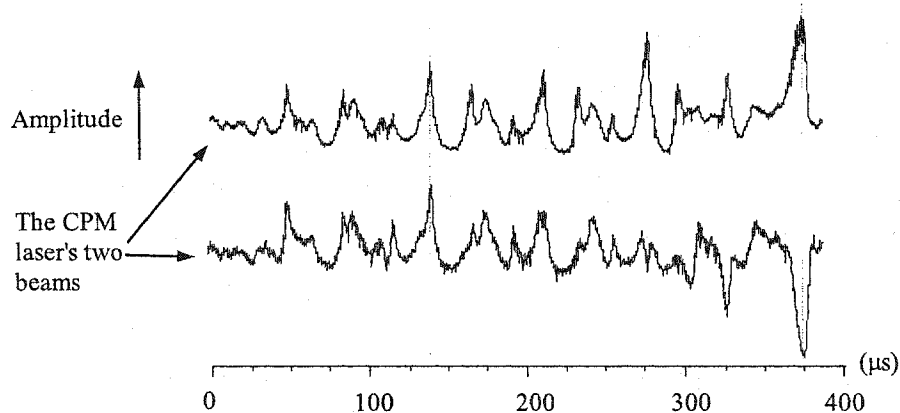
Figure 5.11: The amplitudes of the two beams of the CPM laser operating in CW mode can be either correlated or anti-correlated. The curves are offset for clarity.

The amplitude data obtained by fitting a CW data set is shown in Fig. 5.11. In the CW mode, long pulses form in the CPM laser. The pulses in the two beams sometimes lose synchronization. In contrast to the stable mode-locking mode in which the two beams are very well correlated, the picture shows that the two beams may be correlated or anti-correlated in the CW mode.
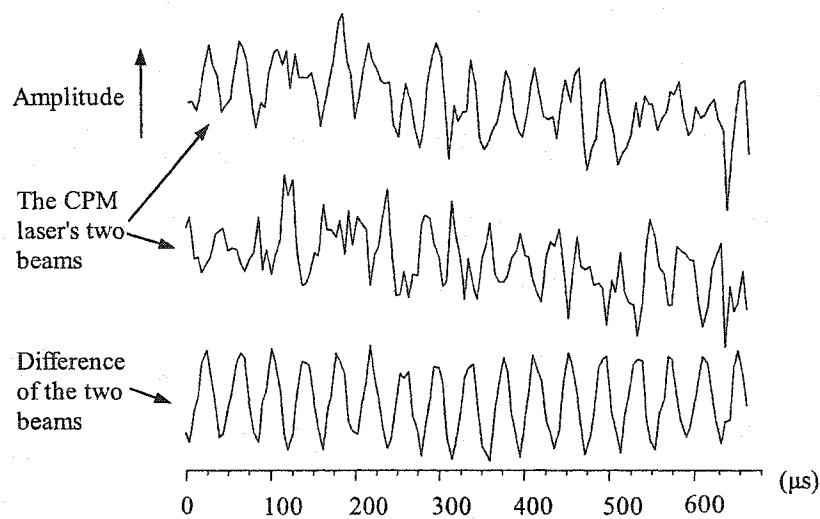
Figure 5.12: The amplitudes of the two beams of the CPM laser operating in double pulse mode display no obvious correlation, their difference changes regularly. We observed this orderly interaction in all the double pulse data. The curves are offset for clarity.

The double pulse data shows interesting result that the two beams actually interact in an orderly way in the double pulse mode. To better illustrate this phenomenon, we use a 500-point fitting process instead. Fig. 5.12 plots the amplitude data of the two beams and their difference.

The frequency of the modulation in the difference data shown in Fig. 5.12 is about 25 KHz. We find this frequency may vary from one set of data to another, but not much under the same experimental condition. The highest modulation frequency we observed in double pulse data is about 100 KHz.

Our experimental data also includes second harmonic time series. Due to the very weak signal produced in SHG process, the second harmonic photo-current must be amplified with a huge gain. So, the preamplifier used can only amplify the AC signal. The second harmonic time series, therefore, consists of AC data. The 16-point fitting process can be
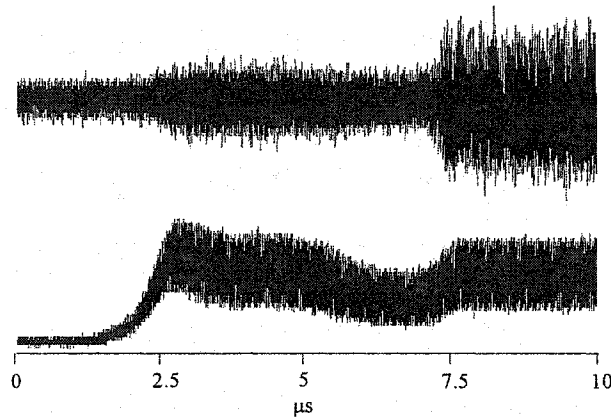
Figure 5.13: The second harmonic signal shows that during dropin process, the overshot of power is caused by long pulses with higher power rather than extremely short pulses.

applied to AC data, but the result only demonstrates the pulse width fluctuation, not the real width. We found that the second harmonic data is also too noisy and inaccurate to be used in searching of the dropout precursor. But it provide very useful information about the pulse width's evolution during dropout and dropin process. During the dropout processes, the second harmonic's drop is monotonic as that of the laser's power. But during dropin process, the second harmonic signal shows that even sometimes the power is higher than that in stable mode-locking mode, the second harmonic signal is still small. This result implies that during the overshoot of power in dropin process, the pulses are longer than that in stable mode-locking mode. Fig. 5.13 depicts a typical dropin process and its second harmonic signal.

Chapter 6

Analysis of Experimental Results

The operational characteristics of the CPM laser are elusive due to its alignment, many parameters and noise. We successfully optimized the operational conditions of the CPM laser in our experiment and mapped its operation modes in the parameter space, so that we could observe the dynamics of the CPM laser with consistency by best ridding it of the uncertainties. The study of the operational characteristics of CPM laser appears in Section 6.1.

We also studied the dropout and dropin phenomenon in an attempt to improve the stability as well as gain insights into the dynamics of the laser. We calibrated the dropout and dropin processes and searched for possible precursors before dropouts in Section 6.2.

6.1 Operational Characteristics

In the CPM laser, various parameters, such as the gain, the absorber, and the GVD, are adjustable, which causes the CPM laser to have versatile operational characteristics. The operation of the CPM laser is further complicated by the alignment and noise conditions. Section 6.1.1 illustrates the influence of alignment upon the operation of the CPM laser and

the technique we use to achieve repeatable optimized alignment. The pump power and the dispersion are important parameters affecting both the operational modes and the output of the CPM laser. The discussion of these two parameters appears in Section 6.1.2 and 6.1.3. Section 6.1.4 demonstrates the various side-bands we observed in the CPM laser's output, which attribute to the noise generated by the pump laser.

6.1.1 Alignment Conditions

The alignment of the CPM laser is a demanding task due to the many components in the cavity. Unless properly aligned, it is hard for the CPM laser to start mode-locking and produce pulses with good spatial, temporal, and spectral properties. Our experiment also requires a repeatable alignment to make the observations consistent.

Poor alignment typically requires a higher pump power for the laser to self-start. This is usually caused by incorrect positioning of the mirrors around the gain and the absorber jets. Another sign of poor alignment is that it is hard to achieve mode-locking in the CPM laser though CW can be produced with very high power, which is often caused by the mis-positioning or tilting of the prisms out of plane. Proper alignment of the CPM laser follows these procedures:

First, the CPM laser should be aligned without the prisms to make fine adjustment of the gain. The gain area in the gain jet is very small. Since the focused pump beam and the laser beam need to overlap in a small area, the adjustment must be very accurate. When this is done properly, our CPM laser operates in a CW mode with a threshold as low as 0.8 W and a central wavelength around 580 nm. This task must be accomplished simultaneously with aligning the gain jet to be vertical and the beams to stay in the same

horizontal plane.

Second, the prisms should be inserted into the cavity by translating the two end prisms

to intersect the beam. Under ideal conditions, the laser will start lasing right away. The

threshold usually increases by about 0.5 W under good alignment conditions. Mode-locking

will not occur since loss is still linear now. The output power increases linearly with the
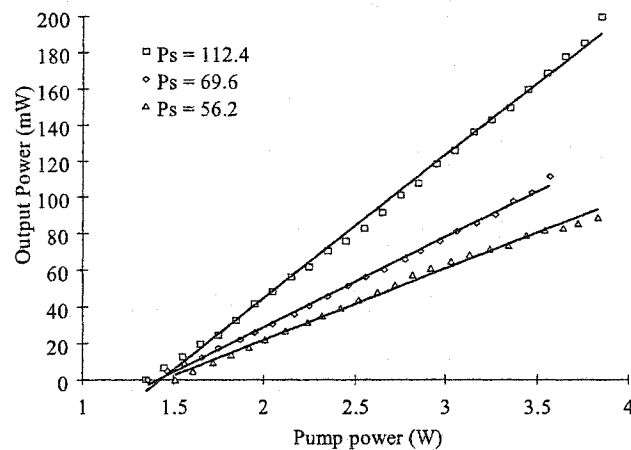
pump power as shown in Fig. 6.1.

Figure 6.1: The output power of the laser (without the absorber in the cavity) is plotted as a function of pump power under three different alignment conditions. Without the absorber, the cavity loss is linear so that the CPM laser operates in a CW mode. The output power increases linearly with the pump power in all alignment conditions. Depending on the alignment condition, saturation intensity of the gain, P_s (in mW), varies as shown in the picture. To achieve optimized alignment and lowest threshold, P_s must be maximized, i.e., the $P_s = 112.4$ mW curve shows the best alignment of the cavity among the three curves.

In this configuration, the CPM laser has a broad tunable bandwidth allowing many

longitudinal modes to lase without mode-locking. The result is that the output power

consists of very long pulses (ns) and fluctuates wildly in the CW mode.

We can estimate the gain and the linear loss in this mode using the experimental data

shown in Fig. 6.1. A stable running operation requires $g = l_0$, where l_0 is the linear loss

and g is the saturable gain. Similar to Eq. 3.3, g can be written as

$$g = g_0 \frac{1}{1 + QP/P_s} \qquad (6.1)$$

with P as the output power. The Q is the quality factor of the cavity with a value about 100 in our system. In small signal case,

$$g_0 = \frac{I_p}{I_t}, \qquad (6.2)$$

where I_p and I_t are the pump's intensity and its intensity at threshold. Then, we can rewrite Eq. 6.1 as

$$I = \frac{P_s}{Q l_0 I_t} I_p - \frac{P_s}{Q}. \qquad (6.3)$$

By least square fit, we can find the saturation power in different alignment conditions. The loss is primarily caused by the output coupler which has one percent transmission rate in our CPM laser. In the best alignment condition in Fig. 6.1, $l_0 = 0.014$, which is close to what we expect. P_s's change attributes to the changes of wavelength of the laser and the active area in the gain.

The last step is to translate the absorber into place. One nearby end must be adjusted slightly. The absorber must be placed in the tight focusing point to meet the stability criteria of mode-locking. But this restriction is looser than that for the gain, since the laser mode-locks as long as New's stability condition is satisfied. In fact, when excessive gain is present in the cavity, the absorber can be moved away from the focal point to avoid CW operation. Sometimes, adding in fresh absorber dye improves the mode-locking quality. Then, slightly walking the two end mirrors can achieve the best laser alignment. With the absorber added in, the threshold rises to around 2.7 W.

The CPM laser can also lase and sometimes achieve mode-locking when the prism sequence is absent from the cavity. But the mode-locking is very unstable.

As a measure of planar alignment of the cavity, we observe the reflections of the beam from the gain and the absorber. The gain and the absorber are placed at the Brewster angle relative to the incident beam. Due to the focused beam's angular divergence, the center part of the beam has less reflection than that of the rest of the beam, which appears as a shadow in the center of such a reflection as in Fig. 6.2. The reflection also allows us to estimate the beam sizes at the focal points. When the laser is running in CW mode, the interference of the light reflected from both surfaces of the dye jet produces vertical fringes. But when it is mode-locked, the pulse is shorter than the double thickness of the jet and shows no interference.
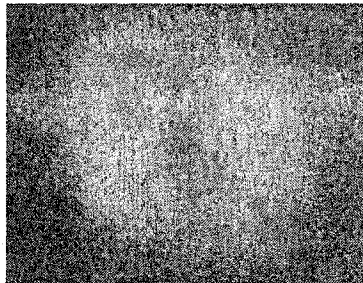
Figure 6.2: The reflections from the gain and absorber surfaces can be used to observe the incident angles of the beams and the size of active areas in the dye jets. This picture is taken when the CPM laser produces ultrashort pulses.

By observing the patterns of the reflections, we can ensure good and repeatable alignment in our experiments. The major uncertainties remaining in our measurement come from the temperature change of surrounding environment and the aging of the dye. To minimize these factors, the measurements are made only when the temperature has stabilized and

drops of fresh absorber dye are added on a daily basis.

6.1.2 Running Modes

The CPM laser can operate in three different states: CW mode, steady mode-locking mode, and double pulse mode. Each mode has its distinctive features.

The CW mode occurs either when the pump power is excessively high or the intracavity GVD is near zero or is positive. The pulse power fluctuates wildly in both cases, but the CW operation is stable. The spectrum of the output is very narrow. In the CPM laser, the CW mode can be avoided by moving prisms to adjust intracavity GVD and by reducing the pump power.

The double pulse mode occurs when the pump power is excessive. The spontaneous emission grows after the main pulse and avoids loss by passing through the absorber before its recovery. The satellite pulses form in a gain-efficient way that the pulses in counter-propagating beams tend to anti-collide in the gain. This behavior causes the satellite pulses to lag about one fourth round trip time after the main pulses in both beams with a lower power. The spectrum of the two pulses overlaps and shifts to the red compared to that in stable mode-locking mode. The total power goes up to a little less than twice the power of pulses in mode-locking mode. The pulse width of the two pulses in a beam cannot be measured by an auto-correlator. But their very broad spectrum indicates the beam consists of ultrashort pulses. The operation in the double pulse mode is extremely unstable and the laser jumps between modes. The double pulse operation is easy to stop by increasing the loss slightly in the cavity. This can be done by adding a few drops of absorber dye, by moving absorber away from the focal point, or by reducing the pump power.

In our experiment, the CW and double pulse modes are intentionally avoided to focus our study on the dropout and dropin events. The CPM laser was kept running in a stable mode-locking mode when we recorded these events. The influence of the pump power is shown in Fig. 6.3.
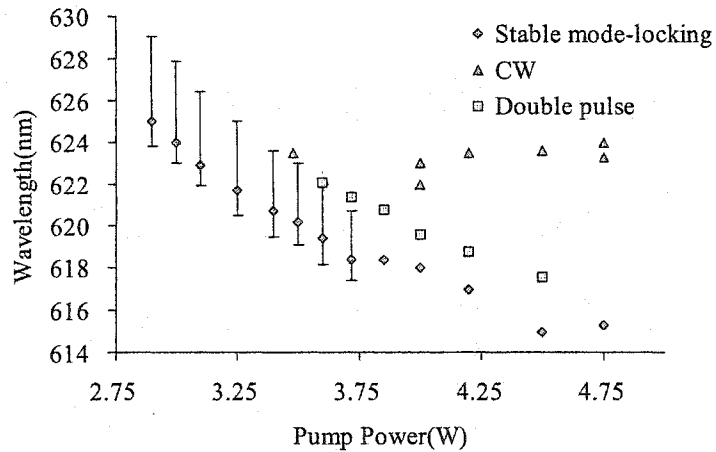

Figure 6.3: When the pump power increases, the spectrum of the laser's output changes. The spectrum properties of the three different operational modes under different pump conditions are plotted: in the CW and double pulse mode, the wavelengths at the peak of the spectrum (triangle symbols and square symbols); in the stable mode-locking mode, the wavelengths at the peak and FWHM of the spectrum, (diamond symbols and the error bar). The spectrum and pulses' duration in the double pulse mode, and sometimes in stable mode-locking mode are unstable. The wavelengths are determined by the gain spectrum under different pump conditions.

Higher pump power also causes pulse power to increase. But the pulses' duration change is caused by the pump power and is very small as shown in Fig. 6.4. It is intuitive that the pulses' power increases with pump power. But according to Eq. 4.49, which is copied for convenience,

$$\tau^2 = \frac{2}{cos(\phi_\epsilon)} \frac{\epsilon}{g_m - l_m},$$ (6.4)

both the maximum gain, g_m, and ϵ increase with the pump power, therefore, the pulses' duration change is hard to predict.
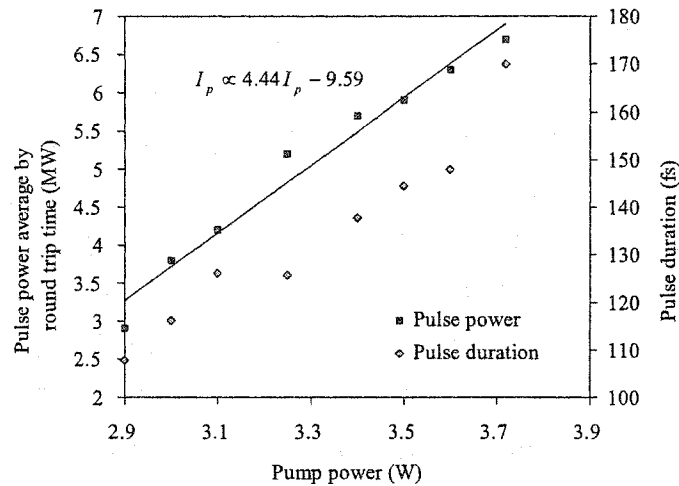
Figure 6.4: The output pulses' power and duration both increase when the pump power increases. But the pulses' duration change is very small.

6.1.3 Dispersion Effects

The dispersion, especially, the GVD, can significantly affect the stability (or running modes) of the CPM laser and duration of the output pulses. The total intracavity GVD is adjustable from positive to negative by changing the prisms' depth in the beam.

In our CPM laser, the intracavity GVD is normally negative in the stable mode-locking mode. When we increase the GVD by translating the prism deeper into the beam, the pulse duration decreases. We use an Optical Multi-channel Analyzer to observe the spectrum and an auto-correlator to measure the pulses' duration at the same time. The result of the measurement is plotted in Fig. 6.5. The cavity length also changes when we adjust the prisms, which causes frequency pulling effect. When the GVD is close to zero, part of the spectrum is in the regime where the GVD is positive. Due to the effect of third order dispersion (see Section 3.3.3), double humps appear in the spectrum causing the output to
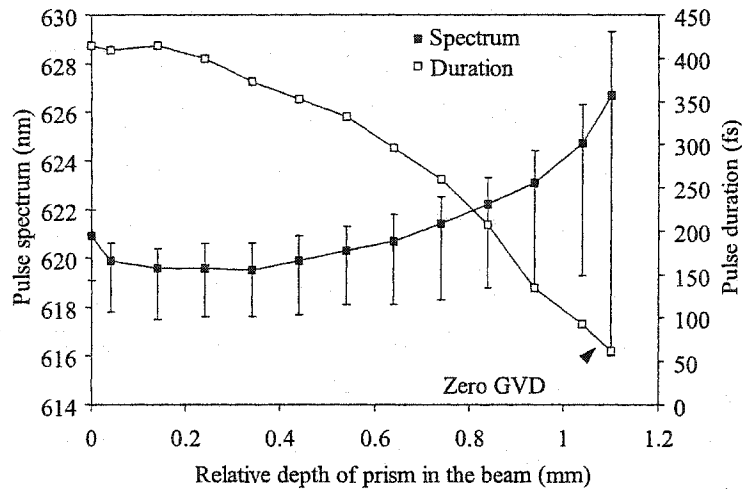
Figure 6.5: The spectrum (peak and FWHM) and duration of the pulses are plotted as functions of intracavity GVD. The GVD increases with the depth of prism in the beam from negative to around zero (from left to right). The pulses' duration decreases and spectrum width increases when GVD changes from negative to zero. When the GVD is close to zero, the spectrum shows double humps and significant increase in its FWHM and the pulse is shortest and unstable. The peak wavelength's shift is the combined result of frequency pulling of the cavity and the gain spectrum.

be unstable.

The bistable medium model predicts the relation between the square of pulse duration and GVD to be linear as shown in Eq. 6.4. In this case, ϵ solely describes the GVD. The experimental data shows the linear relation as predicted (see Fig. 6.6). The Ti:sapphire laser's data plotted in the same figure is provided by Dr. Chaloupka and R. Yang in Physics Department in the College of William and Mary.

We can use the experimental data to compare the $g_m - l_m$ factors in these two systems. Considering the prism sequences in both lasers, the CPM laser only changes one pair of its four prisms when doing the translation; while the Ti:sapphire laser employs 2-prism double pass configuration, the translation changes two pairs of prisms equivalently. With
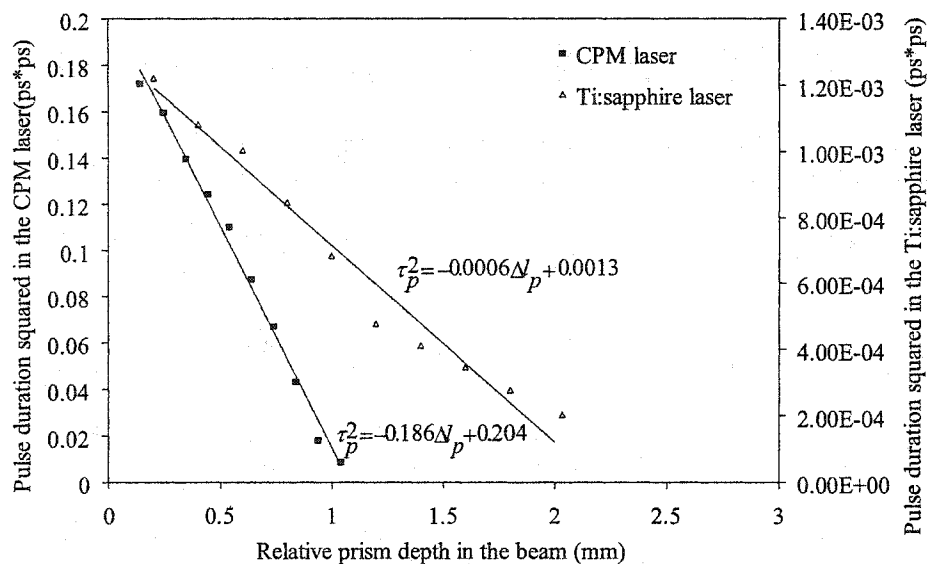
Figure 6.6: The square of pulses' duration changes linearly with intracavity GVD (negative to 0) in both the CPM laser and the Ti:sapphire laser.

this modification, we have

$$\frac{(g_m - l_m)_{Ti:sapphire}}{(g_m - l_m)_{CPM}} = 4.34. \tag{6.5}$$

It shows that the Ti:sapphore system has much larger nonlinearity in its transfer function.

This result is justifiable since the Ti:sapphire laser has a gain (10% output coupler) about

5 times bigger than that of the CPM laser (two 1% outputs).

The adjustment of prism pair also causes the repetition rate of the pulse to vary. This

effect is calculated in Appendix A. The calculation predicts the shift of repetition rate is

about 18 KHz per mm of prism's translation, which is confirmed by observing the pulse

repetition frequency on an RF spectrum analyzer. In the Ti:sapphire laser, this number

should be doubled.

Fig. 6.7 shows the pulse fluence variation with dispersion. Under most of the GVD

conditions, the power of one beam of the laser remains stable around 6 mW. But when the
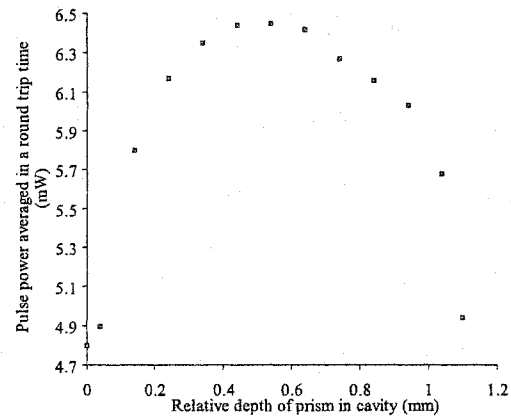
Figure 6.7: The variation of pulse's power as a function of intracavity GVD. The power declines when the GVD is around zero. The gain spectrum filtering effect becomes bigger as the GVD approaches zero, which is minor tradeoff of power for producing shorter pulses.

GVD is very large or near zero, the power declines. When we collected the data for dropout and dropin study, we never chose the GVD to be around zero to obtain a reasonable power output as well as good stability.

6.1.4 Noise

In the CPM laser, various noise sources degrade the quality of the output pulse trains. The noise in the CPM lasers with similar configuration as ours has previously been studied by several groups [54, 55, 56].

One widely used method to detect noise in the CPM laser is to observe the photo-current of an optical pulse using RF spectrum analyzer. Theoretically, the amplitude noise, phase noise and the timing jitter can be measured by this method [57]. But actually, only the power spectrum is measurable by this method due to the bandwidth limit of the photo-detector and the analyzer. The CPM laser output is observed to have spurious side-bands

caused by the pump laser and estimated to have very small time jitter (<50 fs rms [54, 55]) at high frequency.

In our experiment, we used a spectrum analyzer to observe the photo-current generated by a fast photo-diode. The photo-diode has a rising time of about 200 ps. Instead of a single frequency component, many harmonics of the photo-current are seen on the analyzer. The higher harmonic components of the CPM laser signal are only copies of the fundamental component. The fundamental component of the power spectrum shows a series of side-bands, which arise from the coupling of the modulation frequency of the pump, the Argon ion laser, and the CPM cavity. The modulation of the Argon ion laser is observed as shown in Fig. 6.8. When the length of CPM laser's cavity changes, the side-bands are observed to
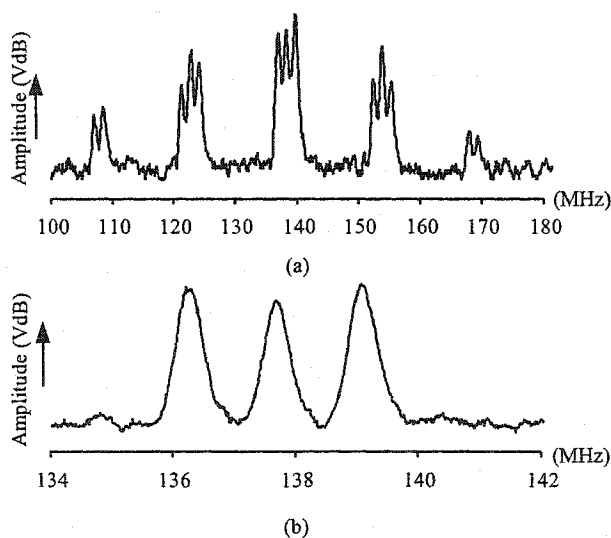
Figure 6.8: The spectrum of the pump laser, the argon ion laser, shows modulation around 133 MHz. The modulation shows five big frequency components as shown in (a). A close look using narrower band filter reveals that each of the five components consists of three peaks as shown in (b). The modulation is caused by the beating of various longitudinal modes in the argon ion laser.

shift accordingly. The shift of the side-bands with cavity length is shown in Fig. 6.9 (a).

In addition to the pump modulation side-bands, we observed a very small side-band

Figure 6.9: (a) The spectrum of the photo-current signal on the detector varies as the length of the cavity increases (from bottom up) by moving a prism. A pair of small side-bands (indicated by the arrow) and their harmonics emerge and shift during the process. The relatively strong peak to the left of the fundamental frequency around -4MHz is the noise in the air. The curves are offset for clarity. (b) As cavity length increases, the side-band shifts away from the fundamental frequency component linearly at the same rate as shown in the calculation.
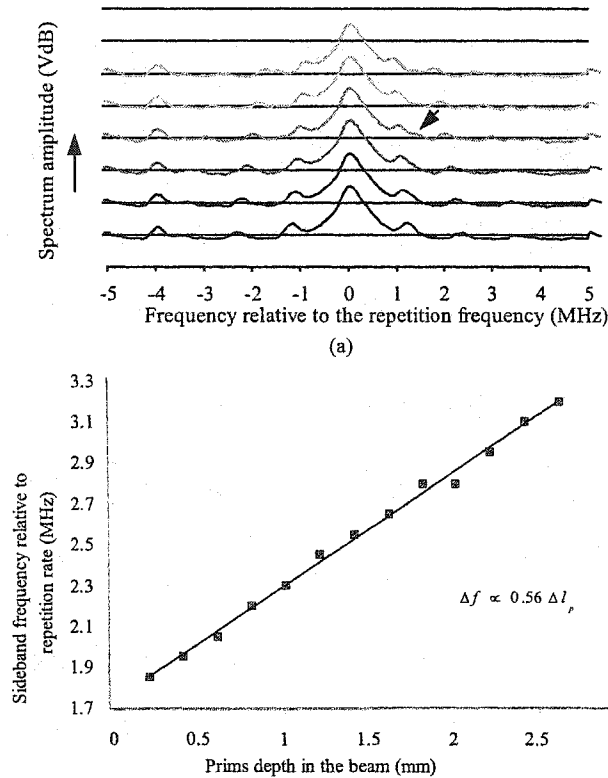
(-80 dB of the maximum peak). This small side-band exists even when the laser turns into CW or double pulse mode. Therefore, we are able to measure its frequency shift with good precision by elongating the cavity several millimeters. The frequency shifts linearly with the cavity length, which is shown in Fig. 6.9 (b).

This small side-band also shifts with the pump power as plotted in Fig. 6.10. But a good measurement is not possible due to its small amplitude and the very small frequency shift. This side-band has little effect on the output power but may be related to the dispersion of
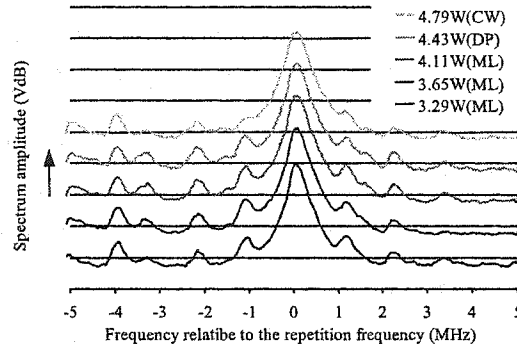
the cavity. But its origin is still unknown.

Figure 6.10: The spectrum of the photo-current signal varies with pump power. A pair of very small side-bands (indicated by the arrow) and their harmonics emerge and shift during the process. The side-bands shift away from the fundamental frequency component when pump power increases. As the power increasing, the CPM laser turns into different operation modes. The small peak to the left of the fundamental frequency around -4 MHz (91 MHz) is the noise in the air. The origin of this modulation is still unknown. The curves are offset for clarity.

The understanding of noise in the CPM laser is very important in the control of the CPM laser's performance. As mentioned in Chapter 1, there were efforts to stabilize the CPM laser by stabilizing the pump and to remove timing jitter by adjusting the cavity length using an error detecting and feedback circuit. Yet no one has investigated the dropout and dropin behaviors in the CPM laser and tried to control them.

6.2 Calibration of Dropout and Dropin

Our analysis of the dropout and dropin processes is based on a large amount of data we collect in various trigger and pump power settings. The data can be roughly divided into three types: dropout, dropin, and stable data. We also develop a C++ program, 2D-Correlation, to perform most of our analysis.

Our analysis shows that dropout events all have simple forms and they can be categorized into two groups by the dropout time: fast and slow dropouts, but the dropin events usually have complicated structures. Fig. 6.11 depicts a few typical dropout and dropin events. This difference confirmed the prediction by Andrews and Tracy's model of the CPM laser. Section 6.2.1 shows the calibration of the dropout and dropin processes.
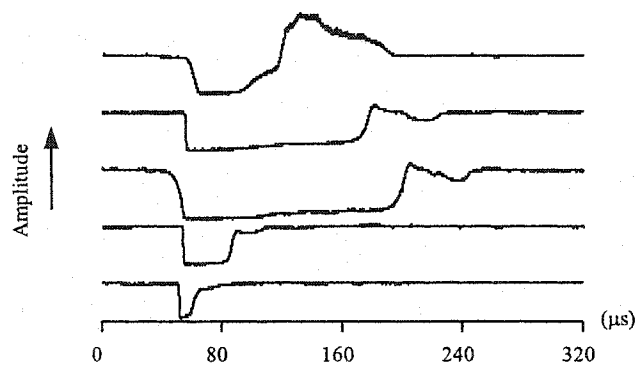
Figure 6.11: The curves plotted shows some typical dropout and dropin data. The curves are offset for clarity. The curves plotted use the amplitude data generated using the 16-point fitting process. The form of dropout events is much different from that of the dropin, which indicates different dynamics. The shortest dropout in above data is about 0.6 μs, the longest one is about 16 μs. But dropout events lasting as long as 0.16ms have been observed. The laser stays in no lasing mode for a while before it self-starts, which time varies from one data set to another. The dropin processes usually have complicated structures.

In the last section, Section 6.2.2, a thorough search of possible precursor before dropout events is carried out using statistical methods. But the result of the search is inconclusive.

6.2.1 The Dropout and Dropin

When a dropout happens, the laser's output power monotonically decreases in both beams. The power change in a dropout event has the form of a asymmetric hyperbolic tangent function. Since dropout events have very simple forms, we can describe a dropout using just a single time, which we called the dropout time. The dropout time, denoted as t_0,

describes the time it takes the output power drop from 90% to 10% of its normal level. The dropout is normally very short, about a few microseconds. But we observed dropout lasting as long as a few hundreds of microsecond. The dropout normally happens frequently, about 10 times per second in a stable mode-locking condition. But, sometimes, the laser can operated for $90 - 100$ seconds without dropout.

We processed more than a few hundred data series to obtain the distribution of dropout times. We used two ways to measure dropout times, which lead to almost identical results. Program 2D-Correlation carried out this calculation. The screen shots of the program show how the program makes the measurement as in Fig. 6.12.

The distribution of dropout time shows two distinct clusters: the fast and slow dropout group as shown in Fig. 6.13 (a). The data files used to generate the histogram were collected under the same experimental conditions except the pump power. The distribution of data series belonging to each pump power are also plotted in Fig. 6.13 (b).

The dropout in the CPM laser may be caused by disturbance in the dye jets such as small air bubbles or dust. But the fact that the rate of dropout occurrence increases dramatically when the parameters change indicates that external disturbances cannot account for all the dropout events. It is arguable that the fast dropout events may be caused by the disturbance in dye jets, because the presence of extra loss greatly reduces the Q value of the cavity and leads to a very fast power decreasing. But the origins of the two categories of dropout are still open questions.

Right after the dropout, there is a short time period during which no output power is detected. This time is denoted as t_s, which is the time that the CPM laser noise takes to initialize lasing action. When the pump power increases, t_s decreases. This effect is due
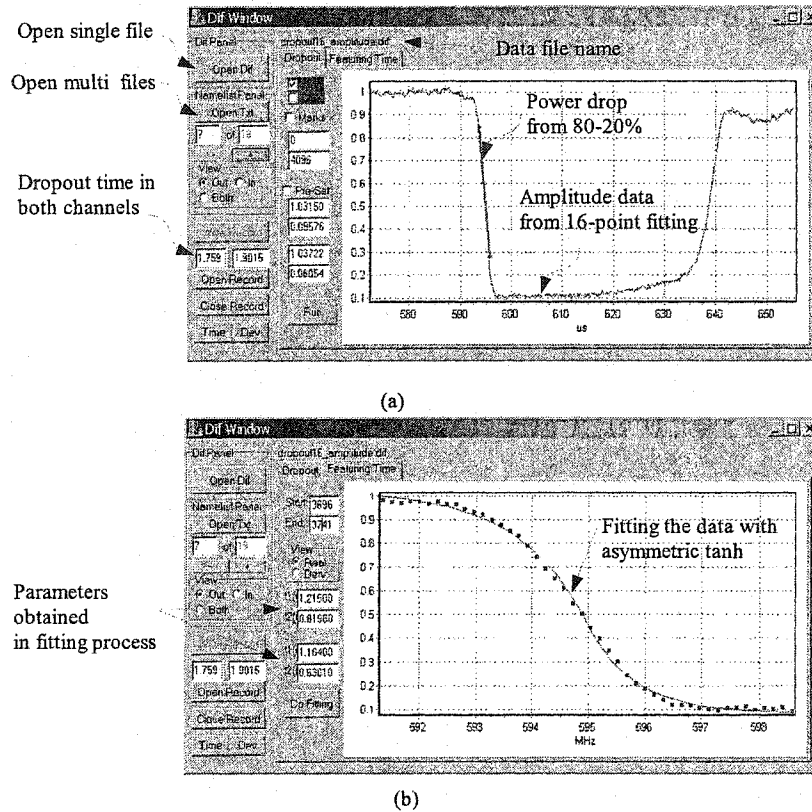
Figure 6.12: (a) The program measures the dropout times of multiple files in a batched way. The picture shows the measurement of the dropout time by measuring the time it takes the power to drop from 80% to 20% of its normal level. (b) The dropout time is also measured by fitting the data to an asymmetric tanh function with almost identical result (a).

to the fact that stronger spontaneous emission noise produced by a higher pump power is easier to evolve into ultrashort pulses. The correlation of t_s and the pump power is shown in Fig. 6.14. The correlation between t_s and t_o is also shown in Fig. 6.14.

A dropin process often shows very complicated patterns. The calibration of the dropin process, therefore, is difficult. A few typical patterns are plotted in Fig. 6.15.

During each self-starting process, the laser takes different paths. Sometimes, the laser starts without a CW pedestal in all pump power conditions, which has a shorter no-lasing period. In this type of dropin, the behavior of the laser is always similar to the pattern at
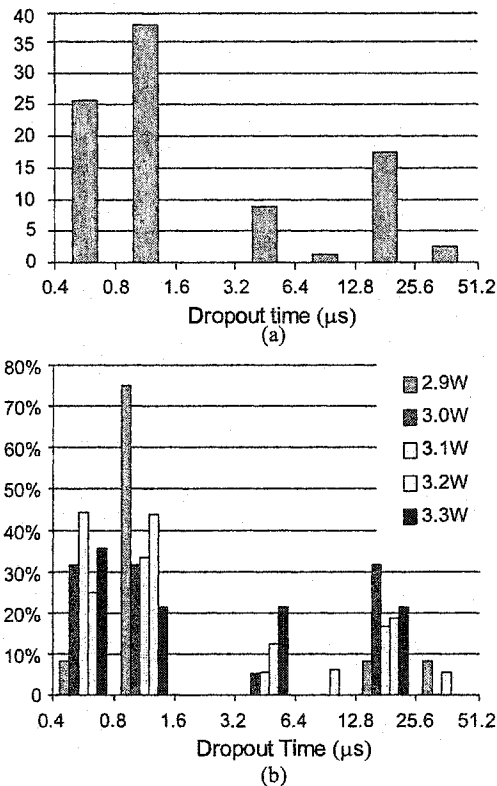
Figure 6.13: The distribution of dropout time shows a sharp peak around 1 μs and a relatively flat distribution at longer time with the bin size increased exponentially. (a) The distribution of dropout time from all the pump conditions. (b) The percentage distribution of dropout time under 5 different pump power conditions with around 20 data sets each.

bottom of Fig. 6.15. The pulsing is seeded by noise. The pulse power then increases by the end of the shallow dip, ultrashort pulse forms.

But as pump power increases, the pedestal appears more often. The pedestal is a metastable state. It evolves into a pulse very quickly. As the pump power increases, the life of the pedestal decreases. Other structures, like the sharp rising overshoot and dip, arise as well with an increase in pump power. The laser may have multiple overshot peaks and dips. The sharp rising edge before the first overshot peak has almost the same time constant under the same pump conditions, which can be used to estimate the time it takes
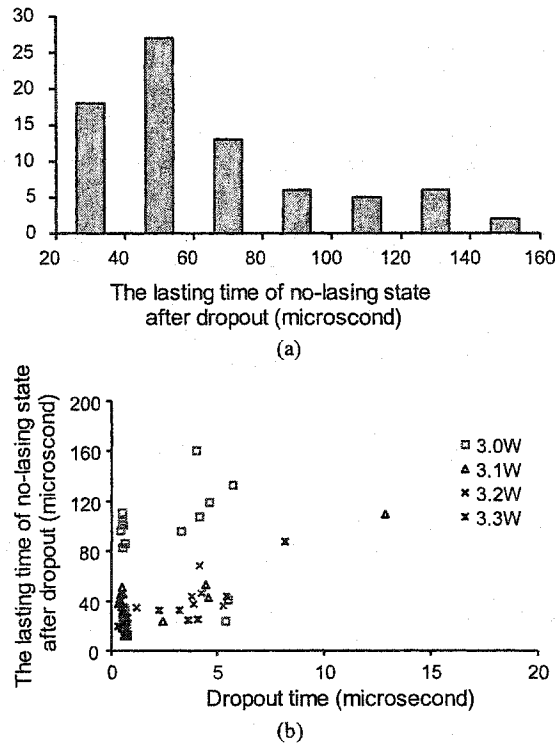
Figure 6.14: The histogram of no-lasing time after a dropout shows different pattern from that of the dropout time histogram. The no-lasing time tends to shrink with increasing of pump power. (a) The distribution of no-lasing time from all the pump conditions does not have two clusters. (b) There is no correlation between the lasting time of no-lasing state and different pump conditions.

a pulse to evolve from CW. At the peak, the pulse is still not very short which shows a lower SHG signal comparing to that produced by an ultrashort pulse. The pulses' duration between the overshot peak and the dip is unclear since the SHG signal varies little during this time. The ultrashort pulse forms at the end of the last dip. Our conjecture is that the pulse formation has two phases, the duration adjusting stage and the shape and phase adjusting stage. During the sharply rising time, the gain-windowing effect dominates and the pulse is shortened to a point that its phase becomes important. Then, the shape and phase adjustment comes into play, during which time the power drops a little to compensate for it.

Figure 6.15: . The dropin data shows similar patterns when the pump power is low (for example, the bottom 2 curves in (a)), but is abound of structures with high pump power. (a) The curve plotted at the bottom shows up under all pump conditions. The othe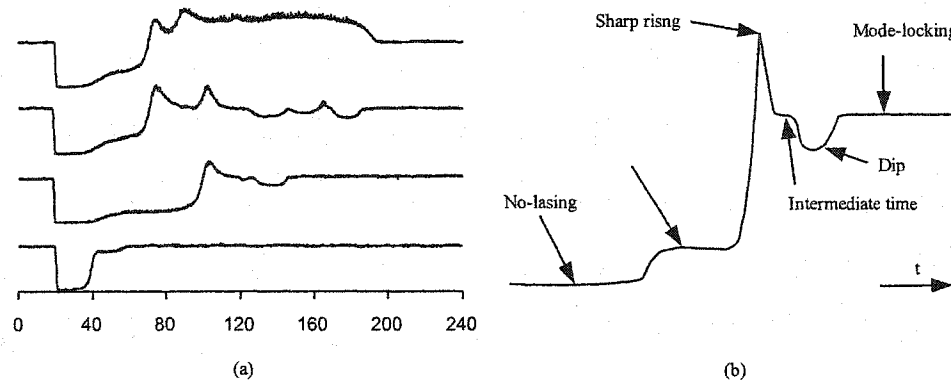r 3 appear in order when the pump power increases (from bottom up). (b) The diagram we use to characterize a typical dropin process.

Under even higher pump power conditions, the overshot peak relaxes to double pulse or CW due to the weakening of the absorber, and the dip disappears. In some other pump conditions, the laser eventually stabilizes in mode-locking state with the double pulse and CW modes are unstable. In case of exceeding pump power, the laser may stabilize in either of these two modes for a long time (more than a few seconds). In the double pulse case, both the pulse power and its SHG signal are greater than that in single pulse mode-locking case. In CW mode, the pulse power is greater but its SHG signal is smaller than the mode-locking case. Also, the spectrum is different between any two modes. So, it is easy to tell the mode of the CPM laser by observing the spectrum.

We proceeded to characterize the dropin by measuring the duration of the pedestal, the dropin time on the sharply rising edge, the FWHM of the peak, and the rising time of the dip. We omitted the intermediate time, which usually is hard to define and short. The amplitude of the pedestal is about the same under same pump power conditions, but it

increases slightly with time during one dropin event. It also increases with the pump level. It is intuitive that the pedestal's length shrinks in higher pump level. Since the seed has a higher energy, it is easier for the seed to evolve into a pulse.

The sharply rising edge can be calibrated by fitting the curve with a tanh function to obtain a time constant. Its rising time turns out to have no correlation with the dropout time. With the pump power increasing, its rising time becomes shorter. The FWHM of the peak is defined as the width at half height of the part of the peak above mode-locking power. This FWHM does not exist in some dropin data. It is correlated with the height of peak. Therefore when the pump power goes up, this FWHM increase slightly.

The rising time of the dip is the time that the SHG signal of the pulse rises to mode-locking level. It also shrinks as the pump power increases.

The measurement of above characteristics is plotted in Fig. 6.16. In general, the time it takes the CPM laser to dropin tends to shrink at a higher pump power, which is not a surprising result. But the dynamics of the dropin process can be very complicated to have multiple of these structure, which leads to a longer relaxation time before the laser stabilizes in a stable mode-locking state.

6.2.2   Precursor Search

The detection of precursors of dropout events is essential to the control of the CPM laser's dropout and dropin behaviors. Since no obvious precursor is observed in the CPM data series, we compared the statistical properties of the slow dropout, fast dropout, and stable data. We took the approach of searching for patterns allowing for physical interpretation rather than separating the data mathematically.
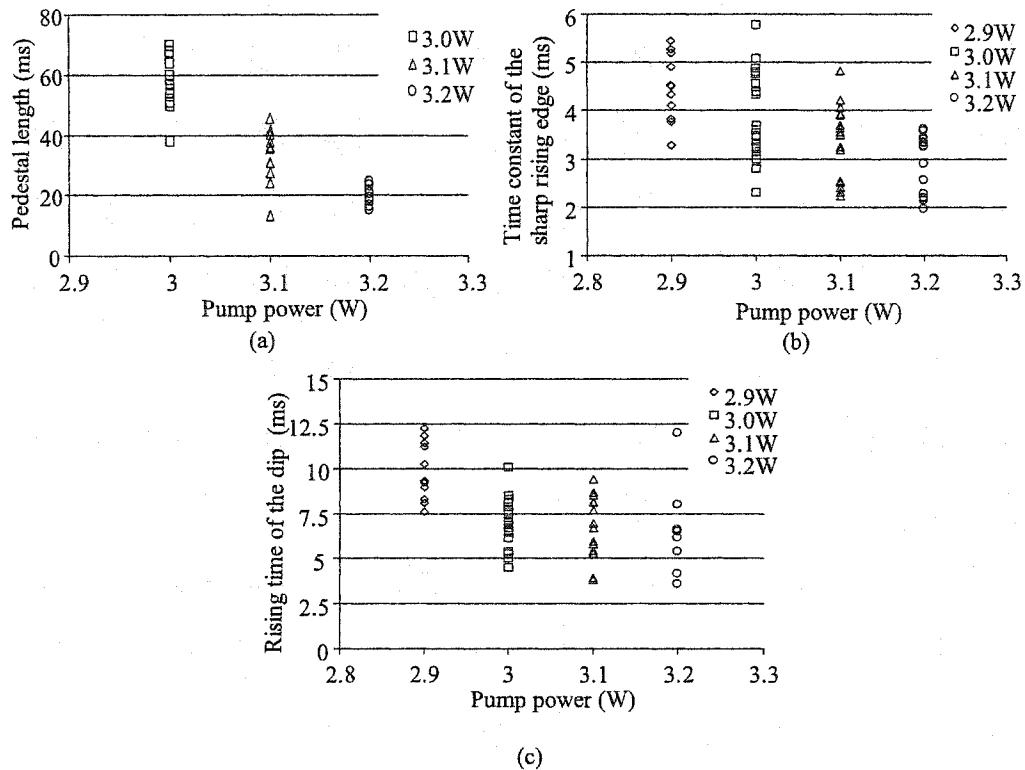
Figure 6.16: The measurement of some of the characteristics of a dropin process is made from about 90 data sets. Due to the variety of dropin processes, fewer than 90 points are actually obtained. (a) The distribution of the pedestal duration; (b) the distribution of the time constant of the sharp rising edge; (c) the distribution of the rising time of the dip.

The dropout data sets we used in the precursor searching were acquired by setting the trigger on dropout events. The stable data were acquired by software triggering the circuit. Since a dropout may happen right after the software trigger, only part of the stable data is valid. Therefore, we used only the fore half of the stable data and the data right before the dropout in the comparison. This finite data acquisition time limits our search range of the precursor to be within 0.32 ms before the dropout.

The comparison employs mainly two statistical methods: correlation and transfer entropy. These methods are also implemented by the software 2D-Correlation.

The correlation method includes auto-correlation of each channel and cross-correlation between two channels. The data in each channel is divided into windows with the same size. The auto-correlation calculates the correlation coefficient between one window and another window in the same channel with a delay, and the cross-correlation calculates the correlation coefficient between one window and another window in the other channel with a delay. For two data channels denoted as $x_i \in X$ (left channel) and $y_i \in Y$ (right channel), the auto-correlation and their cross-correlation coefficients are defined as

$$\rho_{X_i, X_j} = \frac{1}{n} \sum_0^{n-1} (x_i - \bar{X}_i)(x_j - \bar{X}_j)/\sigma_{X_i}\sigma_{X_j} \tag{6.6}$$

and

$$\rho_{X,Y} = \frac{1}{n} \sum_0^{n-1} (x_i - \bar{X})(y_i - \bar{Y})/\sigma_X\sigma_Y, \tag{6.7}$$

where $\bar{X}(\bar{Y})$ is the average value over n data points and $\sigma_{X(Y)}$ is the standard deviation

$$\sigma_{X(Y)}^2 = \frac{1}{n} \sum_0^{n-1} (x(y)_i - \bar{X}(\bar{Y}))^2. \tag{6.8}$$

The correlation coefficient shows the similarity of the two channels of data: strong correlation (=1), no correlation (near 0), or anti-correlation (=-1).

The 2D-correlation program presents the results obtained from the correlation method using 2-dimension bitmap pictures. As an example, the result of the cross-correlation between the left channel and the right channel is plotted in Fig. 6.17. The bitmap is generated with following parameters: the window size $n = 512$, shift steps of the window in the left channel is 30 points. These parameters will be used in the figures throughout this section.

Our analysis shows that in all three types of data the pictures generated using the auto-correlation and cross-correlation methods from the same file have similar patterns. This
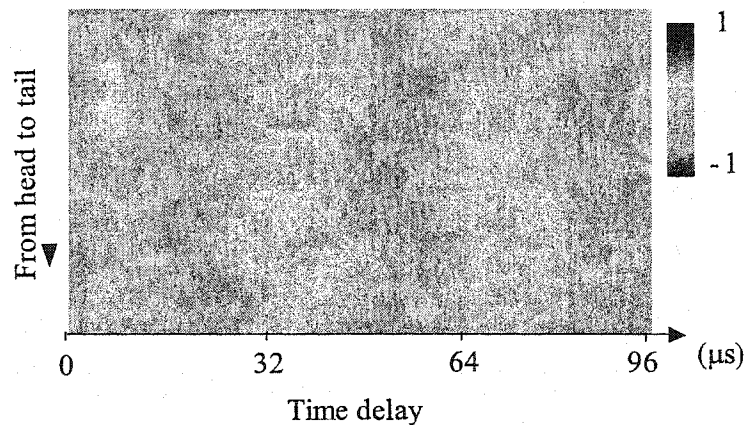
Figure 6.17: The bitmap picture shows color-coded correlation coefficients. This picture is generated by calculating the correlation coefficients between left channel data to delayed right channel data in a double pulse data file. The interchange of pulses power is shown by the vertical stripes. Each bit in the bitmap corresponds to one correlation coefficient with the color indicating its value. Along the X-axis, the bits are plotted with the window in the left channel fixed and varying the delay of the other window in the right channel. Along the Y-axis, the window in the left channel shifts from the beginning to the end of the file.

fact indicates the two beams of the CPM laser are always well correlated. The pictures generated from different types of data shows some differences as shown in Fig. 6.18. But, although a pattern may commonly exist in most of the files in one type of data, there are exceptions.

The transfer entropy uses symbolic data as input, i.e. $0s$ and $1s$, which allows for simple and fast calculation. The data must be symbolized before we can use them in transfer entropy method. We took the following approach to symbolize the data. First, we divided a time series into windows with the same size. Then, each data point was compared to the average of the points in the same window. Finally, the points above the average value are set to $1s$, otherwise, $0s$.

The transfer entropy is derived from the well-known mutual information method in
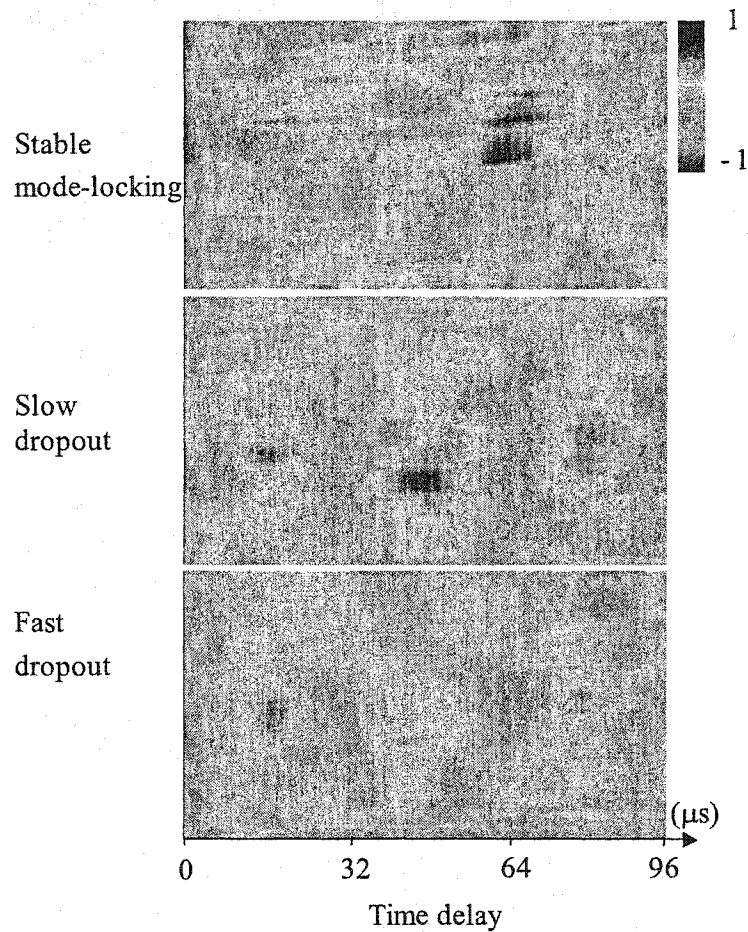
Figure 6.18: The pictures generated by cross-correlation method from different types of data shows some differences, but the patterns are not conclusive.

information theory to provide a measurement of dynamical or directional transfer of information [58]. The mutual information of two data sets $x \in X$ and $y \in Y$ produced by two processes is defined as

$$M_{XY} = \sum_{x,y} p(x,y) log \frac{p(x,y)}{p(x)p(y)}, \tag{6.9}$$

where the sum extends over all possible joint states of x and y. $p(x(y))$ and $p(x,y)$ are probability distribution of x (or y) and x,y. Since when the two processes are indepen-

dent, $p(x, y) = p(x)p(y)$, Eq. 6.9 shows the excessive information produced by the coupling between the two processes. The mutual information thereby measures the derivation of two processes from the independence presumption. The mutual information is zero when the two processes are actually independent. Otherwise it is positive. Note that M_{XY} is symmetric under the exchange of X and Y, therefore it does not contain any directional sense.

Transfer entropy from the right channel to the left
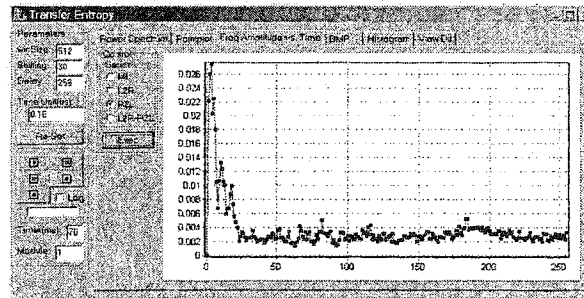
Transfer entropy from the left channel to the right
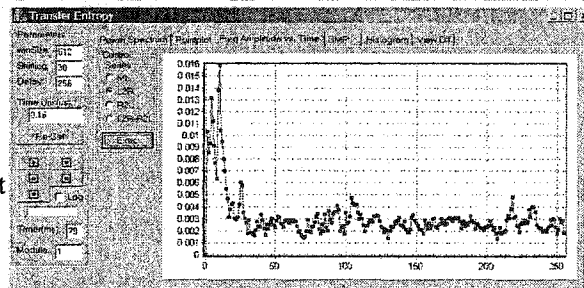
Difference of transfer entropy
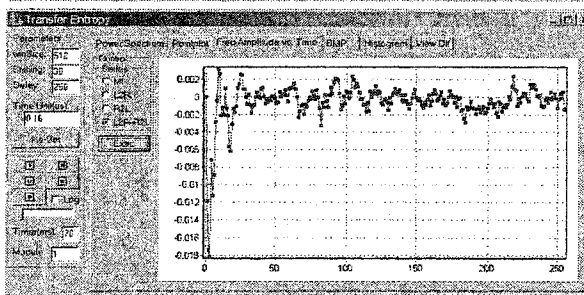
Figure 6.19: The transfer entropy curves show that the information flow between the two channels as a function of the delay time, which is denoted as points on the X-axis on each picture with a unit of 10 ns. The information flow is strong only when the delay time is very short. The structures around 1 μs are either the echo of the information flow or the side-band noise. The DTE indicates that the right channel is driving the left channel.

It is natural to give the mutual information a directional sense by computing the mutual information of two data sets produced by the same process at different time. For example, one can design a window sliding through data set X to make a series of data sets denoted as i with same length and a time delay $\tau \in 1, 2...N$. Then, the mutual information becomes

$$M_{X_i X_{i-\tau}} = \sum_{x_i, x_{i-\tau}} p(x_i, x_{i-\tau}) log \frac{p(x_i, x_{i-\tau})}{p(x_i)p(x_{i-\tau})}. \qquad (6.10)$$

$M_{X_i X_{i-\tau}}$ bears no influence of process Y. By including Y, one has

$$M_{X_i Y_i X_{i-\tau}} = \sum_{x_i, y_i, x_{i-\tau}} p(x_i, y_i, x_{i-\tau}) log \frac{p(x_i, y_i, x_{i-\tau})}{p(x_i, y_i)p(x_{i-\tau})}. \qquad (6.11)$$

The difference, $M_{X_i Y_i X_{i-\tau}} - M_{X_i X_{i-\tau}}$, shows the derivation of two processes from the independent presumption. The derivation is a measurement of information flow introduced by process Y, i.e., the way Y drives X. The transfer entropy from Y to X then is defined as

$$T_{Y-X} = M_{X_i Y_i X_{i-\tau}} - M_{X_i X_{i-\tau}} = \sum_{x_i, y_i, x_{i-\tau}} p(x_i, y_i, x_{i-\tau}) log \frac{p(x_i, y_i, x_{i-\tau})p(x_i)}{p(x_i, y_i)p(x_i, x_{i-\tau})}. \qquad (6.12)$$

The transfer entropy of X to Y can also be defined likewise. Now, T_{Y-X} is no longer symmetric, but rather measures the dependence of X on Y. Similar to mutual information, transfer entropy is zero when the two processes are independent and positive otherwise.

The difference between two counter-directional transfer entropies is also useful, which shows if one channel is driving the other one,

$$D_{X,Y} = T_{Y-X} - T_{X-Y}. \qquad (6.13)$$

Fig. 6.19 shows the transfer entropy study of a dropout data file using our 2D-Correlation program. In Fig. 6.19, each transfer entropy curve is obtained by averaging the information
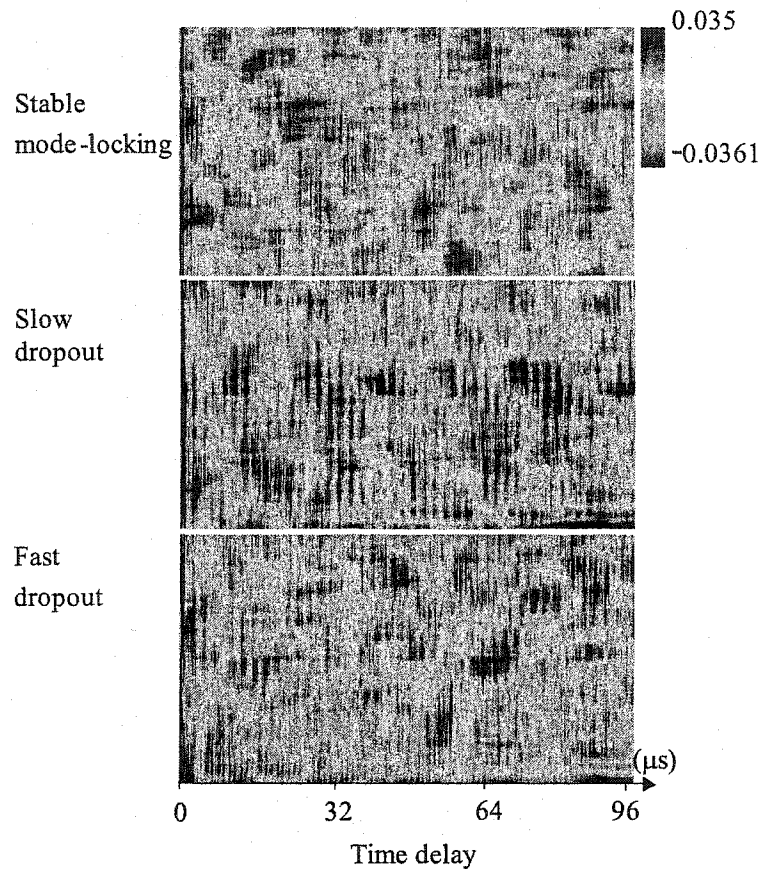
Figure 6.20: The bitmap picture shows the DTE values, left to right channel information flow, generated using the same data used in Fig. 6.18. The values plotted is in the same way as that in Fig. 6.18. A close look reveals that it shows similar patterns as that in Fig. 6.18, but due to the small variation of DTE values, they are not so clear. The different patterns we found in the three types of data are also not consistent with all the data sets.

flow from all the windows from one channel to their corresponding delayed windows in the other channel. Fig. 6.20 shows a plot similar to Fig. 6.18 comparing the DTE between three types of data. These bitmaps uses the same files used in Fig. 6.18. But, since the DTE is always very small, it is a little hard to find patterns in Fig. 6.20.

In summary, we have not found the precursor for dropouts in the CPM laser. Though we observe some patterns suggesting there may be precursors, our observation is not conclusive.

It requires further statistical and experimental study to determine if the precursor exists

and the possible form for it.

Chapter 7

Conclusions and Future Work

The versatile operation characteristics of CPM laser brings up interesting dynamical problems such as the forms of the transitions between its three modes, the dynamics governing its transient behaviors, the control of its transient behaviors.

In this thesis, we studied the CPM laser's operation in detail. By optimizing the CPM laser's stable mode-locking operation, we observed and calibrated the forms of dropout and dropin behaviors in the CPM laser. A dropout process always has a very simple asymmetric tanh form, whereas a dropin sometimes has complicated structures. Andrews and Tracy's theoretical study is suggestive of this difference between the dropout and the dropin behaviors we observed. The two-cluster distribution of the dropout time suggests the fast and slow dropout may have different physical origins.

Aiming at control the dropout behavior of the CPM laser, we carried out a thorough search for possible precursors before dropout events using various statistical tools. Though our searching implies subtle differences between the stable mode-locking data and the dropout data, they are not conclusive when we use them to predict if the laser is going to dropout. Further study will require higher accuracy in experiment and more powerful statistical tools.

Due to its many adjustable parameters, the CPM laser provides us a unique tool to study the ultrafast pulse generation and ultrafast laser dynamics. Realizing the limitation of previous models of ultrafast lasers in including various pulse shapes and allowing for dynamics study, we developed a bistable medium model for ultrafast lasers. This model allows us to intuitively relate the pulse generation process to physical parameters in a system and answer the question of what properties a system needs to produce pulses with selected shapes. This feature of the bistable medium model is instructive to the design of ultrafast systems and pulse shaping in those systems. The bistable medium also has a very simple form allowing for studying of higher order dispersion effects and dynamics in ultrafast lasers, which would be a natural step in future work.

Appendix A

Numerical Calculation of

Prism-pair Dispersion

Fig. A.1 shows the configuration of a four-prism dispersion control device. The two parallel rays, $R1$ and $R2$, shown in Fig. A.1 are two arbitrary rays within the laser beam. The rays disperse after passing through the first prism. After passing through the second prism, the rays gain some width and are in parallel with the input rays. The following two prisms recombine the different frequency components. The output rays will be in parallel with the input if the prisms are well aligned. The transversal surface M, M' denotes that the second pair of prisms should be positioned on the mirror image of the first pair.

The x-y coordinates are set up as in Fig. A.1 to calculate the length of the optical path through the first pair of prism. Since the other half optical path is identical, we will calculate only this half and add a factor of two to it afterward. Then we can find out the phase delay function for different frequency components.

The coordinates are set up in a way that the baselines of the prisms are parallel with the x-axis. The first prism's position can then be described by it vertex's coordinates, $P1(P1_x, P1_y)$. In experiment, the distance between the vertexes of two prisms, shown as L

127
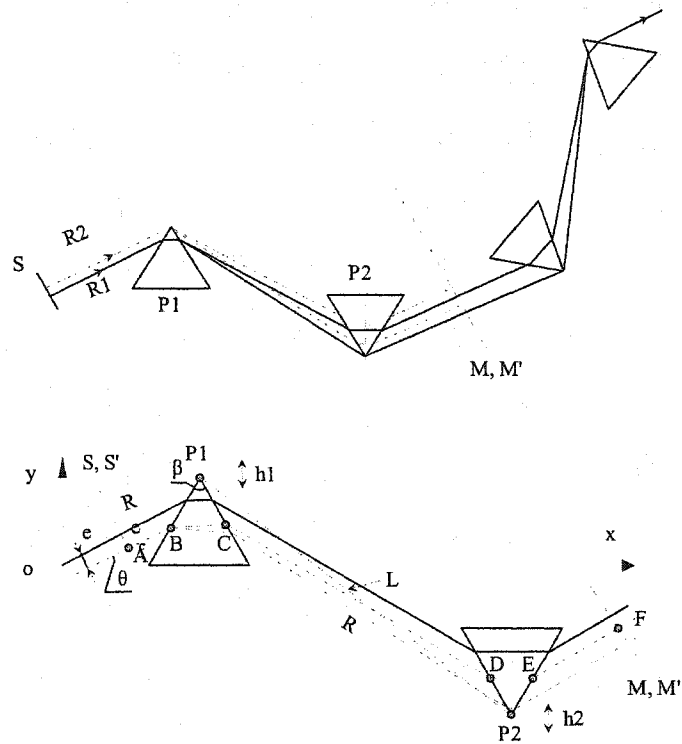
Figure A.1: Prism sequence used in the CPM laser to introduce variable GVD. The bottom diagram shows the optical path that our calculation is based on.

in the bottom diagram in Fig. A.1, is conventionally used to describe the prism pair device. So, we use L as one constraint to initially place the second prism, $P2(P2_x, P2_y)$, relative to the first one. The other constraint is that the second prism must intercept the whole dispersed laser beam. This gives us a range of possible choices. In practice, the laser beam is arranged to pass the second prism near its apex to minimize the path in glass to avoid material dispersion. In our calculation, the prisms are allowed to translate in y direction, therefore, any possible position for $P2$ is good to use. Then, we can describe the surfaces of the two prisms with a set of linear equations.

The incident laser beam can also be described by a set of linear equations. The bottom

diagram in Fig. A.1 illustrates an arbitrary ray R, which is apart from the middle of laser beam by a distance e. The optical path for R is the distance between the surfaces S, S' and M, M', both of which are transversal to the laser beam. The incident angle of the laser beam on the first prism is around the Brewster angle, α, of the glass. The optical path varies with the frequency of the light, therefore the optical path of ray R with frequency ω can be written as,

$$R(e, \theta, \omega) = \overline{AB} + \overline{BC} + \overline{CD} + \overline{DE} + \overline{EF}, \qquad (A.1)$$

where θ is the angle between R and x-axis. Each piece of distance in Eq. A.1 can be calculated by solving for the coordinates of the points in sequence. The overall optical path can then be converted into the phase function of the prism sequence. As we can see, the phase function have four variables: wavelength, prism translation ($h1$ and $h2$), peak-to-peak distance L, and incident angle θ.

Following is the Maple script in which the calculation is carried out.

```
> restart; theta[0]:= T+arcsin(n_0*sin(beta/2))-beta/2:
(Description of parameters:)
  T is the tilt angle deviation from minimum deviation
  s is the wavelength in micron
  h is the offset of the prism from zero net GVD
  w is the offset across the beam
  L is the distance between prisms
  Distances are in mm
> T:=0.000;
```

```
n_0:=1.457:

dn:=-0.03109:

d2n:= +0.1267:

d3n:=-.1492436864*6:

d4n:=.3157242844*24:

n:= n_0+dn*s+(d2n/2)*s^2+(d3n/6)*s^3+(d4n/24)*s^4;

px[1]:=100:

py[1]:=32.23+h:

k:=5:

beta:=Pi/3:

x[0]:=-w*evalf(sin(theta[0])):

y[0]:=w*evalf(cos(theta[0])):

px[2]:=px[1]+L*evalf(cos(theta[0])):

py[2]:=29-evalf(L*sin(theta[0])):

n_g:=simplify(n-(s+0.620)*diff(n,s));
```

(Output:)

```
    T := 0

    n := 1.457 - .03109 s + .06335000000 s^2 - .1492436864 s^3

        + .3157242844 s^4

    n_g := 1.476275800 - .07855400000 s + .2142432567 s^2

        - .4845088528 s^3 - .9471728536 s^4
```

(Solve for the function of beam and intersections)

```
> sols1:=solve({y-y[0]=(x-x[0])*tan(theta[0]),

       y-py[1]=(x-px[1])/tan(beta/2)},{x,y}):

  x[1]:=subs(sols1,x):

  y[1]:=subs(sols1,y):

  theta[1]:=series(arcsin(sin(theta[0]+beta/2)/n)-beta/2,s,k):

> sols2:=solve({y-y[1]=(x-x[1])*tan(theta[1]),

       y-py[1]=(px[1]-x)/tan(beta/2)},{x,y}):

  x[2]:=subs(sols2,x):

  y[2]:=subs(sols2,y):

  theta[2]:=series(arcsin(n*sin(beta/2-theta[1]))-beta/2,s,k):

> sols3:=solve({y-y[2]=(x[2]-x)*tan(theta[2]),

       y-py[2]=(px[2]-x)/tan(beta/2)},{x,y}):

  x[3]:=subs(sols3,x):

  y[3]:=subs(sols3,y):

  theta[3]:=series(arcsin(sin(theta[2]+beta/2)/n)-beta/2,s,k):

> sols4:=solve({y-y[3]=(x-x[3])*tan(theta[3]),

       y-py[2]=(x-px[2])/tan(beta/2)},{x,y}):

  x[4]:=subs(sols4,x):

  y[4]:=subs(sols4,y):

  theta[4]:=series(arcsin(n*sin(beta/2-theta[3]))-beta/2,s,k):

> sols5:=solve({y-y[4]=(x-x[4])*tan(theta[4]),

       y-py[2]-.01*L=-(x-px[2]-.01*L)/tan(theta[4])},{x,y}):

  x[5]:=subs(sols5,x):
```

```
y[5]:=subs(sols5,y):
```

(Calculate optical path in vacuum)

```
> P1:=convert(series(sqrt((x[1]-x[0])^2+(y[1]-y[0])^2),s,k),polynom):

  P2:=convert(series(sqrt((x[3]-x[2])^2+(y[3]-y[2])^2),s,k),polynom):

  P3:=convert(series(sqrt((x[5]-x[4])^2+(y[5]-y[4])^2),s,k),polynom):

  Q1:=convert(series(n_g*sqrt((x[2]-x[1])^2+(y[2]-y[1])^2),s,k),polynom):

  Q2:=convert(series(n_g*sqrt((x[4]-x[3])^2+(y[4]-y[3])^2),s,k),polynom):
```

(Calculate the repetition rate shift as a function of wavelength

and prism depth in the beam. The zero depth repetition rate used

is 95 MHz.)

```
>  A:=280:

> 'KHz_Shift'=subs(w=0,collect(convert(series(convert(series(subs(L=A,

  (P1+P2+P3+Q1+Q2)*30.05),w,3),polynom),h,4),polynom),s));
```

(output:)

```
KHz_Shift(h) = s^4 (-38.22527225 h - 866.2050781 -

        .8559931037e-8 h^2 + .1408726036e-8 h^3)

    + s^3 (163.326938 - 20.83222009 h + .2147106401e-9 h^2

        -.2238973701e-9 h^3)

    + s^2 (-.2846869069e-9 h^3 + 9.118950939 h +

        .5915791554e-9 h^2 - 28.2998026)

    + s (.1330892684e-9 h^3 - 3.321685638 h
```

```
        - .3755752479e-9 h^2 +  .28434e-2)

    + (11706.06969 + 18.14105881 h -  .1423352502e-10 h^2

      -.2674826052e - 12 h^3)
```

(Calculate phase function as w*t)

```
> 'Phase_Function'=subs(w=0,collect(convert(series(convert(series(subs

  (L=A,(P1+P2+P3+Q1+Q2)*10.1),w,3),polynom),h,4),polynom),s));
```

(Output:)

```
    Phase_Function = s^4 (-12.84776206 h - 291.1371467

        - .2877048369e-8 h^2 + .4734819623e-9 h^3)

    + s^3 (54.8952439 - 7.001844354 h

      + .7216563945e-10 h^2 - .7525335902e-10 h^3)

    + s^2 (-.9568511683e-10 h^3 + 3.064938584 h

      + .1988335929e-9 h^2 - 9.5117475)

    + s (.4473216674e-10 h^3 - 1.116440098 h

      -.1262332780e-9 h^2 + .9556e-3)

    + (3934.485986 + 6.09732758 h

      - .4783980124e-11 h^2-.8990263936e-13 h^3)
```

(This piece of code is used to visualize the calculated optical

path. The output is omitted.)

```
> h:=0: w:=0: theta[1]:=convert(theta[1],polynom): theta[2]:=

  convert(theta[2],polynom): theta[3]:=convert(theta[3],polynom):

  theta[4]:=convert(theta[4],polynom):
```

```
> x[2]:=convert(x[2],polynom): y[2]:=convert(y[2],polynom):

    x[3]:=convert(x[3],polynom): y[3]:=convert(y[3],polynom):

    x[4]:=convert(x[4],polynom): y[4]:=convert(y[4],polynom):

    x[5]:=convert(x[5],polynom): y[5]:=convert(y[5],polynom):

> L:=A; s:=0: C1:=CURVES([[x[0],y[0]],[x[1],y[1]],[x[2],y[2]],

    [x[3],y[3]],[x[4],y[4]],[x[5],y[5]]],COLOR(HUE,0.3)):

    s:=0.05: C2:=CURVES([[x[0],y[0]],[x[1],y[1]],[x[2],y[2]],

    [x[3],y[3]],[x[4],y[4]],[x[5],y[5]]],COLOR(HUE,0.8)):

    s:=-0.05: C3:=CURVES([[x[0],y[0]],[x[1],y[1]],[x[2],

    y[2]],[x[3],y[3]],[x[4],y[4]],[x[5],y[5]]],COLOR(HUE,0.1)):

    PLOT(C1,C2,C3,POLYGONS([[evalf(px[1]-py[1]*tan(beta/2)),0],

    [px[1],py[1]],[evalf(px[1]+py[1]*tan(beta/2)),0]]),

    POLYGONS([[evalf(px[2]-py[1]*tan(beta/2)),py[1]+py[2]],

    [px[2],py[2]],[evalf(px[2]+py[1]*tan(beta/2)),py[1]+

    py[2]]]),COLOR(HUE,0.5));
```

Appendix B

Formulating of Master Equation

In this appendix, we will summarize a theoretical treatment of a mode-locked laser using an active mode-locked laser as an example to demonstrate the formulating process of the master equations for ultrafast lasers. Active mode-locking can be achieved simply by inserting an optical modulator to modulate the loss. The periodical modulating action is driven by an external source. If the modulation frequency is precisely equal to the frequency interval between adjacent modes, for each mode, side bands are generated with frequencies coinciding with the frequencies of neighboring modes. This coupling process will gradually synchronize the modes during mode-locking process.
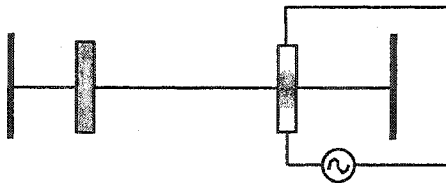

Figure B.1: The diagram of an active mode-locked cavity.

Fig. B.1 sketches such an active mode-locked laser, which consists of a Fabry-Perot cavity, a gain medium, and a modulator. While traveling in the cavity, the pulse undergoes loss, gain, and modulation. The loss in a laser cavity arises from a variety of sources such

135

as the output coupler and optical surfaces. These losses are linear to the field, which can be lumped into a single parameter l. When the pulse travels through the cavity once, its amplitude, ρ, is multiplied by $(1 - l)$. Similarly, the gain causes the pulse amplitude to be multiplied by $1 + g$ after each round trip. Note that the gain is a function of frequency which indicates the gain's bandwidth limitation. The gain profile can be modeled using a Lorentzian shape without losing generality. The gain for the nth Fourier component ρ_n is written as

$$g(n) = \left[1 + \frac{g_0}{1 + (n\Delta\omega)^2/\Omega_g^2}\right], \tag{B.1}$$

where Ω_g is the bandwidth of the gain. Here the spectrum is centered at ω_0 where $n = 0$.

Eq. B.1 can be expanded to the first order as

$$g(n) \simeq 1 + g_0 \left[1 - (n\Delta\omega)^2/\Omega_g^2\right], \tag{B.2}$$

when $n\Delta\omega << \Omega_g$. The influence of the modulator is assumed to be a sinusoidal loss, $M[1 - cos(\Delta\omega t)]$, where M is the modulation depth. For any frequency component, the modulation causes the generation of two side bands,

$$M[1 - cos(\Delta\omega t)]\rho_n e^{i(\omega_0 + n\Delta\omega)t} = -M\rho_n e^{i\omega_0 t}\left[\frac{1}{2}e^{i(n-1)\Delta\omega t} - e^{in\Delta\omega t} + \frac{1}{2}e^{i(n+1)\Delta\omega t}\right]. \tag{B.3}$$

Here the phase is assumed to be exactly the same for all frequency components. From here on the carrier frequency can be dropped, according to Eq. B.3.

In steady state, the pulse replicates itself in each round trip, so does its frequency components. And it can be described by collecting all the terms that belong to frequency

component ρ_n into one equation,

$$\Delta\rho_n = g_0 \left[1 - \frac{(n\Delta\omega)^2}{\Omega_g^2} \right] \rho_n - l\rho_n + \frac{1}{2}(\rho_{n+1} - 2\rho_n + \rho_{n-1}) = 0. \qquad (B.4)$$

When the frequency spacing between neighboring modes are small comparing with the spectrum range, the equation can be further simplified by replacing the last term in Eq. B.4 with a second order derivative,

$$\left[g_0 \left(1 - \frac{(\omega)^2}{\Omega_g^2} \right) - l + \frac{M\Delta\omega^2}{2} \frac{d^2}{d\omega^2} \right] \rho(\omega) = 0. \qquad (B.5)$$

Here a continuous function of $\rho(\omega)$ is used to replace ρ_n. The solution to this equation is Hermite Gaussian,

$$\rho(\omega) = H_\nu(\omega\tau)e^{-\omega^2\tau^2/2}, \qquad (B.6)$$

with the constrains

$$\frac{1}{\tau^4} = \frac{M\Delta\omega^2\Omega_g^2}{2g_0} \qquad (B.7)$$

and

$$g - l = M\Delta\omega^2\tau^2(\nu + \frac{1}{2}). \qquad (B.8)$$

When a mode-locked laser is in a free running state, the loss equals to the gain in one round trip, but smaller than small signal gain which is required for self-starting action. Eq. B.8 shows that the peak gain is greater than the loss now, which is needed to balance the nonlinear loss suffered by the wings of the pulse. For the same reason, higher order Hermite Gaussian pulses suffer more loss than the Gaussian pulse. Therefore, only the Gaussian pulse is the stable solution to Eq. B.5.

The Fourier transform of the first order of Hermite Guassian pulse, Eq. B.6, is a Gausian pulse in the time domain,

$$\rho(t) = \frac{\sqrt{2\pi}}{\tau} A e^{-t^2/\tau^2}, \tag{B.9}$$

where, A is a constant describing the amplitude, and τ is the pulse width.

The pulse width τ in Eq. B.7 is limited by the gain bandwidth and the modulation depth. Although Eq. B.7 is instructive to the mode-locking technique, in practice, it is quite limited. In building practical active mode-locked systems, the match of the repetition rate and modulation frequency is difficult. In a linear cavity, the problem becomes further complicated by the requirement of precise positioning of the modulator.

The time domain master equation governing the mode-locking process can be deduced from Eq. B.5 by the Fourier transform as

$$\left[g_0 \left(1 + \frac{1}{\Omega_g^2} \frac{d^2}{dt^2} \right) - l - \frac{M}{2} \Delta\omega^2 t^2 \right] \rho(t) = 0. \tag{B.10}$$

Eq. B.10 shows the nonlinearity of gain which changes according to the second derivative of its profile. Unfortunately, this equation describes one single pulse because of the assumption that the spectrum is continuous, which limits its ability to describe the gain windowing effect and the pulse evolution.

The master equations Eq. B.9 and B.6 provide an insightful analytic way of explaining the mode-locking mechanism. By replacing the terms in Eq. B.9 and B.6 with corresponding function forms and including dispersion, these master equations can be used in modeling passive mode-locked lasers.
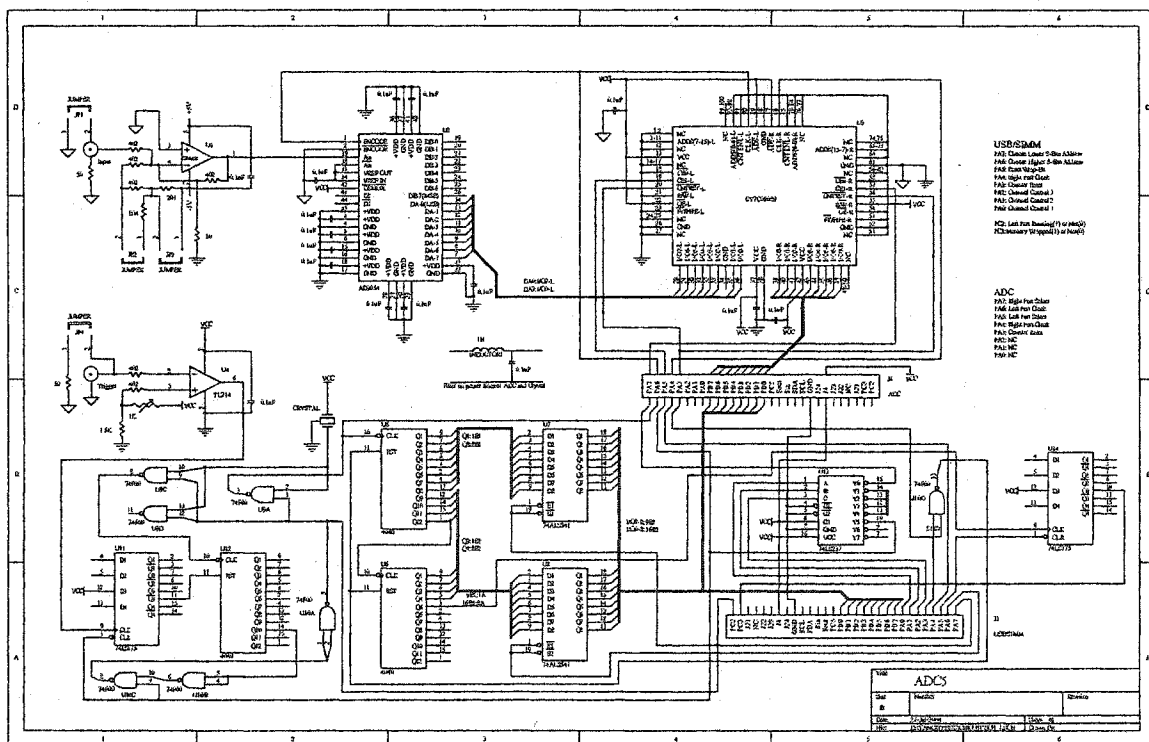
Appendix C

ADC5's Circuit Diagram

Figure C.1: The circuit diagram of ADC5.

139

	Command	P C		P A								PB
		3	2	7	6	5	4	3	2	1	0	ALL
1	Stop Data Collecting	R	x	1	1	1	0	1	1	1	1	x
2	Reset Left Port Counter	x	x	1	1	1	0	0	1	0	1	x
3	Start Data Collecting	x	R	1	1	1	0	1	1	0	1	x
4	Read Outer Counter Address Bit0-7	x	x	0	1	1	0	1	1	1	1	R
5	Read Outer Counter Address Bit8-15	x	x	1	0	1	0	1	1	1	1	R
6	Trigger and Counter Reset	x	x	1	1	0	0	0	1	1	1	x
7	Reset Address in Channel 1	x	x	1	1	1	0	0	0	0	0	x
8	Read Data from Channel 1(First Part)	x	x	1	1	1	0	1	0	0	0	R
9	Read Data from Channel 1(Second Part)	x	x	1	1	1	1	1	0	0	0	R
10	Reset Address in Channel 2	x	x	1	1	1	0	0	0	0	1	x
11	Read Data from Channel 2(First Part)	x	x	1	1	1	0	1	0	0	1	R
12	Read Data from Channel 2(Second Part)	x	x	1	1	1	1	1	0	0	1	R
13	Reset Address in Channel 3	x	x	1	1	1	0	0	0	1	0	x
14	Read Data from Channel 3(First Part)	x	x	1	1	1	0	1	0	1	0	R
15	Read Data from Channel 3(Second Part)	x	x	1	1	1	1	1	0	1	0	R
16	Reset Address in Channel 4	x	x	1	1	1	0	0	0	1	1	x
17	Read Data from Channel 4(First Part)	x	x	1	1	1	0	1	0	1	1	R
18	Read Data from Channel 4(Second Part)	x	x	1	1	1	1	1	0	1	1	R
19	Reset Address in Channel 5	x	x	1	1	1	0	0	1	0	0	x
20	Read Data from Channel 5(First Part)	x	x	1	1	1	0	1	1	0	0	R
21	Read Data from Channel 5(Second Part)	x	x	1	1	1	1	1	1	0	0	R

Figure C.2: The commands executed by ADC5 sending from the USB/SIMM board.

Appendix D

Key Functions in USB Programs

This appendix includes the key function in the GUI program and the framework programs.

In GUI program, the following procedures open a device, send vendor requests and close the device.

```
... HANDLE hDevice; // handle to the device

char * pcDriverName =  "Ezusb-0";

...

//issue a handler to device

if (bOpenDriver (&hDevice, pcDriverName) != TRUE){

    hDevice = NULL;

    MessageBox(NULL,"Error!","Could not open driver",MB_OK);

    }


if (hDevice != NULL){

    //Prepare for windows call to device

    //Transfer Direction (zero=host->device, one=d->h)
```

141

```
TakeData.direction = 0;

//Request Type (1=class, 2=vendor)

TakeData.requestType = 2;

//recipient (0=device,1=interface,2=endpoint,3=other)

.....

// Here is the Windows Call to a vendor request.

TakeData.request=0xb0;

bResult = DeviceIoControl (hDevice,

    IOCTL_EZUSB_VENDOR_OR_CLASS_REQUEST,

    &TakeData,

    sizeof (VENDOR_OR_CLASS_REQUEST_CONTROL),

    NULL,

    NULL,

    (unsigned long *)&nBytes,

    NULL);

// error check vendor request

if (bResult == FALSE) {

    MessageBox(NULL,"Error!","Could not send reset",MB_OK);

    if(!CloseHandle (hDevice))  // close device

        MessageBox(NULL,"Error!","Could not close driver",MB_OK);

        return;

        } //if

}//if
```

```
CloseHandle (hDevice); ...
```

The following procedures are executed to initialize the USB device on the plugging in of the USB device. They also receive and execute vendor request calls from the host computer.

```
...

//user-defined functions

#define VR_STOP 0xb0 // Stop the ADC5 board from collecting data

#define VR_ENABLE 0xb1 // Enable the ADC5 board to collect data

#define VR_READDATA 0xb2 // Read data from 1 channel of 5 channels

#define VR_READ_ADDRESS 0xb3 // Read outer counter address

                            // and other status flags ...


...

//initializing the USB device

void TD_Init(void) // Called once at startup {

    DataREQ = FALSE;

    Trigger_Bit_Set = 0x00;

        Enable_Bit_Set = 0x00;

    Counter_Wrap_Bit_Set = 0x00;


    Rwuen = TRUE; // Enable remote-wakeup

    EZUSB_InitI2C(); // Initialize I2C Bus

    // Configure IO endpoints
```

```
    INO7VAL |= bmEP2;

    OUTO7VAL |= bmEP2;

    PORTACFG = 0x00;

    PORTBCFG = 0x00;

    PORTCCFG = 0xC0;

    OEA = 0xFB;   // A0,1,3-7 as OUT, A2 as IN

    OEB = 0x00;   // B as IN

    OEC &= ~bmBIT3|~bmBIT2;   // C2 and C3 as IN

} ...



... void TD_Poll(void) // Called repeatedly while the device is

idle {

    ...

} ...



...

// implementation of user-defined functions call via vendor request

BOOL DR_VendorCmnd(void) {

    ...

    // direct vendor request to functions' entries

    switch(SETUPDAT[1])

    {

        case VR_STOP:
```

```
            OUTA = 0xE0;

        break;

    case VR_ENABLE:

            . . . .

        . . .

    }

    . . .

} . . . .
```

Bibliography

[1] A. N. Buijserd and H. B. van Linden van den Heuvell, Measurement in Science and Technology **1**, 751 (1990).

[2] S. L. Shapiro, *Ultrashort Laser Pulses:picosecond techniques and applications* (Springer-Verlag, Berlin Heidelberg, New York, 1977).

[3] L. E. Gargrove, R. L. Fork, and M. A. Pollack, Applied Physics Letters **5**, 4 (1964).

[4] E. P. Ippen, C. V. Shank, and A. Dienes, Applied Physics Letters **21**, 348 (1972).

[5] D. E. Spence, P. N. Kean, and W. Sibbett, Optics Letters **16**, 42 (1991).

[6] J. Herrmann and B. Wilhelmi, *Lasers for Ultrashort Light Pulses* (North-Holland, 1987).

[7] C. Hirlimann, Pulsed optics, in *Femtosecond Laser Pulses*, edited by C. Rulliere, pp. 25–52, New York, 1998, Springer-Verlag, Berlin and Heidelburg.

[8] J.-C. Diels, *Ultrashort Laser Pulse Phenomena: Fundamentals, Techniques, and Applications on a Femtosecond Time Scale* (Academic Press, Inc, San Diego, CA, 1996).

[9] I. Walmsley, L. Waxer, and C. Dorrer, Review of Scientific Instruments **72**, 1 (2001).

[10] E. P. Ippen and C. V. Shank, Techniques for measurement, in *Topics in Applied Physics , Vol. 18: Ultrashort Light Pulses: Picosecond Techniques and Applications*, edited by S. L. Shapiro, pp. 25–52, Berlin Heidelberg New York, 1977, Springer-Verlag, Berlin and Heidelburg.

[11] D. J. Kane and R. Trebino, IEEE Journal of Quantum Electronics **29**, 571 (1993).

[12] D. J. Kane, IEEE Journal of Quantum Electronics **35**, 421 (1999).

[13] C. Iaconis and I. A. Walmsley, Optics Letters **23**, 792 (1998).

[14] W. J. Walecki, D. N. Fittinghoff, A. L. Smirl, and R. Trebino, Optics Letters **22**, 81 (2001).

[15] A. Laubereau, Optical nonlinearities with ultrashort pulses, in *Topics in Applied Physics , Vol. 60: Ultrashort Laser Pulses: Generation and Applications, Sec. Ed.*, edited by S. L. Shapiro, p. 57, Berlin Heidelberg New York, 1993, Springer-Verlag, Berlin and Heidelburg.

[16] W. Kaiser, *Topics in applied physics, v60, Ultrashort laser pulses generation and applications, ed. W. Kaiser* (Springee-Verlag, New York, 1993).

[17] M. Nisoli *et al.*, Optics Letters **22**, 522 (1997).

[18] P. P. Sorokin and J. R. Lankard, IBM Journal of Research and Development **10**, 162 (1966).

[19] W. Schmidt and F. P. Schäfer, Physics Letters **26A**, 558 (1968).

[20] J. P. Letouzey and S. O. Sari, Applied Physics Letters **23**, 311 (1973).

[21] C. V. Shank and E. P. Ippen, Applied Physics Letters **24**, 373 (1974).

[22] G. H. C. New, Journal of Applied Physics **47**, 3107 (1976).

[23] G. H. C. New, IEEE Journal of Quantum Electronics **QE-10**, 115 (1974).

[24] H. A. Haus, IEEE Journal of Quantum Electronics **QE-11**, 736 (1975).

[25] I. S. Ruddock and D. J. Bradley, Applied Physics Letters **29**, 296 (1976).

[26] J.-C. Diels, E. V. Stryland, and G. Benedict, Optical Communications **25**, 93 (1978).

[27] R. L. Fork, B. I. Greene, and C. V. Shank, Applied Physics Letters **38**, 671 (1981).

[28] R. L. Fork, C. V. Shank, R. Yen, and C. A. Hirlimann, IEEE Journal of Quantum Electronics **QE-19**, 500 (1983).

[29] D. J. Bradley, A. J. F. Durrant, F. O'Neill, and B. Sutherland, Physics Letters **30A**, 535 (1969).

[30] J. M. Halbout and C. L. Tang, IEEE Journal of Quantum Electronics **QE-19**, 487 (1983).

[31] W. Dietel, J. J. Fontaine, and J.-C. Diels, Optics Letters **8**, 4 (1983).

[32] J.-C. Diels, W. Dietel, J. J. Fontaine, W. Ruldolph, and B. Wilhelmi, Journal of the Optical Society of America B **2**, 680 (1985).

[33] R. L. Fork, O. E. Martinez, and J. P. Gordan, Optics Letters **9**, 150 (1984).

[34] J. A. Valdmanis, R. L. Fork, and J. P. Gordon, Optics Letters **10**, 131 (1985).

[35] F. Gires and P. Tournois, Compt Rent **258**, 6112 (1964).

[36] E. B. Treacy, IEEE Journal of Quantum Electronics **QE-5**, 454 (1969).

[37] C. V. Shank, R. L. Fork, R. Yen, R. H. Stolen, and W. J. Tomlinson, Applied Physics Letters **40**, 761 (1982).

[38] R. L. Fork, C. Brito, C. H. P. C. Becker, and C. V. Shank, Optics Letters **12**, 483 (1987).

[39] J.-C. Diels, Femtosecond dye lasers, in *Dye Laser Principles with Applications*, edited by F. J. Duarte and L. W. Hillman, Academic Press, 1990.

[40] R. Szipocs, K. Ferencz, C. Speilmann, and F. Krausz, Optics Letters **19**, 201 (1994).

[41] J.-C. Diels *et al.*, Colliding pulse femtosecond lasers and apllications to the measurement of optical parameters, in *Ultrafast Phenomena IV: Springer Series in Chemical Physics*, edited by D. Auston and K. B. Eisenthal, p. 30, New York, 1984, Springer-Verlag, Berlin and Heidelburg.

[42] S. A. Akhmanov, V. A. Vysloukh, and A. S. Chirkin, *Optics of Femtosecond Laser Pulses* (American Institute of Physics, New York, 1992).

[43] J. A. Valdmanis and R. L. Fork, IEEE Journal of Quantum Electronics **22**, 112 (1986).

[44] C. V. Shank, R. L. Fork, and F. Beisser, Laser Focus , 59 (1983).

[45] W. Baumler and A. Penzkofer, Optical and Quantum Electronics **24**, 313 (1992).

[46] H. A. Haus, IEEE Journal of Quantum Elctronics **QE-12**, 169 (1976).

[47] G. Andrews, *Ph.D. Dissertation* (, 2003).

[48] H. A. Haus, Short pulse generation, in *Compact Sources of Ultrashort Pulses*, edited by I. N. D. III, Cambridge, England, 1995, Cambridge University Press.

[49] H. A. Haus, IEEE Journal on Selected Topics in Quantum Elctronics **6**, 1173 (2000).

[50] H. A. Haus, J. D. Moores, and L. E. Nelson, Optics Letters **18**, 51 (1993).

[51] F. Salin, P. Grangier, G. Roger, and A. Brun, Optics Letters **15**, 1374 (1990).

[52] F. W. Wise, I. A. Walmsley, and C. L. Tang, Optics Letters **13**, 129 (1988).

[53] H. A. Haus, Optics Communications **97**, 215 (1993).

[54] D. von de Linde, Applied Physics B **39**, 201 (1986).

[55] G. T. Harvey *et al.*, IEEE Journal of Quantum Electronics **27**, 295 (1991).

[56] H. A. Haus and A. Mecozzi, IEEE Journal of Quantum Electronics **29**, 983 (1993).

[57] I. G. Fuss, IEEE Journal of Quantum Electronics **30**, 2707 (1994).

[58] T. Shreiber, Physical Review Letters **85**, 461 (2000).

VITA

Wei Yang

Wei Yang was born on the 22nd of July, 1973, in Shenyang, China. His parents are Lianzhong Yang and Shuxian Liu. He graduated from Tianjin University, Tianjin, China with a Bachelor of Science in Applied Physics and a Bachelor of Engineering in Radio Technology in July 1995. He then attended the graduate program at Peking University, Beijing, China and received his Master of Science degree in Quantum Electronics in July 1998. In the autumn of 1998, he entered the graduate program in Physics at the College of William and Mary, Williamsburg, Virgina and received a Master of Science degree in Physics in May 2000. On the 7th of July, 2004, Mr. Yang defended his dissertation entitled *Characterization of the Transient Behaviors in a Colliding Pulse Mode-locked (CPM) Laser*, earning the degree of Doctor of Philosophy in experimental Physics.